

2002

Finite element and meshless methods in NDT applications

Liang Xuan

Iowa State University

Follow this and additional works at: <https://lib.dr.iastate.edu/rtd>

 Part of the [Electrical and Electronics Commons](#)

Recommended Citation

Xuan, Liang, "Finite element and meshless methods in NDT applications " (2002). *Retrospective Theses and Dissertations*. 554.
<https://lib.dr.iastate.edu/rtd/554>

This Dissertation is brought to you for free and open access by the Iowa State University Capstones, Theses and Dissertations at Iowa State University Digital Repository. It has been accepted for inclusion in Retrospective Theses and Dissertations by an authorized administrator of Iowa State University Digital Repository. For more information, please contact digirep@iastate.edu.

INFORMATION TO USERS

This manuscript has been reproduced from the microfilm master. UMI films the text directly from the original or copy submitted. Thus, some thesis and dissertation copies are in typewriter face, while others may be from any type of computer printer.

The quality of this reproduction is dependent upon the quality of the copy submitted. Broken or indistinct print, colored or poor quality illustrations and photographs, print bleedthrough, substandard margins, and improper alignment can adversely affect reproduction.

In the unlikely event that the author did not send UMI a complete manuscript and there are missing pages, these will be noted. Also, if unauthorized copyright material had to be removed, a note will indicate the deletion.

Oversize materials (e.g., maps, drawings, charts) are reproduced by sectioning the original, beginning at the upper left-hand corner and continuing from left to right in equal sections with small overlaps.

**ProQuest Information and Learning
300 North Zeeb Road, Ann Arbor, MI 48106-1346 USA
800-521-0600**

UMI[®]

NOTE TO USERS

This reproduction is the best copy available.

UMI

Finite element and meshless methods in NDT applications

by

Liang Xuan

A dissertation submitted to the graduate faculty
in partial fulfillment of the requirements for the degree of
DOCTOR OF PHILOSOPHY

Major: Electrical Engineering (Communications and Signal Processing)

Program of Study Committee:
Lalita Udpa, Co-major Professor
Shanker Balasubramaniam, Co-major Professor
Paul Sacks
Robert Weber
Yushi Sun
Satish Udpa

Iowa State University

Ames, Iowa

2002

Copyright © Liang Xuan, 2002. All rights reserved.

UMI Number: 3073489

Copyright 2002 by
Xuan, Liang

All rights reserved.

UMI[®]

UMI Microform 3073489

Copyright 2003 by ProQuest Information and Learning Company.
All rights reserved. This microform edition is protected against
unauthorized copying under Title 17, United States Code.

ProQuest Information and Learning Company
300 North Zeeb Road
P.O. Box 1346
Ann Arbor, MI 48106-1346

**Graduate College
Iowa State University**

This is to certify that the doctoral dissertation of

Liang Xuan

has met the dissertation requirements

Signature was redacted for privacy.

Co-major Professor

Signature was redacted for privacy.

Co-major Professor

Signature was redacted for privacy.

For the Major Program

TABLE OF CONTENTS

LIST OF FIGURES	vi
LIST OF TABLES	x
ACKNOWLEDGEMENTS	xi
ABSTRACT	xii
CHAPTER 1. INTRODUCTION.....	1
1.1 Eddy Current Testing.....	1
1.2 Problem Statement.....	3
1.3 Magneto-Optic Imaging.....	4
1.4 Physical Principle of Magneto-Optic Effect	5
1.5 Magneto-Optic Sensor	9
1.6 Process of Eddy Current Imaging.....	11
1.7 Need for Modeling for MOI.....	12
CHAPTER 2. FINITE ELEMENT MODELING	14
2.1 Galerkin Method.....	14
2.2 Electromagnetic Field Equations.....	15
2.3 Hexahedral Element.....	18
2.4 Finite Element Approach for EC NDT	20
2.5 Boundary Conditions	23
2.6 Solution of Linear Algebraic Equations	23

2.7	Post Processing	28
CHAPTER 3. FEM RESULTS AND DISCUSSIONS		30
3.1	Model Validation	30
3.2	Corrosion Dome in Single Layer	33
3.2.1	Geometry and Parameters	33
3.2.2	Effect of the Corrosion Depth	34
3.3	Corrosion Dome in Double Layers	37
3.3.1	Corrosion at the Bottom of the First Layer	37
3.3.2	Corrosion at the Top of the Second Layer	40
3.4	Optimal Excitation Frequency	42
3.5	Effect of Air Gap between Two Layers	43
3.6	Effect of the Slope of the Corrosion	44
3.7	Effect of Edge	47
CHAPTER 4. ELEMENT FREE GALERKIN METHOD		53
4.1	Introduction	53
4.2	Mathematical Preliminaries	54
4.2.1	Poisson Equation	55
4.2.2	Diffusion Equation	55
4.3	Element-Free Galerkin Method	56
4.3.1	Moving Least Square Approximation	57
4.3.2	Weight Function	59
4.3.3	Discontinuities Approximation	60
4.4	Numerical Implementation	62
4.4.1	Static Problem	62
4.4.2	Quasi-Static Problem	63
4.5	Applications and Results	64
4.5.1	Convergence Study and Comparison with Traditional FE	64

4.5.2	Application to Eddy Current NDT.....	67
-------	--------------------------------------	----

CHAPTER 5. MULTIFREQUENCY AND PULSED EDDY CURRENT TECHNIQUES74

5.1	Introduction	74
5.2	Multifrequency Eddy Currents.....	75
5.3	Pulsed Eddy Currents.....	78
5.3.1	Time Domain Solution.....	78
5.3.2	Analytic Solution in Frequency Domain.....	82
5.4	Conducting plate under Current Foil	88

CHAPTER 6. 3D ELEMENT FREE GALERKIN METHOD..... 92

6.1	Introduction	92
6.2	Numerical Implementation.....	92
6.2.1	Static Fields	93
6.2.2	Quasi-static Fields.....	95

CHAPTER 7. SUMMARY AND FUTURE WORK101

7.1	Summary of Work	101
7.2	Future Work	102

REFERENCES106

LIST OF FIGURES

Figure 1.1 Eddy current testing [4].	2
Figure 1.2 Corrosions in multiple layer structure.	3
Figure 1.3 Side view of crack under fastener.	4
Figure 1.4 Schematic of MOI instrument.	5
Figure 1.5 Numerical and real MO images.	11
Figure 1.1 (a) Hexahedral element in local coordinates. (b) Hexahedral element in global coordinates.	19
Figure 1.2 Region, boundary and interface in typical eddy current problem.	22
Figure 1.1 Geometry of hole with EDM notch.	31
Figure 1.2 (a) Mesh on y-z plane and induced current around the hole and notch. (b) MO image of flux leakage at the sensor substrate.	32
Figure 1.3 Geometry of single layer aluminum plate.	33
Figure 1.4 Mesh of the region of interest.	34
Figure 1.5 Source current in copper foil. (a).	35
Figure 1.6 (a) Induced current in y-z plane. (b) Induced current in z-x plane. (c) Induced current in x-y plane.	35
Figure 1.7 Numerical MO images of flux leakage at sensor layer for corrosion domes with different depth. (a) 10%, (b) 20%, (c) 30%, (d) 40%.	36
Figure 1.8 Geometry of double layers.	37
Figure 1.9 Numerical MO images of flux leakage at sensor layer for corrosion domes with different depth. (a) 10%, (b) 20%, (c) 30%, (d) 40%.	38
Figure 1.10 Peak values of flux leakage versus corrosion depth.	39
Figure 1.11 Geometry of double layers.	40
Figure 1.12 Surface plot of flux leakage and its MO image for 40% corrosion dome.	41
Figure 1.13 Peak values of flux leakage versus excitation frequency.	42
Figure 1.14 Geometry of corrosion dome with air gap between two layers.	43

Figure 1.15 Peak value of flux leakage versus the size of air gap.	44
Figure 1.16 Side view of the geometry and the MO image of flux leakage.....	45
Figure 1.17 Side view of the geometry and the MO image of flux leakage.....	45
Figure 1.18 Side view of the geometry and the MO image of flux leakage.....	46
Figure 1.19 Side view of the geometry and the MO image of flux leakage.....	46
Figure 1.20 Geometry of double layer aluminum plate with z-edge.	47
Figure 1.21 Geometry of z-edge and the MO image of flux leakage.	48
Figure 1.22 Geometry of z-edge and the MO image of flux leakage.	48
Figure 1.23 Geometry of y-edge and the MO image of flux leakage.	49
Figure 1.24 Geometry of y-edge and the MO image of flux leakage.	49
Figure 1.25 Peak value of flux leakage versus the distance between edge and corrosion center.....	50
Figure 1.26 Geometry of rivet head with radial crack (crack length 3 mm).....	51
Figure 1.27 Eddy currents around rivet head region. (a) Top view, (b) Side view.	51
Figure 1.28 MO image for rivet head with a radial crack.	52
Figure 1.1 Domain of influence of node adjacent to material discontinuity.	61
Figure 1.2 Surface plot of numerical solution.	65
Figure 1.3 (a) Error estimation in L^2 norm for the linear EFG. (b) Error estimation in H^1 norm for the linear EFG.....	66
Figure 1.4 (a) Error estimation in L^2 norm for the quadratic EFG. (b) Error estimation in H^1 norm for the quadratic EFG.	66
Figure 1.5 (a) Error estimation in L^2 norm for different weight functions. (b) Error estimation in H^1 norm for different weight functions.....	67
Figure 1.6 Eddy current in unit disk.....	69
Figure 1.7 (a) Error estimation in L^2 norm. (b) Error estimation in H^1 norm.....	70
Figure 1.8 Discretization of solution region with a tight crack. (a) EFG (b) FEM	71
Figure 1.9 (a) Eddy current in presence of crack predicted by EFG. (b) Difference between EFG and FEM.	71

Figure 1.10 (a) Geometry of an 'H' plate. (b) Numerical induced currents inside the plate calculated by EFG. (c) Numerical induced currents inside the plate calculated by FEM. (d) Difference between FEM and EFG.....	73
Figure 1.1 Eddy currents in a disk with the excitation frequency of (a) 300 Hz (b) 1 KHz (c) 3 KHz (d) 10 KHz . The length of arrow is proportional to amplitude of current density.	77
Figure 1.2 Relative error versus excitation frequency. (a) in L^2 norm (b) in H^1 norm	77
Figure 1.3 Geometry of current source and conducting half-space.	80
Figure 1.4 Magnetic potential at various time instances. (a) $t = 5 \mu s$ (b) $t = 30 \mu s$ (c) $t = 55 \mu s$ (d) $t = 80 \mu s$	80
Figure 1.5 Induced current at various time instances. (a) $t = 12 \mu s$ (b) $t = 18 \mu s$ (c) $t = 24 \mu s$ (d) $t = 30 \mu s$	81
Figure 1.6 Induced current in the conducting plate with a sinusoidal excitation and parameters $\tau = 0.72 \text{ mm}$, $\Delta = 0.5 \text{ mm}$ and $h = 2 \text{ mm}$ at (a) $\omega = 400 \text{ Hz}$, (b) $\omega = 1 \text{ KHz}$, (c) $\omega = 4 \text{ KHz}$, (d) $\omega = 10 \text{ KHz}$. The contour lines are drawn at value of 0.1 , 0.3 , 0.5 , 0.7 , 0.9 times peak value.	86
Figure 1.7 Induced current distribution along y axis at various time instances. (a) $\Delta = 0.5 \text{ mm}$ (b) $\Delta = 0.1 \text{ mm}$. Dashed lines denote the analytical solution, solid line denote the numerical solution.	87
Figure 1.8 Conducting plate under current sheet.	88
Figure 1.9 Magnetic vector potential with frequency of 3 KHz (a) real part (b) imaginary part	91
Figure 1.10 Magnetic vector potential with frequency of 10 KHz (a) real part (b) imaginary part.....	91
Figure 1.1 (a) Error estimation in L^2 norm for the linear EFG. (b) Error estimation in H^1 norm for the linear EFG.....	94
Figure 1.2 Computation time for 3D Poisson Problems. (a) CPU time versus number of nodes. (b) The product of CPU time and numerical error versus number of nodes.....	94
Figure 1.3 Geometry of conducting plate under current foil.	96

Figure 1.4 Magnetic vector potential at frequency of 3 <i>KHz</i> . (a) real part, (b) imaginary part.	97
Figure 1.5 Magnetic vector potential at frequency of 10 <i>KHz</i> . (a) real part, (b) imaginary part.	97
Figure 1.6 Induced currents in the conducting plate. (a) Top view of the real part of currents (plane $z = 0$) (b) Top view of the imaginary part of currents (plane $z = 0$) (c) Side view of the real part of currents (plane $y = 0$) (d) Side view of the imaginary part of currents (plane $y = 0$).....	99
Figure 1.7 Induced currents in the conducting plate. (a) Top view of the real part of currents (plane $z = 0$) (b) Top view of the imaginary part of currents (plane $z = 0$) (c) Side view of the real part of currents (plane $y = 0$) (d) Side view of the imaginary part of currents (plane $y = 0$).....	100

LIST OF TABLES

Table 1.1 Parameters used in model validation.	31
Table 1.2 Boundary conditions.	32
Table 1.3 Parameters used in single layer plate test.....	34
Table 1.4 Parameters in test.....	51
Table 1.1 Boundary conditions.	96

ACKNOWLEDGEMENTS

I would like to express gratitude to my major professors and research advisors, Dr. Lalita Udpa and Dr. Shanker Balasubramaniam for their instruction, guidance and encouragement during this Ph.D study. I would also like to thank Dr. Satish Udpa, Dr. Yushi Sun, Dr. Robert Weber and Dr. Paul Sacks for their valuable comments and suggestions.

Special thanks are extended to my research fellows in Material Assessment Research Group at Iowa State University (now in Michigan State University), including Chao Chen, Yue Li, Zhiwei Zeng, Paradeep Ramuhalli for their supports and helpful discussions during my stay in this group.

Also I want to mention this research is based on the work supported by the Federal Aviation Administration under Contract No. DTFA03-98-D-00008, and performed at Iowa State University's Center for Aviation Systems Reliability program through the Airworthiness Assurance Center of Excellence.

At last, but not least, I want to thank my parents and homeland for their culture, encouragement and help through all these years.

ABSTRACT

Eddy current nondestructive testing (NDT) methods are extensively used in the inspection of aging aircrafts. Thousands of fasteners and bonded joints on each aircraft should be inspected and in order to handle the huge task, fast, accurate and cost effective inspection methods are clearly needed. Some of the challenges encountered in eddy current testing are (1) detection of corrossions or cracks in the multi-layer structures, (2) detection of cracks under the fastener (CUF), (3) detection of surface and subsurface defects close to edges.

Conventional eddy current inspection method is time consuming due to the small probe size and large inspection area. Furthermore it requires trained operators for data interpretation. Development of new techniques for rapid and accurate inspection is of considerable interest to the aviation industry. In this dissertation, a more recent eddy current technique called magneto-optic imaging (MOI) is studied.

The availability of a theoretical model that can simulate the MOI system performance is extremely important for understanding and optimizing the MOI sensor and hardware system. In this dissertation, finite element (FE) methods have been applied to numerically compute the electromagnetic fields associated with MOI testing with respect to variation in parameters such as operating frequency, source current and sensor parameters. Most of the testing geometries are three-dimensional and consequently the FE models require extensive computational resources. This paper presents a robust FE model based on A-V formulation

and a fast iterative solver, which offers a distinct advantage in terms of computational time and data storage.

A major contribution of this work is the development of Element-Free Galerkin (EFG) method for NDE applications. In order to model the complex CUF geometry, EFG method has been studied. Two and three-dimensional models for Poisson equation and diffusion equation, describing static or low frequency problems, have been developed and compared with conventional FE methods. EFG methods have also been applied to multi-frequency and pulsed eddy current problems. Simulation results clearly demonstrate the feasibility of the method for time-dependent field applications.

CHAPTER 1. INTRODUCTION

Nondestructive testing (NDT) methods are widely used in industry to control product qualities. It may be defined as the inspection of an object or material with technology that does not affect its future usefulness. NDT can be used without any physical damage to the test specimen [1]. Consequently, NDT provides an excellent balance between quality control and cost-effectiveness. NDT is applied not only to locate a defect, but also to provide information about the defect such as size, shape, and orientation. Furthermore, it may also be used to characterize material properties. Common NDT techniques include ultrasonic testing, magnetic flux leakage testing, and eddy current testing etc.

1.1 Eddy Current Testing

Eddy current methods of NDT are one of the most commonly used methods for evaluating the integrity of materials in industry [2]. A traditional eddy current test set up involves a probe consisting of a coil or a set of coils excited by a time varying current waveform (Figure 1.1). When this probe is placed close to a conducting material, it induces eddy current inside the specimen (Faraday's law). The magnetic field generated by the eddy current (Ampere's law) opposes the field produced by the probe coil (Lenz's law). The net effect is a change in the magnetic flux linking the coil which by definition is the coil impedance [3] [4].

Defects in the test sample disturb the eddy current distribution which in turn alters the net magnetic flux linking the coil. Consequently the presence of a defect is detected as a change

of the coil impedance. The changes of coil impedance could be measured as the probe scans the specimen.

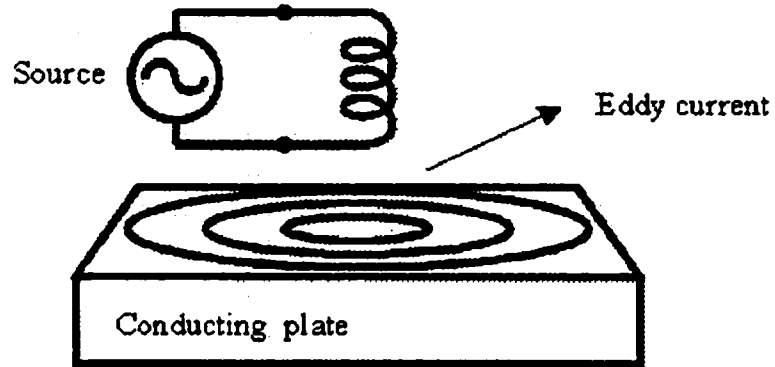


Figure 1.1 Eddy current testing [4].

Eddy current techniques are widely used in the inspection of aircraft structure composed largely of conducting material. It is more suitable to detect surface flaws or subsurface flaws close to the surface because of the skin depth effect. It can be shown that the current density decays with the depth inside the conducting material. The amplitude of fields at a depth x could be expressed as

$$A_x = A_0 e^{-\frac{x}{\delta}} \quad (1.1)$$

where A_0 is the amplitude of field on the surface of a half-infinite conducting plate. And δ is the skin depth given by [5] [6]

$$\delta = \sqrt{\frac{1}{\pi f \sigma \mu}} \quad (1.2)$$

σ : the conductivity of the plate.

μ : the permeability of the plate.

f : the frequency of the excitation.

1.2 Problem Statement

With the continuous growth of air transportation, more and more aircrafts have to be maintained to extend their service lifetime. For flight safety, it is critical to have periodic inspections of aging aircrafts. Thousands of fasteners and bonded joints on each aircraft should be inspected and in order to handle the huge task, fast, accurate and cost effective inspection methods are clearly needed.

Some of the challenges encountered in eddy current testing are (1) detection of corrosions or cracks in the multiple layers as shown in Figure 1.2, (2) detection of cracks under the fastener (CUF) as shown in Figure 1.3, (3) detection of defects close to edges [3] [4].

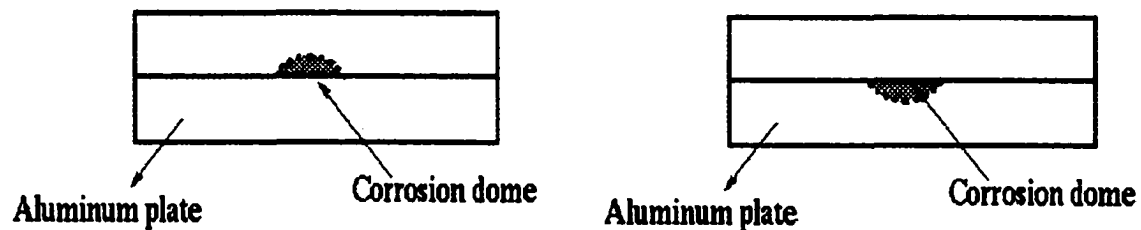


Figure 1.2 Corrosions in multiple layer structure.

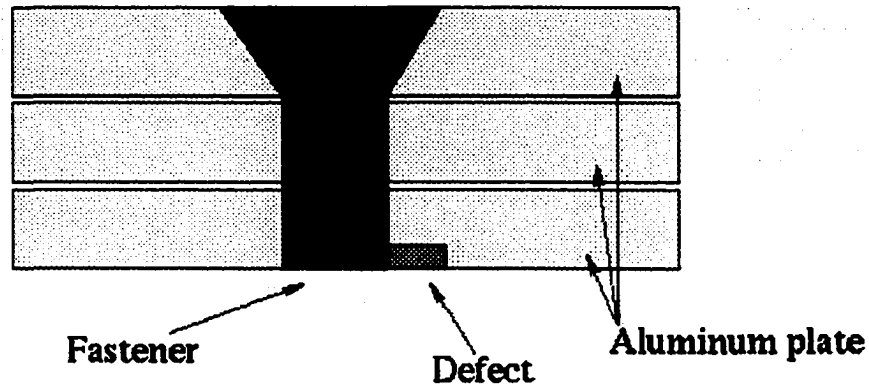


Figure 1.3 Side view of crack under fastener.

Conventional eddy current inspection methods is time consuming due to the small probe size and large inspection area; also it requires trained operators for data interpretation. Development of new technique for rapid and accurate inspection is of considerable interest to the aviation industry. In this dissertation, a more recent eddy current technique called magneto-optic imaging is studied.

1.3 Magneto-Optic Imaging

Magneto-optic imaging (MOI) is a relatively new sensor application of bubble memory technology to nondestructive inspection. The MOI uses a magneto-optic (MO) sensor to produce easy to interpret analog images of magnetic flux leakage from surface and subsurface crack or corrosion in aging aircraft skin structure. The principles of the magneto-optic imaging is based on Faraday induction and Faraday rotation effect. Eddy current in the test specimen is produced by electromagnetic induction; Faraday rotation effect is applied to produce magneto-optic images of magnetic flux associated with the eddy currents [7] [8].

A schematic of MOI instrument is shown in Figure 1.4 [9]-[11]. A copper foil carries time-varying currents at low frequency (1.5 – 200 KHz), which induces eddy currents in the test specimen. When there are no defects, the associated magnetic flux is tangential to the specimen surface. Anomalies in the specimen result in the generation of a normal component of the magnetic flux density. This magnetic flux leakage is then imaged using Faraday rotation effect. A linear polarized light is incident normally on the MO sensor placed above the copper foil. The flux leakage will rotate the plane of polarization of the incident light. When the light reflected from the MO sensor, it is viewed by analyzer, the local occurrence of normal magnetic flux is seen as ‘dark’ areas depending on the direction of the fields. The principles on MOI technique are introduced in following sections.

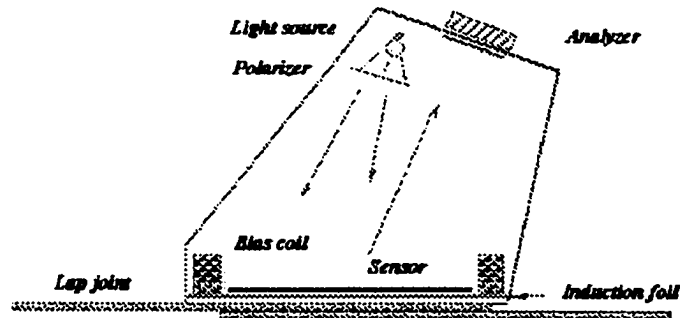


Figure 1.4 Schematic of MOI instrument.

1.4 Physical Principle of Magneto-Optic Effect

The Magneto-optic effect describes the interactions between magnetized material and light [12]. At a macroscopic level, these interactions could be characterized by the constitutive relations,

$$\bar{D} = \epsilon \bar{E} \quad (1.3a)$$

$$\bar{B} = \mu \bar{H} \quad (1.3b)$$

Where \bar{D} is electric flux density, \bar{E} is electric field intensity, \bar{B} is magnetic flux density and \bar{H} is magnetic field intensity. ϵ is permittivity tensor of the medium, and μ is permeability tensor of the medium. Equation (1.3) describes how the materials respond to the electromagnetic fields.

When a magnetic field \bar{H} is applied to a magnetic medium, a change in the magnetization \bar{M} will occur, and can be described by

$$\bar{M} = \chi \bar{H} \quad (1.4)$$

where χ is the magnetic susceptibility tensor of the medium.

The change in magnetization in turn induces a perturbation in the permittivity tensor ϵ . This phenomenon is called the magneto-optic effect [13].

$$\epsilon = \epsilon_{jk}(\bar{M}) = \epsilon_0 (\epsilon_r \delta_{jk} + i f_1 e_{jkl} M_l + f_{jklm} M_l M_m) \quad (1.5)$$

where $i = \sqrt{-1}$, j and k takes values 1, 2 or 3. M_1, M_2 and M_3 stands for magnetization components along the principle axes X, Y , and Z respectively. ϵ_r is the relative permittivity in the paramagnetic state ($\bar{M} = 0$). f_1 and f_{jklm} are the first and second order magneto-optic factors respectively, and e_{jkl} is the antisymmetric alternate index of the third order.

Considering the first order magneto-optic factor, the permittivity tensor is given by

$$\boldsymbol{\varepsilon} = \varepsilon_0 \begin{bmatrix} \varepsilon_r & if_1 M_3 & -if_1 M_2 \\ -if_1 M_3 & \varepsilon_r & if_1 M_1 \\ if_1 M_2 & -if_1 M_1 & \varepsilon_r \end{bmatrix} \quad (1.6)$$

In an isotropic transparent media, if incident light and the magnetization is taken as z direction, the permittivity tensor becomes

$$\boldsymbol{\varepsilon} = \varepsilon_0 \begin{bmatrix} \varepsilon_r & if_1 M_3 & 0 \\ -if_1 M_3 & \varepsilon_r & 0 \\ 0 & 0 & \varepsilon_r \end{bmatrix} \quad (1.7)$$

The interaction between material and light could be easily explained by a plane wave solution of Maxwell equations.

Consider an electromagnetic wave propagates in $+\hat{z}$ direction in the media (assume charge density $\rho = 0$). The governing equations are given by

$$\nabla \times \bar{\mathbf{E}} = -\frac{\partial \bar{\mathbf{B}}}{\partial t} \quad (1.8a)$$

$$\nabla \times \bar{\mathbf{H}} = \frac{\partial \bar{\mathbf{D}}}{\partial t} + \bar{\mathbf{J}} \quad (1.8b)$$

$$\nabla \cdot \bar{\mathbf{D}} = 0 \quad (1.8c)$$

$$\nabla \cdot \bar{\mathbf{B}} = 0 \quad (1.8d)$$

The fields of this plane wave could be written as

$$\bar{\mathbf{E}} = (\hat{x}E_x + \hat{y}E_y)e^{i(\omega t - kz)} \quad (1.9a)$$

$$\bar{\mathbf{H}} = (\hat{x}H_x + \hat{y}H_y)e^{i(\omega t - kz)} \quad (1.9b)$$

where ω is the angular frequency and $k = \frac{2\pi}{\lambda}$ is the wave vector. Substitute (1.9) into (1.8),

we could obtain

$$\begin{pmatrix} E_x \\ E_y \end{pmatrix} = \begin{pmatrix} 0 & \nu \\ -\nu & 0 \end{pmatrix} \begin{pmatrix} B_x \\ B_y \end{pmatrix} \quad (1.10a)$$

and

$$\begin{pmatrix} H_x \\ H_y \end{pmatrix} = \begin{pmatrix} 0 & -\nu \\ \nu & 0 \end{pmatrix} \begin{pmatrix} D_x \\ D_y \end{pmatrix} \quad (1.10b)$$

where $\nu = \frac{\omega}{k}$.

Applying (1.10) into (1.3), we get

$$\begin{pmatrix} D_x \\ D_y \end{pmatrix} = \epsilon_0 \begin{pmatrix} \epsilon_r & if_1 M_3 \\ -if_1 M_3 & \epsilon_r \end{pmatrix} \begin{pmatrix} E_x \\ E_y \end{pmatrix} = \frac{1}{\nu^2 \mu} \begin{pmatrix} E_x \\ E_y \end{pmatrix} \quad (1.11)$$

Equation (1.11) is an eigenvalue problem. $\frac{1}{\nu^2 \mu}$ only can be chosen to be either one of the

two eigenvalues of matrix $\epsilon_0 \begin{pmatrix} \epsilon_r & if_1 M_3 \\ -if_1 M_3 & \epsilon_r \end{pmatrix}$. And ν is given by

$$\nu = \sqrt{\frac{1}{\epsilon_0 \mu (\epsilon_r \pm f_1 M_3)}} \quad (1.12a)$$

$$E_x = \pm i E_y, \quad H_x = \pm i H_y \quad (1.12b)$$

Here we get two possible waves (eigenmode) in space. The wave vectors for the left and right circularly polarized waves are

$$k_L = \omega \sqrt{\epsilon_0 \mu (\epsilon_r + f_1 M_3)} \quad (1.13a)$$

$$k_R = \omega \sqrt{\epsilon_0 \mu (\epsilon_r - f_1 M_3)} \quad (1.13b)$$

Assume at position $z = 0$,

$$\vec{H} = \hat{x}H_0 = (\hat{x} + i\hat{y})\frac{H_0}{2} + (\hat{x} - i\hat{y})\frac{H_0}{2} \quad (1.14)$$

where the linear polarized wave is resolved into two eigenmode circular polarized components with $H_0 = |H_x| = |H_y|$.

At position $z = d$, the magnetic field will be

$$H = (\hat{x} + j\hat{y})\frac{H_0}{2}e^{-jk_L d} + (\hat{x} - j\hat{y})\frac{H_0}{2}e^{-jk_R d} \quad (1.15)$$

It could also be expressed as

$$H = \frac{H_0}{2}(e^{-jk_L d} + e^{-jk_R d})(\hat{x} + \hat{y}j \tan \theta) \quad (1.16)$$

where

$$\theta = \frac{(k_L - k_R)d}{2} = \omega \sqrt{\frac{\epsilon_0 \mu}{\epsilon_r}} f_1 M_3 d \quad (1.17)$$

The above results show that the wave is still linearly polarized but is rotated by an angle θ .

This phenomenon is called Faraday rotation.

The angle of rotation θ is proportional to the magnetization M_3 , and the relationship is given by

$$\theta = KM_3 d \quad (1.18)$$

where K is called Kundt's constant.

1.5 Magneto-Optic Sensor

The magneto-optic sensor used in the MOI consists of a bismuth-doped iron garnet film of thickness 0.5 mm and diameter 75 mm . These films exhibit three important physical

properties for MO imaging [8] [11]. First the films is uniaxial magnetic-anisotropic, that is, they have a ‘easy’ axis of magnetization normal to the sensor surface and a ‘hard’ axis of magnetization along the sensor plate. Second, the films have a ‘memory’. They can still retain most of the magnetization even the magnetic fields are removed along the easy axis of magnetization. Third, the films possess a large Faraday rotation θ_f , usually ranges from 20,000 to 40,000 *degree/cm*. This property is particularly useful in detecting low level magnetic fields, which is desirable in NDT applications.

When a linearly polarized light normally passes through a garnet film, the plane of polarization of the light will be rotated by angle θ . The angle is given by [14],

$$\theta = \theta_f (\vec{k} \cdot \vec{M}) d / (|\vec{k}| |\vec{M}_s|) \quad (1.19)$$

where \vec{k} is the wave vector of the light, \vec{M} is the local magnetization and d is the thickness of the film, while \vec{M}_s is the saturated magnetization. For a reflection type MOI instrument, the incident light will be reflected back through the sensor film again, the effective Faraday rotation will be doubled.

Through an analyzer as shown in Figure 1.4, the local occurrence of magnetization in the sensor can be seen as a high contrast dark-light area.

In practice, the MO images are not perfect dark and light images. In an experimental image, we can see many randomly distributed curves as shown in Figure 1.5. Those curves actually show the structure of the serpentine domains in the sensor film [15] [16]. A common bubble memory film contains two kinds of domain structures, in which magnetic moments are directed either along or opposite to the easy axis, that is, the normal direction of the

sensor. The binary modes of the magnetic moments result in producing binary valued MO images.

When a magnetic field is applied normal to the sensor, the domain will expand when the direction of its magnetic moment is same as that of the applied field, and contract with the field in opposite orientation. So the intensity of the magnetic field will affect the size of the domains and not the intensity of the images.

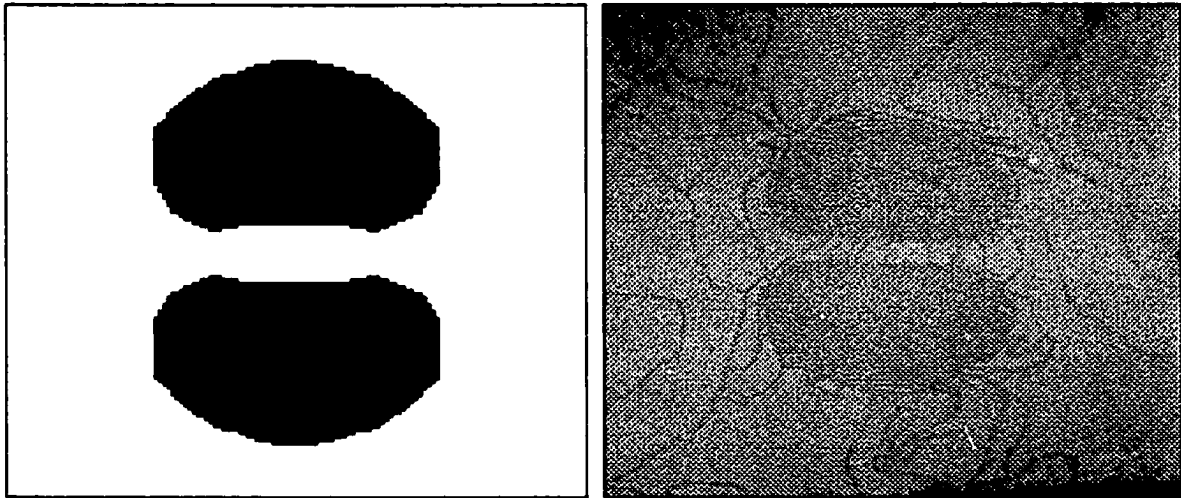


Figure 1.5 Numerical and real MO images.

1.6 Process of Eddy Current Imaging

If the specimen has no defect, when a linear time-varying excitation is applied in the copper foil, it produces a time-varying magnetic field parallel to the sensor plate which is along the hard axis of magnetization of sensor. Thus it has little or no effect on the state of magnetization of the sensor. If there is some defect in the specimen, the induced currents inside the specimen will be turned and produce magnetic field normal to the sensor plate which is parallel to the easy axis of magnetization of the sensor. As mentioned in section 1.5,

this magnetic field can be imaged as a dark area in the sensor. It should be mentioned that a bias magnetic field (around 3 G) is needed to get a larger field passing through the sensor so that the state of magnetization of the sensor is flipped by the small field produced by perturbation in the induced eddy currents.

The actual steps for producing image is as follows. First, an erase pulse in the bias coil (shown in Figure 1.4) is applied so that the background image in the sensor is bright. Then a bias field is applied and excitation in the foil is turned on at the same time, so that an image is formed in the sensor. Finally the excitation is turned off. However the sensor has a memory, and the image remains until the start of the next erase pulse.

1.7 Need for Modeling for MOI

The availability of a theoretical model that can simulate the MOI system performance is extremely important for optimization of the MOI sensor and hardware system. First, the model is useful in visualization of the electromagnetic fields around the testing specimen. Secondly, by providing quantitative values of electromagnetic fields, a numerical model can be used to adjust the MOI instrument parameters such as operating frequency, source current and sensor parameters. Thirdly, simulation model can help in understanding and visualizing the field/flaw interaction which is important in determining the improvement needed in sensor development.

This dissertation includes the following part: Chapter 2 presents the basic theory of the finite element method applied to NDT problems. Chapter 3 presents a series of simulation results and discussions on MOI applications. Chapter 4 introduces the meshless EFG method

and its applications in NDT. Chapter 5 presents EFG modeling on the multifrequency and pulsed eddy current technique, then three-dimensional EFG method on static and quasi-static electromagnetic fields is studied in Chapter 6. Finally Chapter 7 gives the summary and future work.

CHAPTER 2. FINITE ELEMENT MODELING

In general mathematic models of physical phenomena involve differential equations for which analytic solutions are not always available. Consequently, there has been considerable activity in the development of numerical approximations. The finite element method (FEM) is such a technique. In the past 40 years, finite element method has been widely applied to solve problems in structural mechanics, fluid dynamics, heat transfer and electromagnetics [17]-[19]. In the following sections, we will describe the finite element method based on Galerkin procedure, and set up the finite element model for electromagnetic eddy current problems.

2.1 Galerkin Method

Consider a linear operational equation.

$$Lu = f \quad \text{in } \Omega \quad (2.1a)$$

with homogeneous boundary conditions

$$\frac{\partial u}{\partial n} = 0 \quad \text{on } S_1 \quad (2.1b)$$

$$u = 0 \quad \text{on } S_2 \quad (2.1c)$$

where

$S = S_1 \cup S_2$ is boundary of Ω .

L is a second order differential operator [20].

The weak form of (2.1) is to find $u \in V$, a vector space, such that

$$(Lu, v) = (f, v) \quad (2.2)$$

holds for any $v \in V$.

In FEM, the vector space V is chosen as a finite space, which is a linear expansion of a set of linear independent functions φ_i called shape functions, and u could be written as

$u = \sum_{i=1}^n \varphi_i u_i$. Substituting this into (2.2), will get

$$(Lu, v_i) = (f, v_i) \quad \text{for } i = 1, 2, \dots, m \quad (2.3)$$

Usually φ_i is chosen to be

$$\varphi_i = \begin{cases} \neq 0 & \text{in } \Omega_i \\ = 0 & \text{in } \Omega \setminus \Omega_i \end{cases} \quad (2.4)$$

where Ω_i is a finite element. A numerical implementation of the Galerkin method will be obtained if we choose $v_i = \varphi_i$ and $m = n$. Then (2.3) become a linear algebraic equation.

$$[G][u] = [F] \quad (2.5)$$

with $G_{ij} = (L\varphi_i, \varphi_j)$ and $F_i = (f, \varphi_j)$.

$[G]$ is called stiffness matrix, $[F]$ is load vector.

2.2 Electromagnetic Field Equations

The governing equations for electromagnetic fields are given by Maxwell equations, which can be written in differential form as

$$\nabla \times \vec{E} = -\frac{\partial \vec{B}}{\partial t} \quad (\text{Faraday's law}) \quad (2.6a)$$

$$\nabla \times \vec{H} = \vec{J} + \frac{\partial \vec{D}}{\partial t} \quad (\text{Ampere's law}) \quad (2.6b)$$

$$\nabla \cdot \vec{D} = \rho \quad (\text{Gauss's law}) \quad (2.6c)$$

$$\nabla \cdot \vec{B} = 0 \quad (\text{Gauss's law}) \quad (2.6d)$$

where:

\vec{J} electric current density (Am^{-2})

ρ electric charge density (Cm^{-3})

In addition, the above equations are supplemented by the constitutive relations describing macroscopic properties of the media

$$\vec{D} = \epsilon \vec{E} \quad (2.7a)$$

$$\vec{B} = \mu \vec{H} \quad (2.7b)$$

$$\vec{J} = \sigma \vec{E} \quad (2.7c)$$

where μ, ϵ, σ denote the permeability, permittivity and conductivity respectively. For linear isotropic media, μ, ϵ, σ are scalars, and doesn't depend on fields.

In the following model development, we make some assumptions:

- The media is linear and isotropic in each element, so they are single valued constants in each element.
- The field is magneto-static or quasi magneto-static, so the displacement current is negligible.
- There is no free charge in solution region, so $\rho = 0$.

With these assumptions, we can define magnetic vector potential \vec{A} in terms of flux density \vec{B} as

$$\vec{B} = \nabla \times \vec{A} \quad (2.8)$$

and substitute it in (2.6a) to get $\nabla \times \vec{E} = -\nabla \times \frac{\partial \vec{A}}{\partial t}$. Thus \vec{E} could be expressed as

$$\vec{E} = -\frac{\partial \vec{A}}{\partial t} - \nabla \Phi \quad (2.9)$$

where Φ is called electric scalar potential.

Through Ohm's law $\vec{J} = \sigma \vec{E} + \vec{J}_s$ and (2.9), (2.6b) changes to

$$\nabla \times \left(\frac{1}{\mu} \nabla \times \vec{A} \right) + \sigma \left(\frac{\partial \vec{A}}{\partial t} + \nabla \Phi \right) = \vec{J}_s \quad (2.10)$$

In eddy current problem, when the excitation current is a single frequency time-varying harmonic source, all field quantities vary sinusoidally, and then (2.10) could be written as [17]

$$\nabla \times \left(\frac{1}{\mu} \nabla \times \vec{A} \right) + \sigma (j\omega \vec{A} + \nabla \Phi) = \vec{J}_s \quad (2.11)$$

In order to obtain a unique solution of (2.11), a gauge condition is necessary. Two well-known gauge conditions, Lorentz gauge and Coulomb gauge are generally used.

The Lorentz gauge condition is expressed as

$$\nabla \cdot \vec{A} + \frac{1}{c^2} \frac{\partial \Phi}{\partial t^2} = 0 \quad (2.12)$$

where c is the speed of speed of light in free space. Lorentz gauge is suitable for high frequency problems, since it leads to a set of wave equations and thus the potentials will be in wave form.

For Coulomb gauge,

$$\nabla \cdot \vec{A} = 0 \quad (2.13)$$

From (2.6c), we see that the scalar potential satisfies the Poisson equation,

$$\nabla^2 \Phi = -\frac{\rho}{\epsilon_0} \quad (2.14)$$

with solution

$$\Phi(x) = \frac{1}{4\pi\epsilon_0} \int \frac{\rho(x')}{|x-x'|} dx' \quad (2.15a)$$

and this potential is just the Coulomb potential due to the charge density ρ . Coulomb potential is generally used in low frequency problems since the displacement current is negligible and the resulting equations are simplified. Since there is no free charge and the scalar potential is only defined in a finite region,

$$\Phi(x) = \frac{1}{4\pi} \oint_S \left[\frac{1}{|x-x'|} \frac{\partial \Phi(x')}{\partial n'} - \Phi(x') \frac{\partial}{\partial n'} \left(\frac{1}{|x-x'|} \right) \right] dx' \quad (2.15b)$$

where S is the boundary of conducting region.

2.3 Hexahedral Element

In general, it is convenient to use local normalized coordinates (ξ, η, ζ) to derive the stiffness matrix and load vector. For a linear hexahedral element, the solution u^e inside any element could be expressed as

$$u^e(\xi, \eta, \zeta) = [N]^T [u]^e = \sum_{i=1}^8 N_i u_i^e \quad (2.16)$$

The shape functions are defined by

$$N_i(\xi, \eta, \zeta) = (1 + \xi_i \xi)(1 + \eta_i \eta)(1 + \zeta_i \zeta) \quad \text{for } i = 1, 2, \dots, 8 \quad (2.17)$$

where (ξ_i, η_i, ζ_i) is the local coordinate of a vertex in the element shown in Figure 2.1a.

Global coordinates (x, y, z) could be explicitly defined by local coordinates (ξ, η, ζ) , by the relationships.

$$x(\xi, \eta, \zeta) = [N]^T [x]^e = \sum_{i=1}^8 N_i x_i \quad (2.18a)$$

$$y(\xi, \eta, \zeta) = [N]^T [y]^e = \sum_{i=1}^8 N_i y_i \quad (2.18b)$$

$$z(\xi, \eta, \zeta) = [N]^T [z]^e = \sum_{i=1}^8 N_i z_i \quad (2.18c)$$

where (x_i, y_i, z_i) are corresponding global coordinates shown in Figure 2.1b.

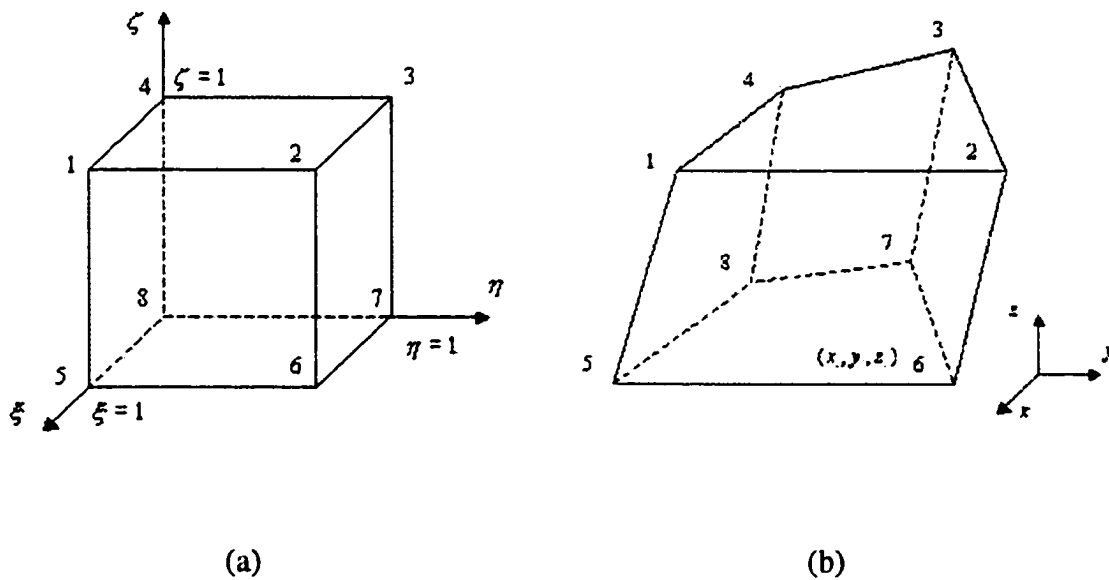


Figure 2.1 (a) Hexahedral element in local coordinates. (b) Hexahedral element in global coordinates.

The Jacobian for the coordinate transformation is

$$[J] = \begin{bmatrix} \frac{\partial x}{\partial \xi} & \frac{\partial y}{\partial \xi} & \frac{\partial z}{\partial \xi} \\ \frac{\partial x}{\partial \eta} & \frac{\partial y}{\partial \eta} & \frac{\partial z}{\partial \eta} \\ \frac{\partial x}{\partial \zeta} & \frac{\partial y}{\partial \zeta} & \frac{\partial z}{\partial \zeta} \end{bmatrix} = \begin{bmatrix} \sum_{i=1}^8 \frac{\partial N_i}{\partial \xi} x_i & \sum_{i=1}^8 \frac{\partial N_i}{\partial \xi} y_i & \sum_{i=1}^8 \frac{\partial N_i}{\partial \xi} z_i \\ \sum_{i=1}^8 \frac{\partial N_i}{\partial \eta} x_i & \sum_{i=1}^8 \frac{\partial N_i}{\partial \eta} y_i & \sum_{i=1}^8 \frac{\partial N_i}{\partial \eta} z_i \\ \sum_{i=1}^8 \frac{\partial N_i}{\partial \zeta} x_i & \sum_{i=1}^8 \frac{\partial N_i}{\partial \zeta} y_i & \sum_{i=1}^8 \frac{\partial N_i}{\partial \zeta} z_i \end{bmatrix} \quad (2.19)$$

and the relationships between local, global derivatives of shape functions is

$$\begin{bmatrix} \frac{\partial N_i}{\partial \xi} \\ \frac{\partial N_i}{\partial \eta} \\ \frac{\partial N_i}{\partial \zeta} \end{bmatrix} = \begin{bmatrix} \frac{\partial x}{\partial \xi} & \frac{\partial y}{\partial \xi} & \frac{\partial z}{\partial \xi} \\ \frac{\partial x}{\partial \eta} & \frac{\partial y}{\partial \eta} & \frac{\partial z}{\partial \eta} \\ \frac{\partial x}{\partial \zeta} & \frac{\partial y}{\partial \zeta} & \frac{\partial z}{\partial \zeta} \end{bmatrix} \begin{bmatrix} \frac{\partial N_i}{\partial x} \\ \frac{\partial N_i}{\partial y} \\ \frac{\partial N_i}{\partial z} \end{bmatrix} = [J] \begin{bmatrix} \frac{\partial N_i}{\partial x} \\ \frac{\partial N_i}{\partial y} \\ \frac{\partial N_i}{\partial z} \end{bmatrix} \quad (2.20)$$

So

$$\begin{bmatrix} \frac{\partial N_i}{\partial x} \\ \frac{\partial N_i}{\partial y} \\ \frac{\partial N_i}{\partial z} \end{bmatrix} = [J]^{-1} \begin{bmatrix} \frac{\partial N_i}{\partial \xi} \\ \frac{\partial N_i}{\partial \eta} \\ \frac{\partial N_i}{\partial \zeta} \end{bmatrix} \quad (2.21)$$

2.4 Finite Element Approach for EC NDT

Including the implicit gauge condition $\nabla \cdot \bar{A} = 0$, Maxwell equations for time-varying harmonic fields written in potential form are [22]-[25]

$$\nabla \times \left(\frac{1}{\mu} \nabla \times \bar{A} \right) + \nabla \left(\frac{1}{\mu} \nabla \cdot \bar{A} \right) + j\omega \sigma \bar{A} + \sigma \nabla V = \bar{J}_s \quad \text{in } \Omega \quad (2.22a)$$

$$\nabla \cdot (j\omega \sigma \bar{A} + \sigma \nabla V) = 0 \quad \text{in } \Omega_1 \quad (2.22b)$$

Ω_1 denotes the conducting region, Ω_2 denotes the free space region, and $\Omega = \Omega_1 \cup \Omega_2$ as shown in Figure 2.2.

The potentials are expressed in terms of corresponding functions inside the element Ω_e as

$$\bar{A} = \sum_{j=1}^8 N_j A_{xj} \hat{x} + N_j A_{yj} \hat{y} + N_j A_{zj} \hat{z} = \sum_{k=1}^{24} \bar{N}_k A_k^e \quad (2.23a)$$

$$V = \sum_{j=1}^8 N_j V_j^e \quad (2.23b)$$

where

$$\bar{N}_k = \begin{cases} N_j \hat{x} & k = 3j - 2 \\ N_j \hat{y} & k = 3j - 1 \\ N_j \hat{z} & k = 3j \end{cases} \quad (2.24a)$$

and

$$A_k^e = \begin{cases} A_{xj}^e & k = 3j - 2 \\ A_{yj}^e & k = 3j - 1 \\ A_{zj}^e & k = 3j \end{cases} \quad (2.24b)$$

Using Galerkin formulation, we obtain

$$\begin{aligned} & \sum_{j=1}^{24} \left\{ \int_{\Omega_e} \left(\frac{1}{\mu} \nabla \times \bar{N}_i \right) \cdot \left(\nabla \times \bar{N}_j \right) + \left(\frac{1}{\mu} \nabla \cdot \bar{N}_i \right) \left(\nabla \cdot \bar{N}_j \right) dV \right\} A_j^e + \\ & \sum_{j=1}^{24} \left\{ \int_{\Omega_e} j \omega \sigma \bar{N}_i \cdot \bar{N}_j dV \right\} A_j^e + \sum_{j=1}^8 \left\{ \int_{\Omega_e} \sigma \bar{N}_i \cdot \nabla N_j dV \right\} V_j^e - \\ & \int_{\partial \Omega_e} \bar{N}_i \cdot \left(\frac{1}{\mu} \nabla \times \bar{A} \times n \right) dS - \int_{\partial \Omega_e} \bar{N}_i \cdot \left(n \frac{1}{\mu} \nabla \cdot \bar{A} \right) dS = \int_{\Omega_e} \bar{N}_i \cdot \bar{J}_s dV \end{aligned} \quad (2.25a)$$

for $i = 1, 2, \dots, 24$

2.5 Boundary Conditions

In order to get a unique solution, certain boundary conditions are required before solving the system of equations. Either Dirichlet boundary conditions (values of \bar{A} or V on the boundary) or Neumann boundary conditions (values of \bar{B} or \bar{H} on the boundary) should be specified. Since Neumann boundary conditions are usually included implicitly in the finite element formulation, we only need to impose Dirichlet boundary conditions.

2.6 Solution of Linear Algebraic Equations

The finite element procedure results in a linear algebraic system of equations which must be solved to determine the unknown coefficients of the shape functions. There are two approaches to solving the system: direct methods and iterative methods. Gaussian elimination is a fundamental method to solve the general full or sparse matrix equations. In the finite element method, the resulting stiffness matrix is usually sparse and banded, and hence compared to direct methods, iterative methods are more advantageous with respect to computational cost and data storage.

For a system of dimension N , a general Gaussian elimination algorithm approximately requires $\frac{N^3}{3}$ multiplications and additions; Gaussian elimination algorithm incorporating banded matrix storage requires about $\frac{NB^2}{2}$ multiplications and additions, where B is the half-bandwidth (the maximum distance that a non-zero entry is away from the diagonal).

Direct methods are commonly used to solve general linear systems. However they do not fully exploit the sparse matrix structure generated by finite element procedure; furthermore, direct methods for sparse systems are difficult to adapt to parallel architecture computers. A number of iterative methods have been developed, but few are applicable to the general complex-valued matrix equations arising in eddy current problems. Transpose Free Quasi-Minimal-Residual (TFQMR) method is one of the applicable approaches.

Given a sparse matrix A and vector b , the associated Krylov subspace is $K_n = \text{span}\{b, Ab, A^2b, \dots, A^{n-1}b\}$. The exact solution $x = A^{-1}b$ could be approximated by $x_n \in K_n$ that minimizes the norm of the residual $r_n = b - Ax_n$. The TFQMR algorithm relaxes this minimization requirement, it aims to minimize a different, data-dependent norm that in practice is similar to $\|r_n\|$. An important issue in iterative methods is its convergence. The convergence of iteration depends on the properties of matrix, such as eigenvalues, the singular value or condition number. Usually a large condition number will result in large solution error or even non-convergence. Thus the process of “preconditioning” is essential for the success of iterative methods. In this thesis, we apply the incomplete LU (ILU) preconditioning technique. The overall solution procedure requires $O(N)$ multiplications and additions [26]-[28].

Before describing the TFQMR algorithm, we need to introduce the Biconjugate gradient (Bi-CG) algorithm. This method does not require the k -th residual r_k to satisfy the minimization principle. In stead, the k -th residual must satisfy the bi-orthogonality condition

$$r_k^T w = 0 \text{ for all } w \in K_k \quad (2.28)$$

At k -th iteration step, it produces two residuals r_k, \hat{r}_k and search directions p_k, \hat{p}_k such that bi-orthogonality holds, that is

$$\hat{r}_k^T r_l = 0 \text{ if } k \neq l \quad (2.29a)$$

and the search directions satisfy the bi-conjugate property

$$\hat{p}_k^T A p_l = 0 \text{ if } k \neq l \quad (2.29b)$$

The algorithm is as follows

Algorithm 2.6.1. Biconjugate gradient (Bi-CG)

1. $r = b - Ax, \hat{r} = r, \rho_0 = 1, \hat{p} = p = 0$
2. for $k = 1, 2, 3, \dots$
 - a) $\rho_k = \hat{r}_{k-1}^T r_{k-1}, \beta_k = \rho_k / \rho_{k-1}$
 - b) $p_k = r_{k-1} + \beta_k p_{k-1}, \hat{p}_k = \hat{r}_k + \beta_k \hat{p}_{k-1}$
 - c) $v_k = A p_k$
 - d) $\alpha_k = \rho_k / (\hat{p}_k^T v_k)$
 - e) $x_k = x_{k-1} + \alpha_k p_k$
 - f) $r_k = r_{k-1} - \alpha_k v_k, \hat{r}_k = \hat{r}_k - \alpha_k A^T \hat{p}_k$
 terminate if $\|r_k\|_2 > \varepsilon \|b\|_2$

We note that there exists $p_k \in P_k$ such that both

$$r_k = p_k(A)r_0 \text{ and } \hat{r}_k = p_k(A^T)\hat{r}_0 \quad (2.30)$$

So the product $\hat{r}_k^T r$ in step 2b of BiCG can be given without using A^T by

$$r_k^T \hat{r}_k = (p_k(A)r_0)^T (p_k(A^T)\hat{r}_0) = (p_k(A)^2 r_0)^T \hat{r}_0$$

Similarly, α can be given without using A^T , results in a modified method Conjugate Gradient Squared (CGS) algorithm as follows

Algorithm 2.6.2. Gradient Squared (CGS)

$$1. x_0 = x, p_0 = u_0 = r_0 = b - Ax,$$

$$v_0 = Ap_0, \hat{r}_0 = r_0, \rho_0 = \hat{r}_0^T r_0$$

2. for $k = 1, 2, \dots$

$$a) \sigma_{k-1} = \hat{r}_0^T v_{k-1}$$

$$b) \alpha_{k-1} = \rho_{k-1} / \sigma_{k-1}$$

$$c) q_k = u_{k-1} - \alpha_{k-1} v_{k-1}$$

$$d) x_k = x_{k-1} + \alpha_{k-1} (u_{k-1} + q_k)$$

$$r_k = r_{k-1} - \alpha_{k-1} A(u_{k-1} + q_k), \text{ terminate if } \|r_k\|_2 > \varepsilon \|b\|_2$$

$$e) \rho_k = \hat{r}_0^T r_k, \beta_k = \rho_k / \rho_{k-1}$$

$$u_k = r_k + \beta_k q_k$$

$$p_k = u_k + \beta_k (q_k + \beta_k p_{k-1})$$

$$v_k = Ap_k$$

It is shown [26] that the residual polynomial $p_k(z)$ in (2.30) can be given by

$$p_k(z) = p_{k-1}(z) - \alpha_{k-1} z q_{k-1}(z) \quad (2.31a)$$

where the auxiliary polynomial $q_k(z)$ satisfies $q_0 = 1$ and

$$q_k(z) = p_k(z) + \beta_k q_{k-1}(z) \quad (2.31b)$$

and the CGS residual r_k satisfying

$$r_k = p_k(A)^2 r_0 \quad (2.32)$$

Now we define two sequences y_m, w_m by

$$y_m = \begin{cases} u_{k-1} & \text{if } m = 2k - 1 \text{ is odd} \\ q_k & \text{if } m = 2k \text{ is even} \end{cases} \quad (2.33a)$$

and

$$w_m = \begin{cases} p_k(A)^2 r_0 & \text{if } m = 2k - 1 \text{ is odd} \\ p_k(A) p_{k-1}(A) r_0 & \text{if } m = 2k \text{ is even} \end{cases} \quad (2.33b)$$

If the algorithm successfully works, then $\alpha_k \neq 0$ and we can obtain

$$Ay_m = (w_m - w_{m-1}) / \alpha_{\lfloor (m-1)/2 \rfloor} \quad (2.34)$$

where $\lfloor r \rfloor$ denotes the nearest integer less than or equal to a real r . In matrix form, we can have

$$AY_m = W_{m+1} B_m \quad (2.35)$$

where Y_m is the $N \times m$ matrix with columns $\{y_j\}_{j=1}^m$, W_{m+1} the $N \times (m+1)$ matrix with columns $\{w_j\}_{j=1}^{m+1}$, and B_m is the $(m+1) \times m$ matrix given by

$$B_m = \begin{pmatrix} 1 & 0 & \cdots & 0 \\ -1 & 1 & \ddots & \vdots \\ 0 & \ddots & -1 & 1 \\ 0 & \cdots & 0 & -1 \end{pmatrix} \text{diag}(\alpha_0, \alpha_0, \dots, \alpha_{\lfloor (m-1)/2 \rfloor})^{-1} \quad (2.36)$$

Successful completion of the algorithm also implies that K_m is the span of $\{y_j\}_{j=1}^m$, therefore

$$x_m = x_0 + Y_m z \quad (2.37)$$

for some $z \in R^m$. Thus

$$r_m = r_0 - AY_m z = W_{m+1} (e_1 - B_m z) = W_{m+1} \Omega_{m+1}^{-1} (f_{m+1} - H_m z) \quad (2.38)$$

where

$$e_1 = (1, 0, \dots, 0)^T \in R^m,$$

$$\Omega_m = \text{diag}(\omega_1, \omega_2, \dots, \omega_m), \text{ using to improve the conditioning of matrix } W_{m+1},$$

$$f_{m+1} = \Omega_{m+1} e_1, \quad H_m = \Omega_{m+1} B_m$$

The TFQMR algorithm is to find solution by solving the least square problem

$$\text{minimize}_{z \in R^m} \| f_{m+1} - H_m z \|_2 \quad (2.39)$$

which is a quasi-minimum residual. And x_m is given by

$$x_m = x_0 + Y_m z_m \quad (2.40)$$

The algorithm is as follows

Algorithm 2.6.3. Transpose Free Quasi-Minimum Residual (TFQMR)

1. $w_1 = y_1 = r_0 = b - Ax$, $u_1 = v = Ay_1$, $d = 0$

$$\rho_0 = r_0^T r_0, \tau = \|r\|_2, \theta = 0, \eta = 0$$

2. for $k = 1, 2, 3, \dots$

a) $\sigma_{k-1} = r_0^T v$, $\alpha = \rho_{k-1} / \sigma_{k-1}$, $y_2 = y_1 - \alpha_{k-1} v$, $u_2 = Ay_2$

b) For $j = 1, 2$ ($m = 2k - 2 + j$)

$$w = w - \alpha_{k-1} u_j$$

$$d = y_j + (\theta^2 \eta / \alpha_{k-1}) d$$

$$\theta = \|w\|_2 / \tau, c = 1 / \sqrt{1 + \theta^2}$$

$$\tau = \tau \theta c, \eta = c^2 \alpha_{k-1}$$

$$x = x + \eta d$$

if $\tau \sqrt{m+1} \leq \varepsilon \|b\|_2$ terminate successfully

c) $\rho_k = r_0^T w$, $\beta = \rho_k / \rho_{k-1}$

d) $y_1 = w + \beta y_2$, $u_1 = Ay_1$

e) $v = u_1 + \beta(u_2 + \beta v)$

2.7 Post Processing

After solving the linear algebraic system of equations, we get a numerical solution in terms of magnetic vector potential \bar{A} and electric scalar potential V . But these potentials are of little value due to the lack of experimental measurements for comparison. In order to have experimental comparison, magnetic flux density \bar{B} or electric current density \bar{J} need be calculated.

In terms of potential \bar{A} , the magnetic flux density $\bar{B} = \nabla \times \bar{A}$ can be written in component form as

$$B_x = \frac{\partial A_z}{\partial y} - \frac{\partial A_y}{\partial z} \quad (2.41a)$$

$$B_y = \frac{\partial A_x}{\partial z} - \frac{\partial A_z}{\partial x} \quad (2.41b)$$

$$B_z = \frac{\partial A_y}{\partial x} - \frac{\partial A_x}{\partial y} \quad (2.41c)$$

In each element, B is assumed to be constant, and could be calculated by

$$B_x = \sum_{i=1}^8 \left(\frac{\partial N_i}{\partial y} A_{zi} - \frac{\partial N_i}{\partial z} A_{yi} \right) \quad (2.42)$$

We could get similar form for B_y and B_z .

The current density J inside an element is evaluated through equation $\bar{J} = -j\omega\sigma\bar{A} - \sigma\nabla V$ at the element center.

$$J_x = -j\omega\sigma A_x - \sigma \frac{\partial V}{\partial x} = -j\omega\sigma \sum_{i=1}^8 N_i A_{xi} - \sigma \sum_{i=1}^8 \frac{\partial N_i}{\partial x} V_i \quad (2.43)$$

The components J_y and J_z can be calculated using similar expressions.

CHAPTER 3. FEM RESULTS AND DISCUSSIONS

This chapter describes the development of finite element method for simulating Magneto-Optic inspection (MOI). The FEM for MOI serves as a test bed for generating signals from a variety of crack and corrosion geometries. The model can also be used for optimizing parameters of the testing. In this chapter, we present the results of parametric studies on experimental MO images.

3.1 Model Validation

Figure 1.4 shows the schematic of the MOI instrument. A copper foil carrying time-varying harmonic currents is used to induce eddy current in the test sample. An induction foil of thickness 0.04 mm is placed above the sample at a distance of 0.35 mm . The test specimen is a 1.5 mm thick aluminum plate similar to that used in aircraft skin. A 6.35 mm diameter hole and 3.18 mm long notch emanating from the hole is introduced in the plate as shown in Figure 3.1.

The parameters used in the test are summarized in Table 3.1.

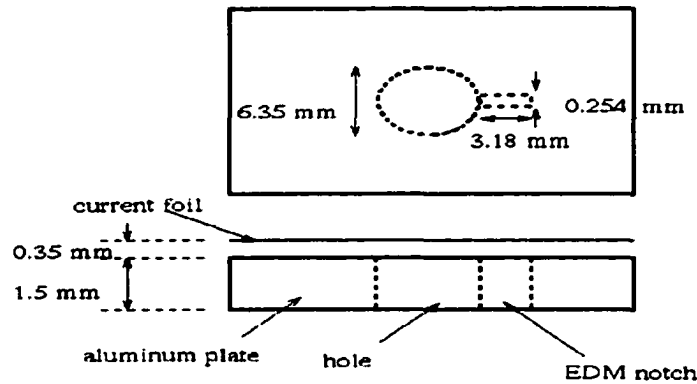


Figure 3.1 Geometry of hole with EDM notch.

Table 3.1 Parameters used in model validation.

Thickness of Aluminum plate	1.5 mm
Diameter of hole	6.35 mm
Length of the EDM notch	3.18 mm
Width of the EDM notch	0.254 mm
Density of source current	10^8 A/m^2
Frequency of source current	50 kHz
Conductivity of aluminum plate	$1.8867 \times 10^7 \text{ S/m}$

The finite element model is based on $A-V$ formulation, and the solution domain is of dimension $[-1616] \times [-30 \ 30] \times [-30 \ 30] \text{ mm}$. Both Dirichlet and Neumann boundaries are applied, and are listed in Table 3.2. Figure 3.2 shows the mesh used around the region of interest and the induced currents around the hole that generates flux leakage (B_x) normal to the sample plate. The field is calculated at $x = 0.45 \text{ mm}$ where the sensor is placed. The peak value of B_x is 16.7 G near the notch tip. This result agrees with the calculation by Infolytica

Corporation in Montreal, Canada [11]. When the current density was taken to be $0.75 \times 10^8 \text{ A/m}^2$, the largest flux leakage calculated was 13G near the notch tip using software MAGNETS5 by Infolytica. The relative difference between the two is less than 3.7%.

Table 3.2 Boundary conditions.

Upper boundary ($x = 16 \text{ mm}$)	$A_x = A_y = A_z = 0, V = 0$
Lower boundary ($x = -16 \text{ mm}$)	$A_x = A_y = A_z = 0, V = 0$
Left boundary ($y = -30 \text{ mm}$)	$A_x = 0, V = 0, A_y, A_z \text{ free}$
Right boundary ($y = 30 \text{ mm}$)	$A_x = 0, V = 0, A_y, A_z \text{ free}$
Front boundary ($z = -30 \text{ mm}$)	$A_x = 0, V = 0, A_y, A_z \text{ free}$
Rear boundary ($z = 30 \text{ mm}$)	$A_x = 0, V = 0, A_y, A_z \text{ free}$

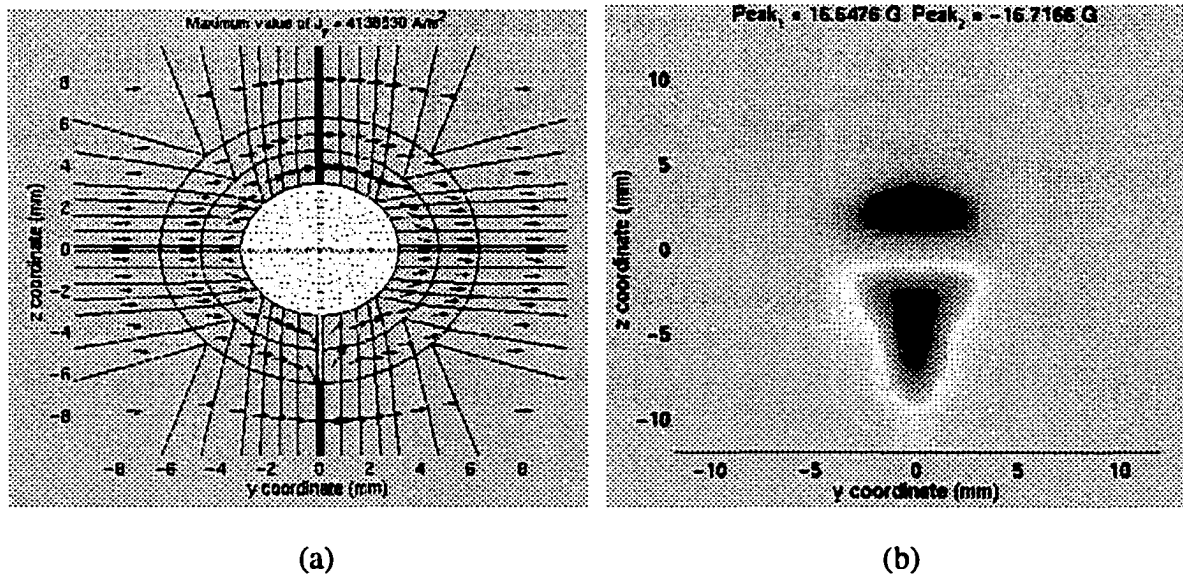


Figure 3.2 (a) Mesh on y-z plane and induced current around the hole and notch. (b) MO image of flux leakage at the sensor substrate.

3.2 Corrosion Dome in Single Layer

3.2.1 Geometry and Parameters

This section presents the studies on subsurface corrosion. The inspected geometry consists of an aluminum plate of thickness 1.5 mm with a corrosion dome of diameter 19 mm and height h introduced on the lower side as shown in Figure 3.3.

Table 3 lists the parameters used in the test. Figure 3.4 shows the region of interest in $y-z$ plane and $z-x$ plane discretized using a $23 \times 21 \times 21$ mesh.

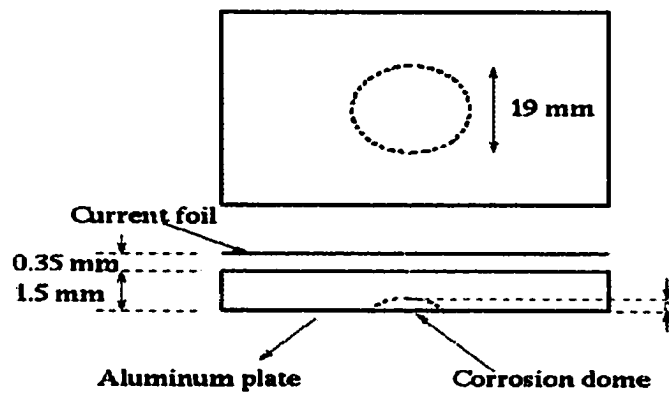


Figure 3.3 Geometry of single layer aluminum plate.

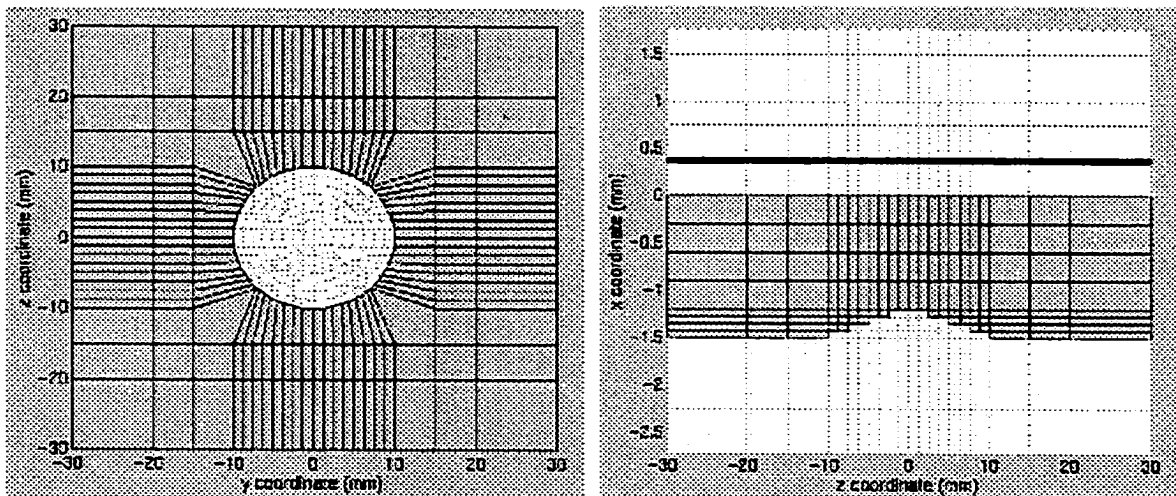


Figure 3.4 Mesh of the region of interest.

Table 3.3 Parameters used in single layer plate test.

Thickness of Aluminum plate	1.5 mm
Diameter of corrosion dome	19 mm
Depth of corrosion dome	h
Density of source current	10^8 A/m^2
Frequency of source current	1.0 kHz
Conductivity of aluminum plate	$1.8867 \times 10^7 \text{ S/m}$

3.2.2 Effect of the Corrosion Depth

The source current in the copper foil is shown in Figure 3.5. The time-varying source induces eddy currents inside the aluminum plate. Figure 3.6 (a)-(c) show the induced current in three cross sectional planes. Due to the induced current, a flux leakage (B_x) is generated normal to the sample plate. The depth of the corrosion dome is varied from 10% to 40% of the plate thickness. The distribution of B_x at the sensor substrate is plotted for 10% , 20% , 30% , 40% corrosion dome depth as shown in Figure 3.7 (a)-(d). It is observed that the peak value of flux leakage at the sensor substrate increases with the depth of the corrosion dome, which agrees with the experimental results.

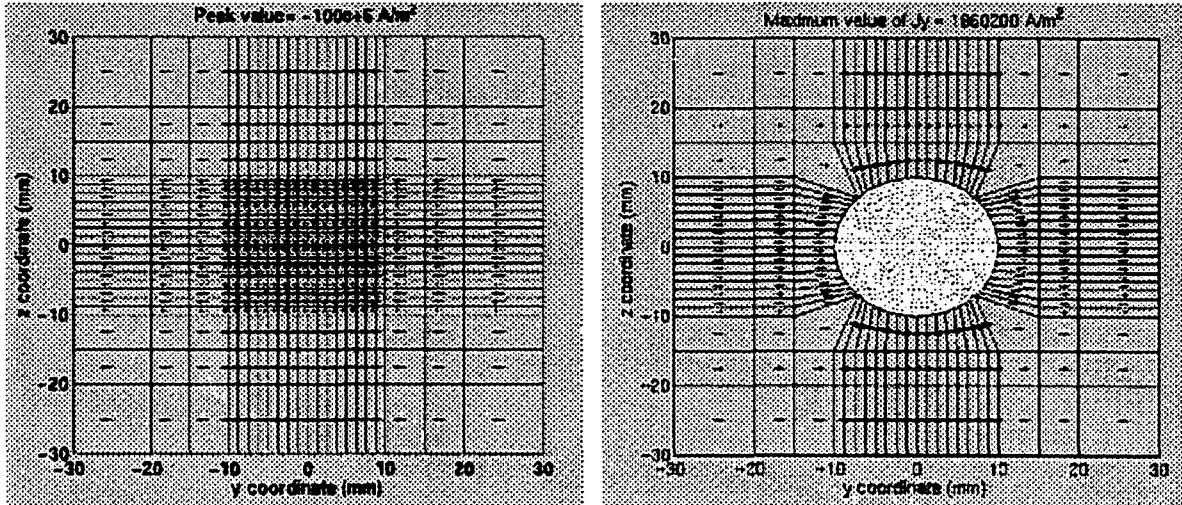
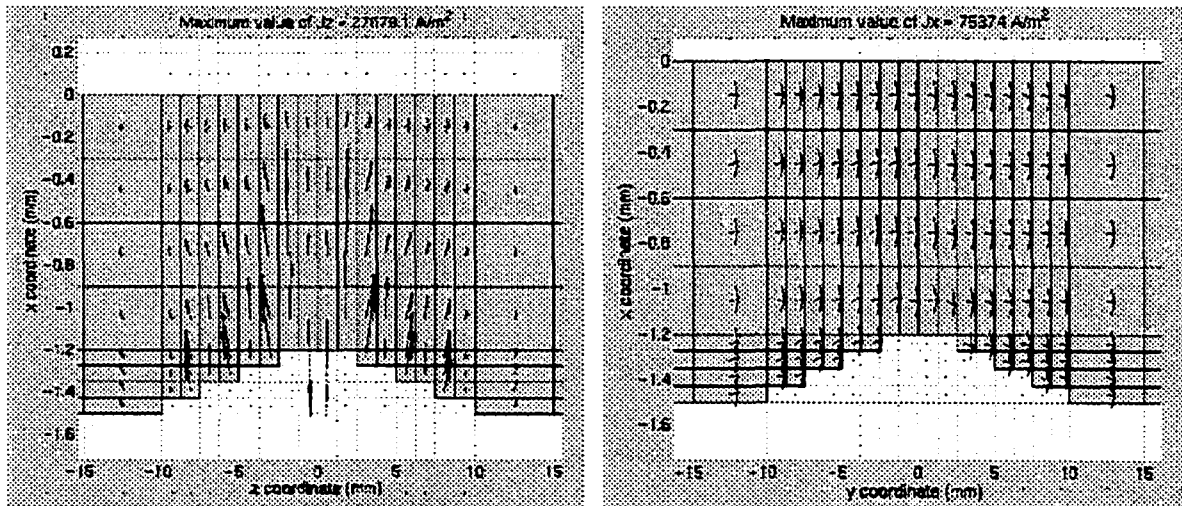


Figure 3.5 Source current in copper foil.

(a)



(b)

(c)

Figure 3.6 (a) Induced current in y-z plane. (b) Induced current in z-x plane. (c) Induced current in x-y plane.

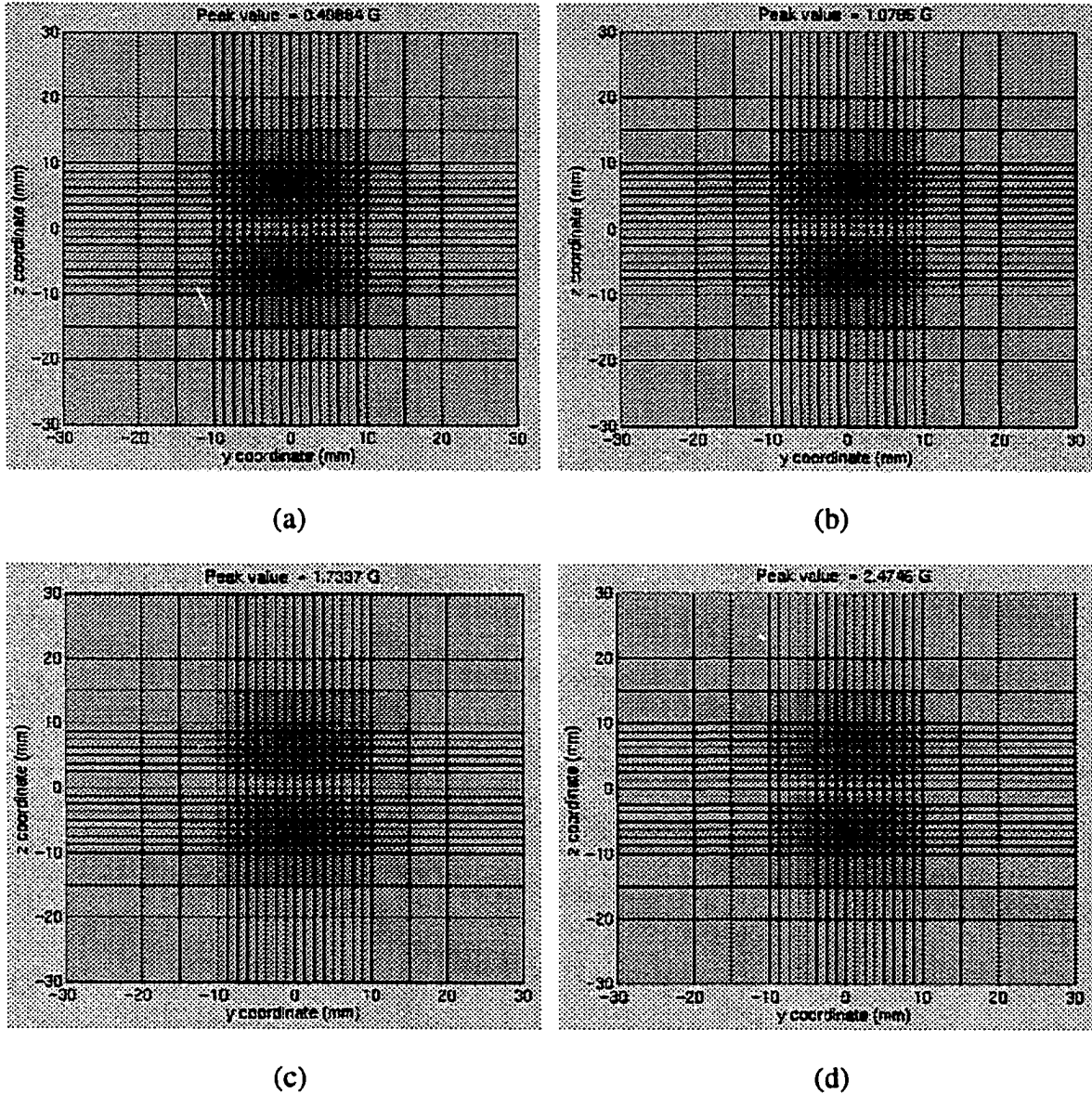


Figure 3.7 Numerical MO images of flux leakage at sensor layer for corrosion domes with different depth. (a) 10%, (b) 20%, (c) 30%, (d) 40%.

3.3 Corrosion Dome in Double Layers

Generally corrosion may occur in multiplayer structures. This section presents the finite element model and results of corrosion dome in a double layer aluminum structure.

3.3.1 Corrosion at the Bottom of the First Layer

Figure 3.8 shows the geometry of corrosion dome at the bottom of the first layer in a two-layer geometry. The parameters used in calculation are same as those in Table 3.3. The depth of the corrosion dome is varied from 10% to 40% of the plate thickness. The distribution of flux leakage at the sensor substrate is plotted in Figure 3.9 (a)-(d) respectively for 10% , 20% , 30% , 40% depth.

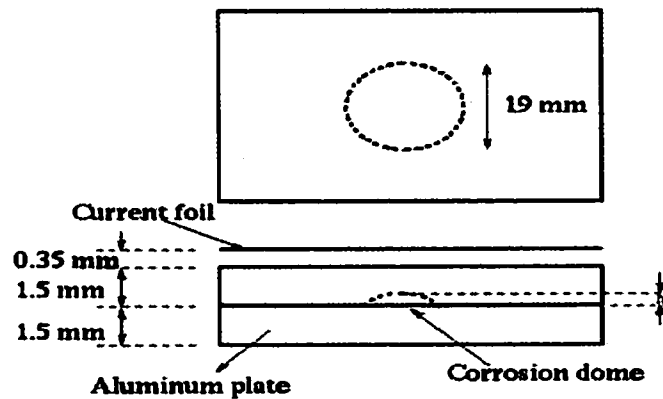


Figure 3.8 Geometry of double layers.

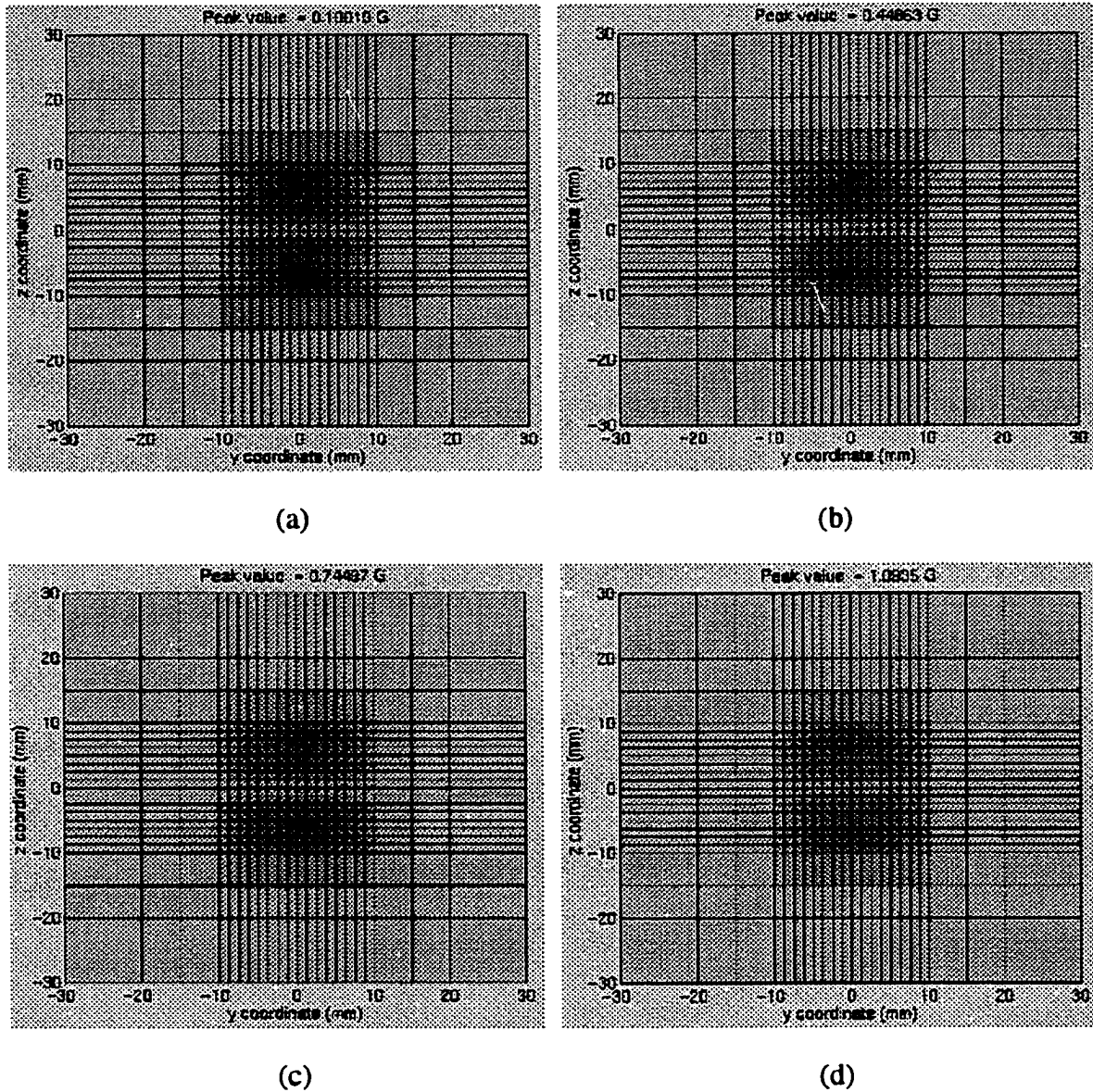


Figure 3.9 Numerical MO images of flux leakage at sensor layer for corrosion domes with different depth. (a) 10%, (b) 20%, (c) 30%, (d) 40%.

Compared with the single layer case, it can be seen that the presence of the second layer reduces the flux leakage B_x by a factor of 2. The additional layer reduces the strength of induced eddy current in the first layer, thus results in the decrease of B_x . Figure 3.10 shows the peak values of flux leakage as a function of depth h of the corrosion dome. The results

agree with the experimental observation that the MOI instrument can detect a 10% corrosion dome in a single layer plate, but can only detect a 20% corrosion dome in presence of second layer plate.

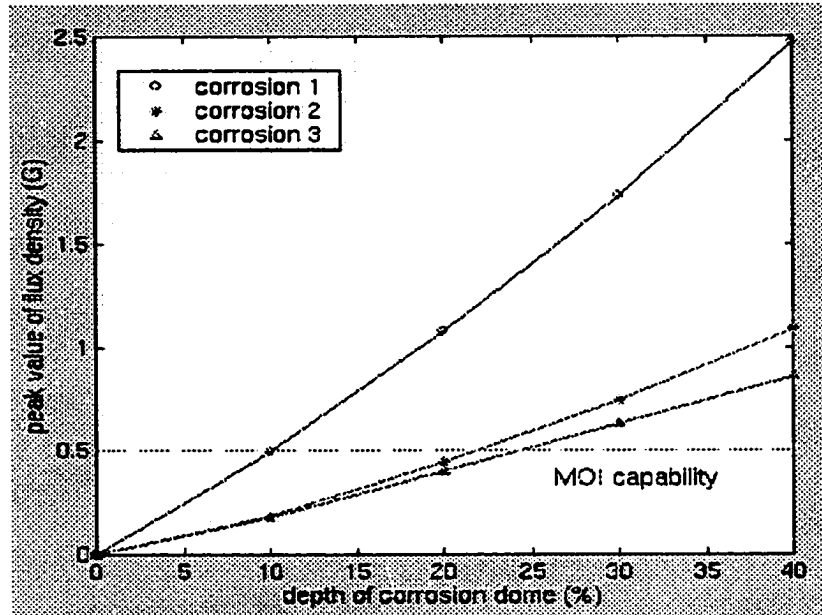


Figure 3.10 Peak values of flux leakage versus corrosion depth.

Corrosion 1: corrosion dome at the bottom of single layer.

Corrosion 2: corrosion dome at the bottom of the first layer in two-layer geometry.

Corrosion 3: corrosion dome at the top of the second layer in two-layer geometry.

3.3.2 Corrosion at the Top of the Second Layer

Corrosions may also occur in second layer. In order to study the effect of corrosion location, corrosion dome at the top of the second layer was modeled. Figure 3.11 shows the geometry of corrosion dome at the top of the second layer. The parameters used in calculation are same as Table 3.3. The distribution of flux leakage at the sensor substrate is plotted in Figure 3.12 (a)-(d) with respect to different corrosion depth.

For the same corrosion depth, the peak value of the flux leakage for the corrosion at the top of the second layer is smaller than that at the bottom of the first layer as observed experimentally.

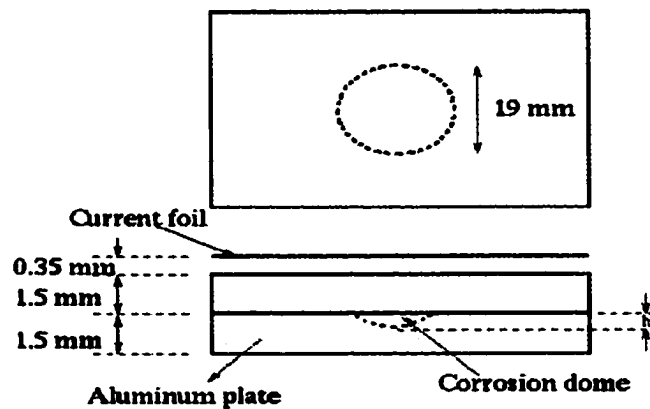


Figure 3.11 Geometry of double layers.

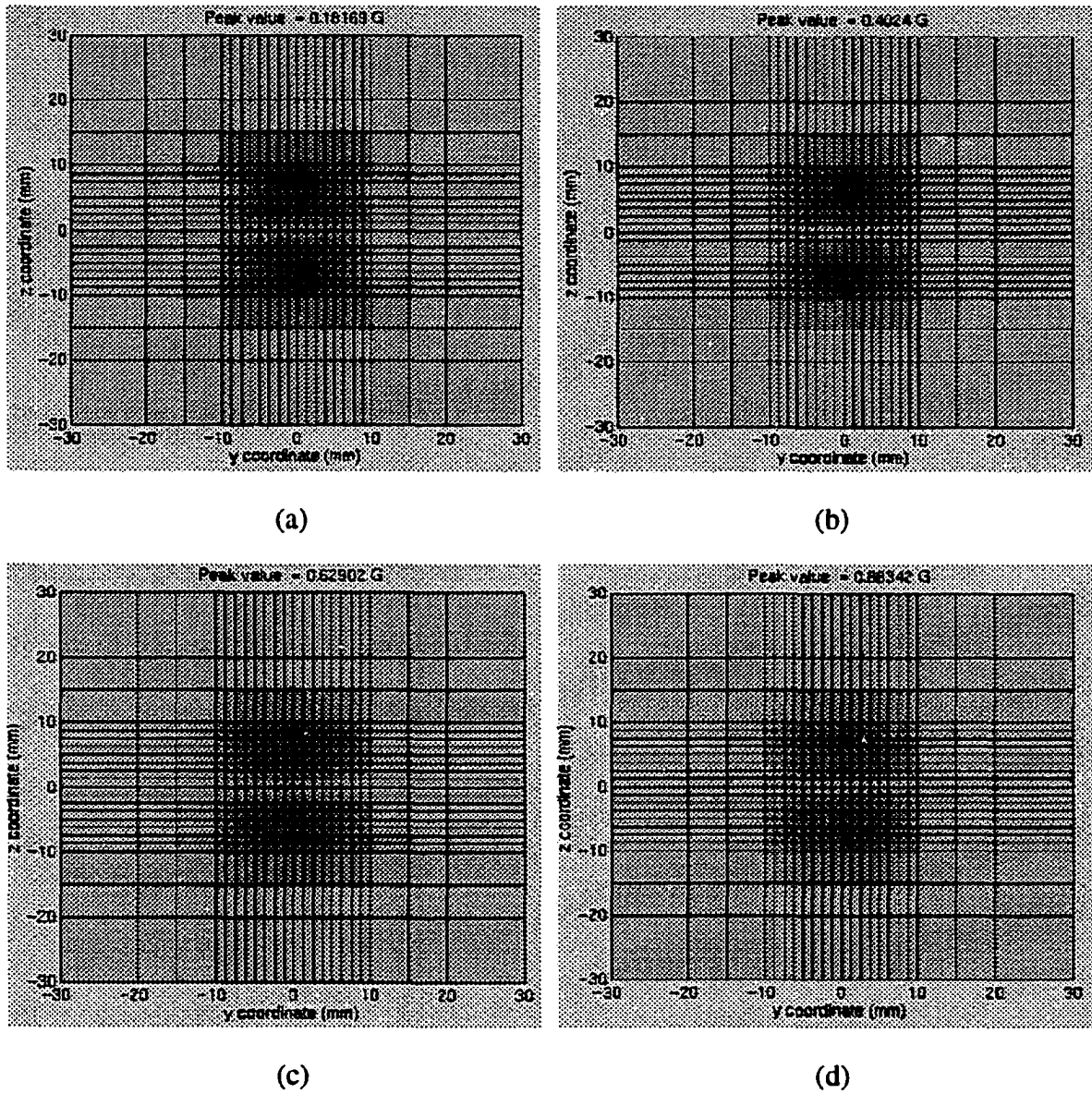


Figure 3.12 Surface plot of flux leakage and its MO image for 40% corrosion dome.

3.4 Optimal Excitation Frequency

In the last two sections, we calculated the fields using an excitation frequency of 1 kHz . Next a study of the effect of frequency was conducted. The frequency affects the induced current inside the aluminum plate, and thus affects the generated fields. A 20% corrosion dome was modeled and the frequency was varied from 0.1 kHz to 5 kHz . Figure 3.13 shows the peak value of flux leakage as a function of excitation frequency. As we can see, the optimal frequency is 1 kHz for single layer case, and is reduced to 0.5 kHz when a second layer is present.

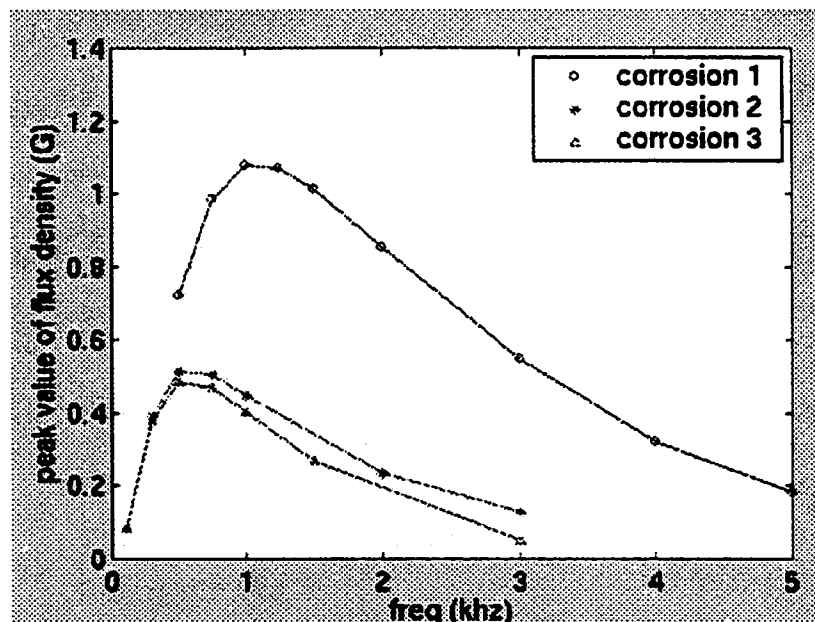


Figure 3.13 Peak values of flux leakage versus excitation frequency.

Corrosion 1: corrosion dome at the bottom of single layer.

Corrosion 2: corrosion dome at the bottom of the first layer in two-layer geometry.

Corrosion 3: corrosion dome at the top of the second layer in two-layer geometry.

3.5 Effect of Air Gap between Two Layers

Typically an air gap exists between different layers. This section presents the results obtained at various values of the air gap between the two layers. We still use 20% corrosion as an example. Air gaps of thickness of 0–0.5 mm were applied. The material parameters are same as those in Table 3.3. The corrosion dome could be located at the bottom of the first layer or the top of the second layer as shown in Figure 3.14.

When the corrosion is located at the bottom of the first layer, the peak value of flux leakage increases with the size of the air gap and tends to the value of a single layer case; In contrast, when the corrosion is located at the top of the second layer, the peak value of flux leakage decreases with the size of the air gap as shown in Figure 3.15.

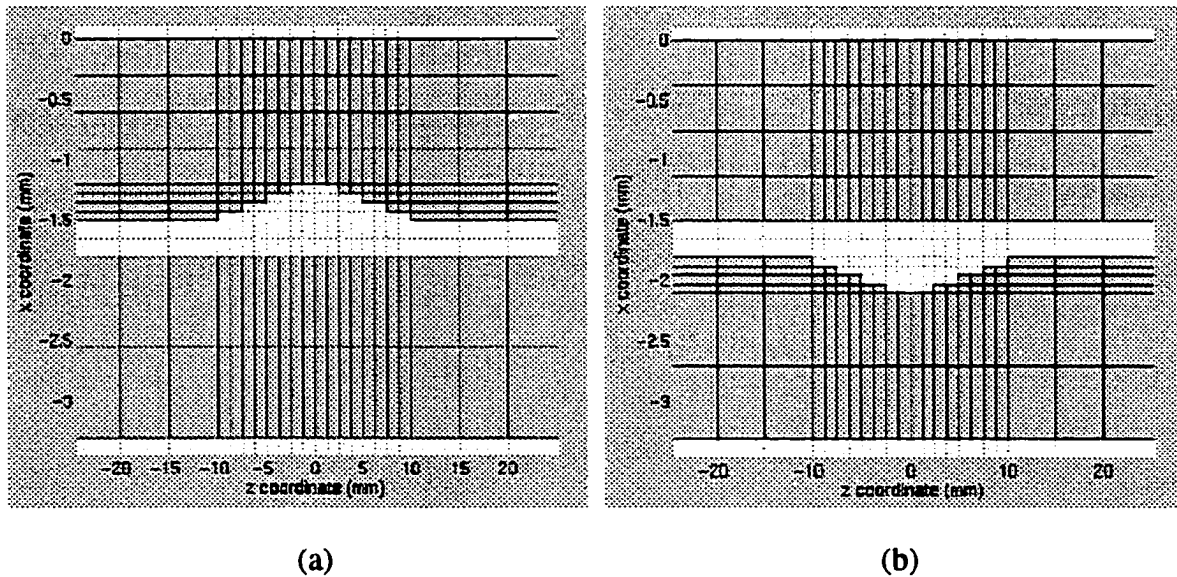


Figure 3.14 Geometry of corrosion dome with air gap between two layers.

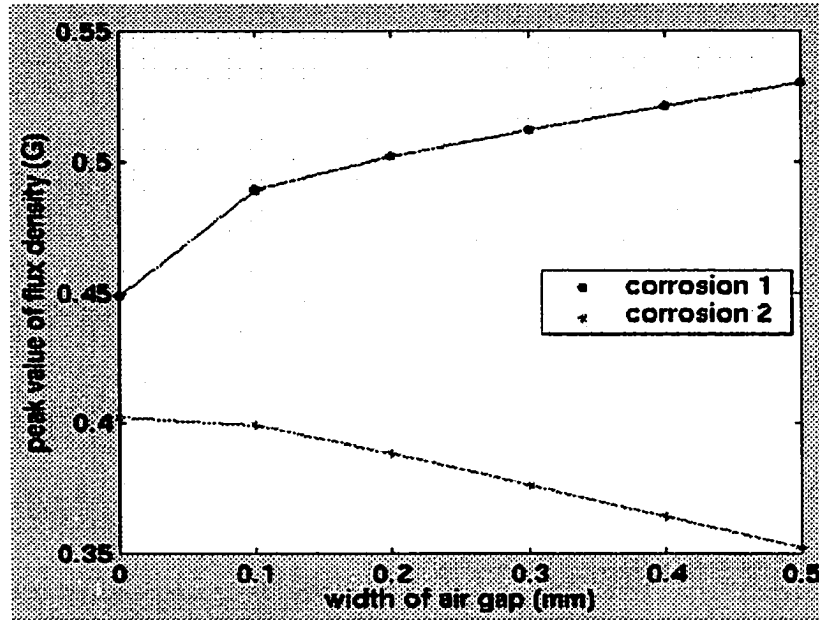


Figure 3.15 Peak value of flux leakage versus the size of air gap.

Corrosion 1: corrosion dome at the bottom of the first layer in two-layer geometry.

Corrosion 2: corrosion dome at the top of the second layer in two-layer geometry.

3.6 Effect of the Slope of the Corrosion

In practice, the shape of the corrosion is complex. This section presents the effect of corrosion dome slope on the resulting MO image. A single layer aluminum plate with 20% corrosion dome is modeled. Parameters used in the model are same as those listed in Table 3.3. The side view of corrosion domes with different slope and the corresponding MO images are shown in Figure 3.16 through Figure 3.19.

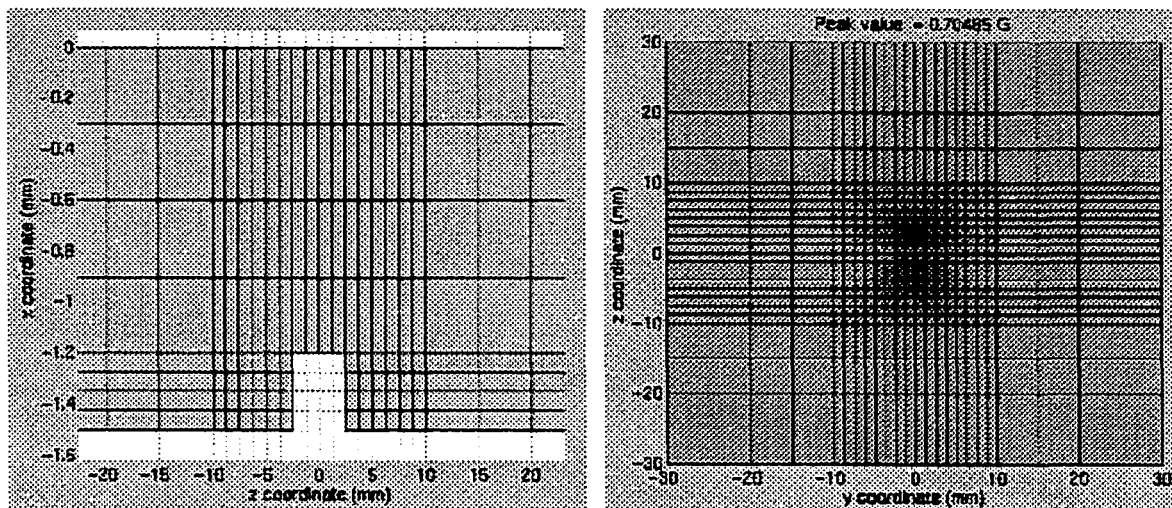


Figure 3.16 Side view of the geometry and the MO image of flux leakage.

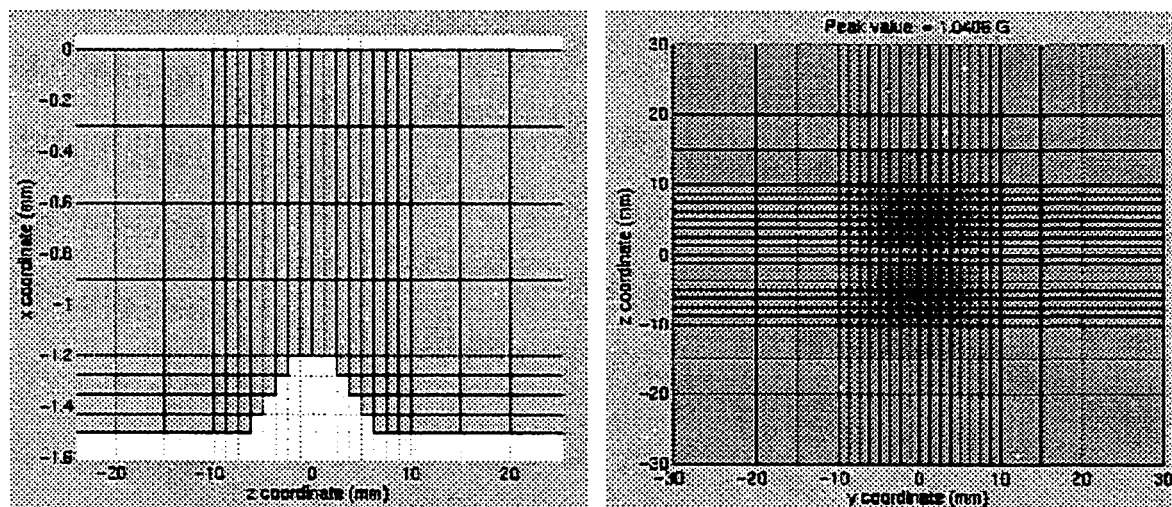


Figure 3.17 Side view of the geometry and the MO image of flux leakage.

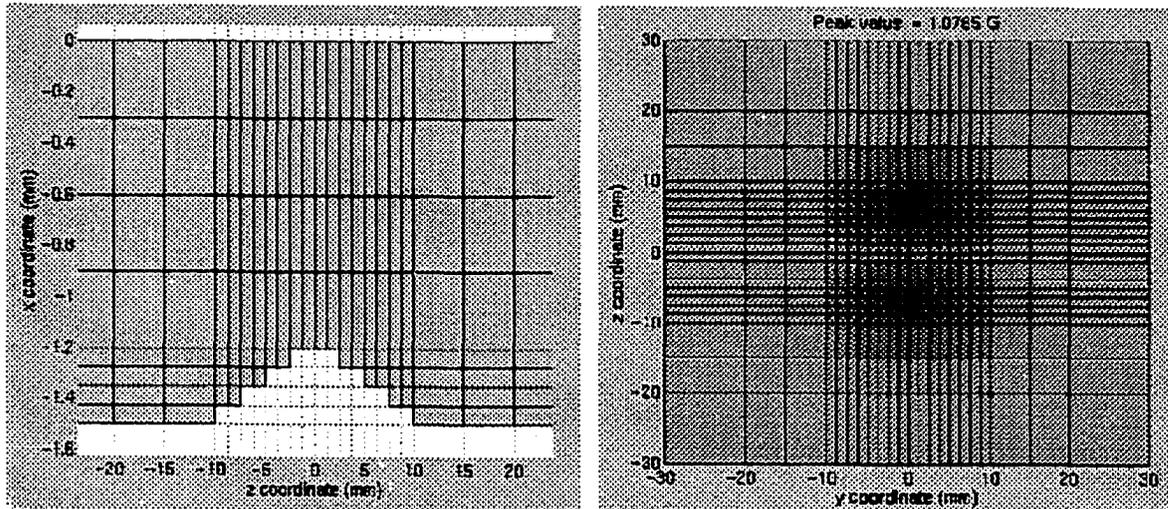


Figure 3.18 Side view of the geometry and the MO image of flux leakage.

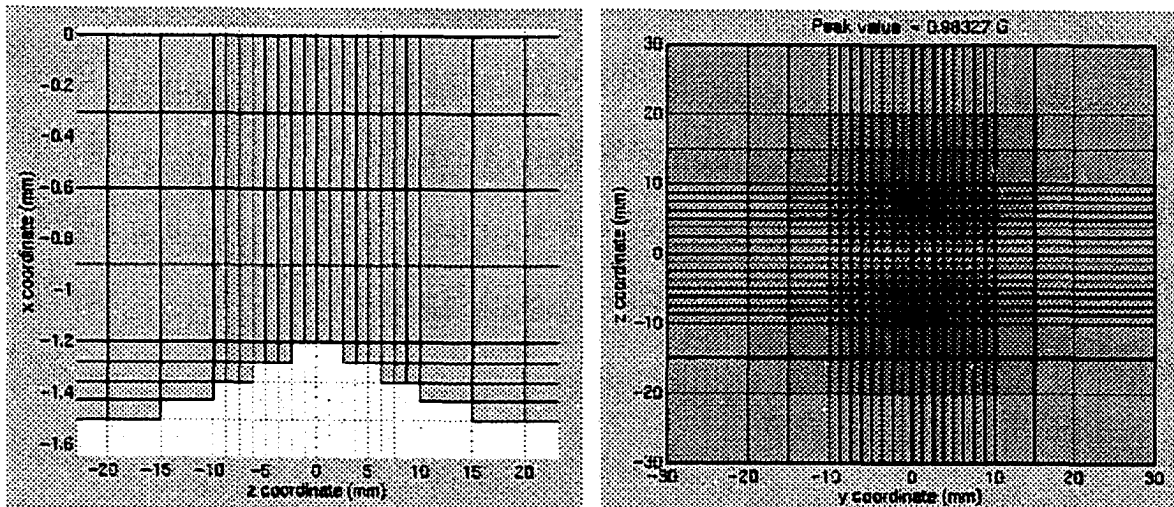


Figure 3.19 Side view of the geometry and the MO image of flux leakage.

We can see that the MO images of flux leakage vary widely with respect to different slopes of the corrosion dome. The images can therefore be used to characterize the shape of corrosion damage.

3.7 Effect of Edge

Practically, corrosions may occur near a lap joint, where an edge discontinuously lies in the vicinity of corrosion in the second layer of the sample. Figure 3.20 shows a z-edge geometry (edge is perpendicular to induction current source). This section presents the effect of a second layer edge on the MO image formed at the sensor. A 20% corrosion dome is modeled in the vicinity of a z-edge or y-edge (edge is parallel to induction current source) in the second layer. Parameters used in the test are same as those listed in Table 3.3. A side view of the corrosion dome and edge along with the corresponding MO images are shown in Figure 3.21 through Figure 3.24, x-y cross section is shown for z-edge case, and x-z cross section is shown for y-edge case. The edge is located at a distance of 5,10 mm to the corrosion center respectively.

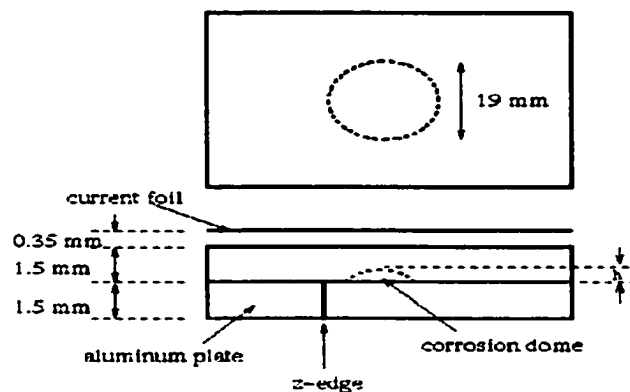


Figure 3.20 Geometry of double layer aluminum plate with z-edge.

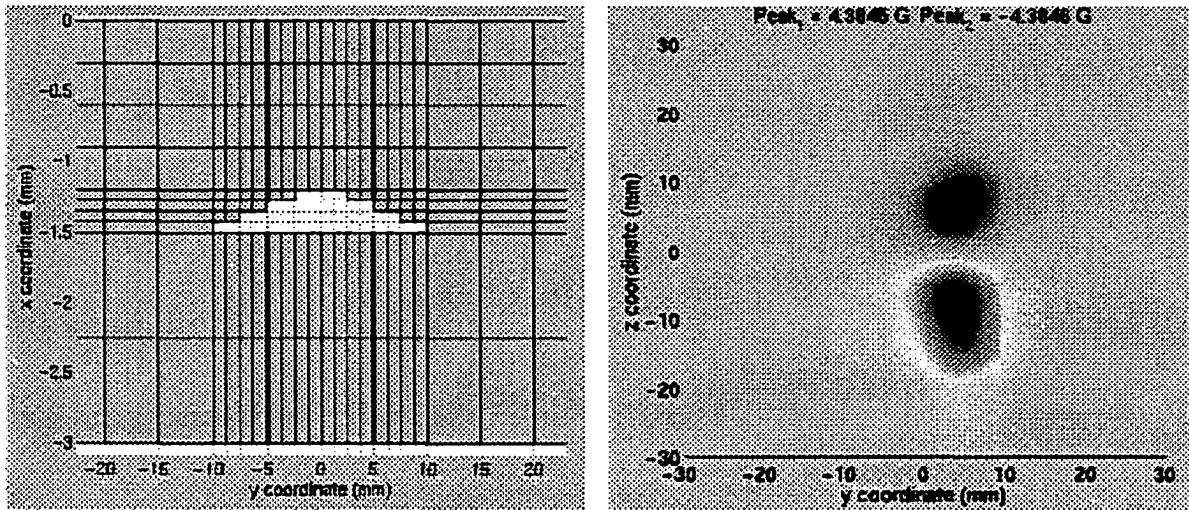


Figure 3.21 Geometry of z-edge and the MO image of flux leakage.

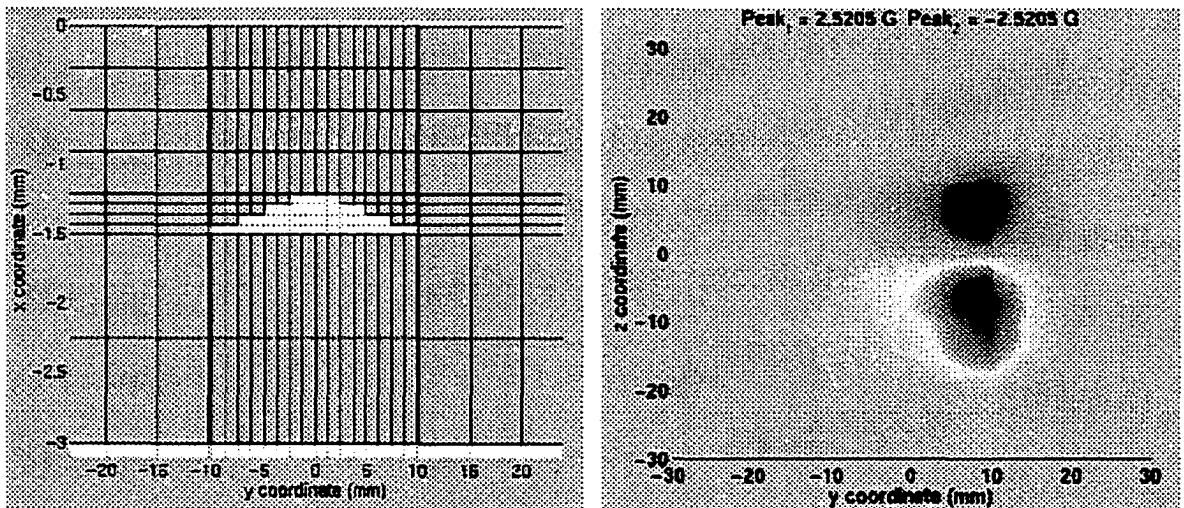


Figure 3.22 Geometry of z-edge and the MO image of flux leakage.

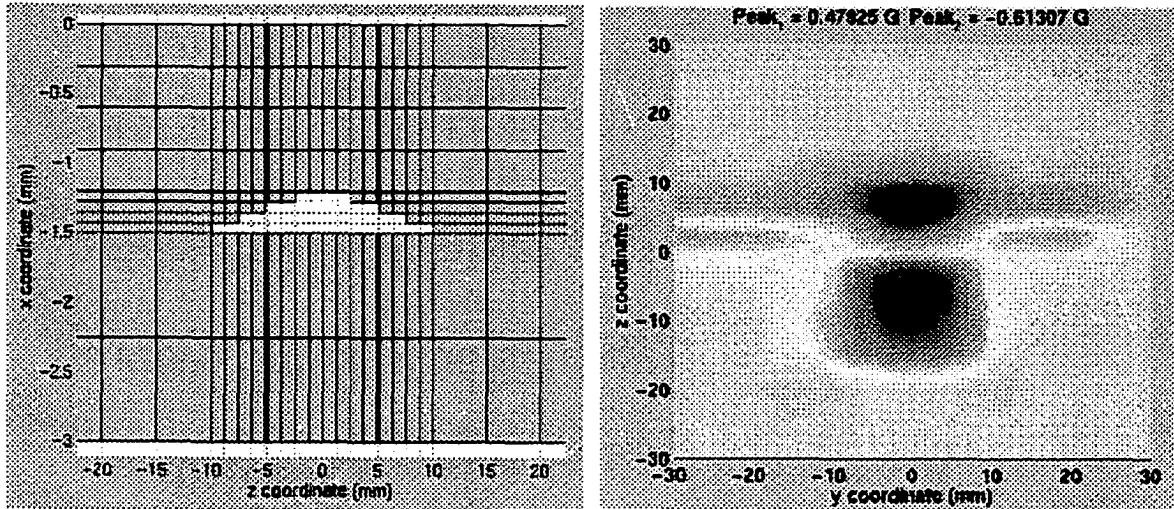


Figure 3.23 Geometry of y-edge and the MO image of flux leakage.

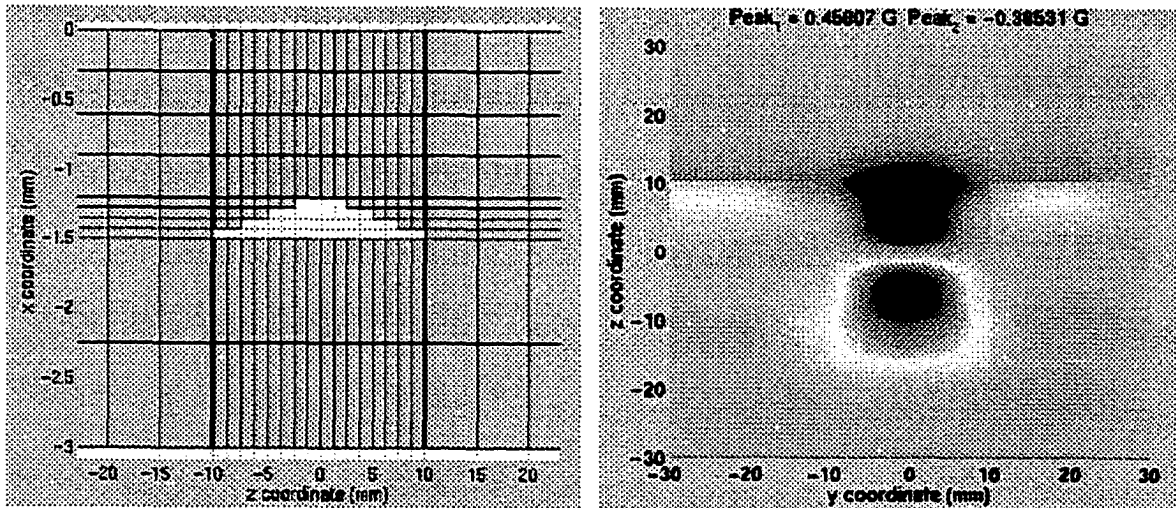


Figure 3.24 Geometry of y-edge and the MO image of flux leakage.

We can see that the MO image of corrosion dome is shifted away from the center when a z-edge is present, while y-edge is seen in the MO image. It is also observed that in the presence of edges, the peak value of flux leakage is enlarged. We can express the peak value of flux leakage as a function of the distance (h) between edge and corrosion center, as shown in Figure 3.26. The peak value of flux leakage decreases with h for z-edge case, but

this relationship becomes more complex in the case of a y-edge. A z-edge affects the peak value more distinctly than a y-edge.

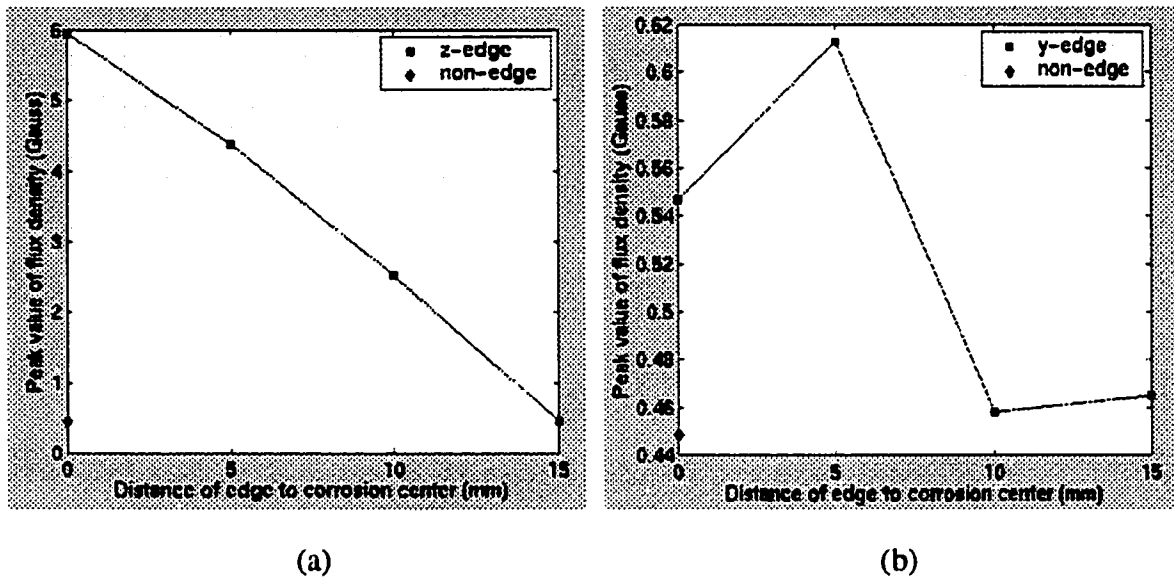


Figure 3.25 Peak value of flux leakage versus the distance between edge and corrosion center.

The next geometry presents a significant challenge for modeling. The geometry referred to as cracks under Fastener (CUF) (Figure 1.3) consists of three layers with a fastener hole and a fastener. The mesh is shown in Figure 3.26, and the parameters used in the test are summarized in Table 3.4.

In Figure 3.27a, we see the induced current flows around the rivet, it cannot pass through the rivet because of the air gap, while a relatively weak induced current is generated inside of rivet, these eddy currents in turn produce a leakage field above the rivet. Figure 3.27b shows the side view of the induced currents around rivet region, the eddy currents inside the rivet form loops in $x-y$ plane. Overall, the flux leakage will result in a binary image in the MO sensor as shown in Figure 3. 28.

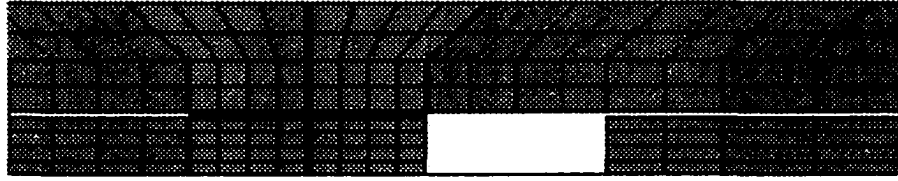


Figure 3.26 Geometry of rivet head with radial crack (crack length 3 mm)

Table 3.4 Parameters in test

Thickness of Aluminum plate	3 mm
Length of Radial Crack	3 mm
Width of Radial Crack	0.1 mm
Density of source current	10^8 A/m^2
Frequency of source current	1.5 kHz
Conductivity of aluminum plate	$1.8867 \times 10^7 \text{ S/m}$

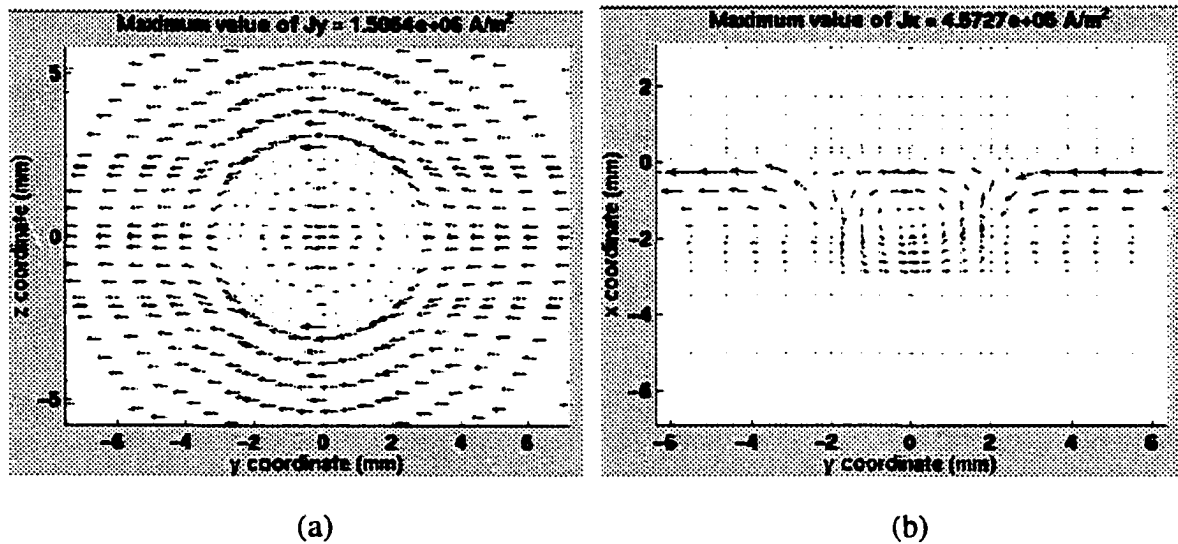


Figure 3.27 Eddy currents around rivet head region. (a) Top view, (b) Side view.

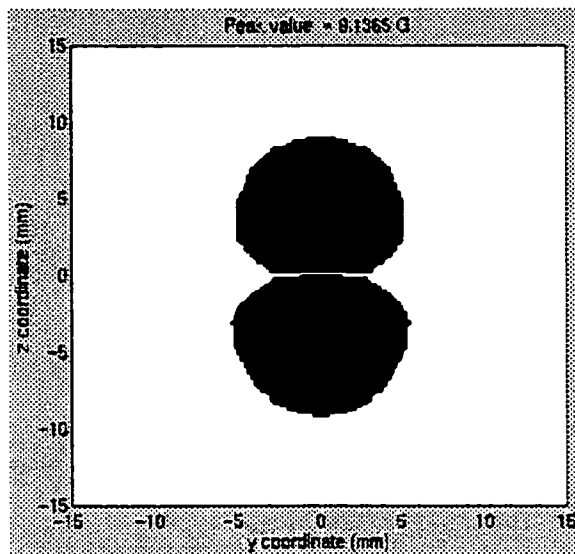


Figure 3.28 MO image for rivet head with a radial crack.

As we can see, this geometry includes very small air gap between the different metal layers resulting in a multiply connected regions. The modeling of the extremely small air gaps can result in a highly wasteful mesh, which becomes worse when a radial crack is introduced under the fastener in the third layer. A more efficient modeling technique was therefore needed to address this problem. In chapter 4, a recently developed meshless method [29] is introduced and applied to solve complex eddy current problems.

CHAPTER 4. ELEMENT FREE GALERKIN METHOD

4.1 Introduction

The finite element method (FEM) is a well established analysis technique that has been successfully applied in solving various problems in science and engineering. This method is based on the fundamental idea that a continuous function over the entire solution domain can be replaced by piecewise continuous approximation, usually polynomials, over a set of subdomains called finite elements. The interconnecting structure of the elements via nodes is called a finite element mesh. Reliance of the FE method on a mesh leads to some distinct disadvantages. Generation of a mesh for a complex geometry is in itself difficult and time consuming [30]. For example, in electromagnetic computation, problems that involve geometrical deformation such as inverse shape optimization, or large dynamic geometrical changes such as propagating cracks, the use of an underlying mesh creates difficulties in the treatment of discontinuities that might not necessarily coincide with the element boundaries. Usually re-meshing is required to handle the discontinuities at every step of the shape reconstruction. For such problems, developing a numerical method that does not rely on mesh is desirable.

Recently a new technique known as meshless method has been developed where the unknown function is approximated entirely in terms “local” functions defined at a set of nodes. Elements or usual relationship between nodes and elements is not necessary to construct a discrete set of equations. With the implementation of moving least square approximation with Galerkin formulation, meshless methods are now widely applied to

problems in fracture mechanics and static electromagnetics [29]-[34]. These methods are promising, although substantially more expensive than FEM in terms of construction of the mass matrices.

This disadvantage notwithstanding, the principal attractive feature of meshless methods is the possibility of (i) working with a cloud of points that describes the underlying structure exactly instead of relying on a tessellation, and (ii) using this method for inverse problems. The principal contributions of this paper are two-fold: (i) validation of the Element-Free Galerkin (EFG) method via comparison against standard FEM and analytical models; (ii) formulation and application of this technique to two dimension (2D) and three dimension (3D) static and quasi-static electromagnetic problems.

The organization of this chapter is as follows: Section 4.2 defines the problems that will be analyzed; Section 4.3 outlines the EFG method in two dimensions, while Section 4.4 presents the details of numerical implementation; Finally, Section 4.5 presents a series of results that both validate this model as well as demonstrate its applicability.

4.2 Mathematical Preliminaries

The interaction of static and low frequency electromagnetic fields with materials is the basic of Nondestructive Evaluation (NDE) of conducting samples. To simulate this interaction, the fields are typically expressed in terms of potentials and the governing equations for either the Poisson or the diffusion equation are solved together with appropriate boundary and initial conditions, i.e., In what follows, we analyze the application of the EFG method to the numerical solution of both these equations.

Consider a domain of interest denoted by Ω that is bounded by $S_1 \cup S_2 = \partial\Omega$, where S_1 is the Dirichlet boundary and S_2 is the Neumann boundary. The outward pointing normal to the boundary is denoted by n .

4.2.1 Poisson Equation

The Poisson equation with inhomogeneous boundary conditions in Cartesian coordinates can be expressed as

$$\nabla^2 V(\mathbf{x}) = \frac{\rho(\mathbf{x})}{\epsilon} \quad \text{for } \mathbf{x} \in \Omega \quad (4.1a)$$

$$V(\mathbf{x}) = V_0(\mathbf{x}) \quad \text{for } \mathbf{x} \in S_1 \quad (4.1b)$$

$$\frac{\partial V(\mathbf{x})}{\partial n} = g(\mathbf{x}) \quad \text{for } \mathbf{x} \in S_2 \quad (4.1c)$$

where $V(\mathbf{x})$ is the electric scalar potential, $\rho(\mathbf{x})$ is electric charge density, and ϵ material permittivity. Note \mathbf{x} represents the position vector in either two- or three-dimensions.

4.2.2 Diffusion Equation

The diffusion equation for eddy currents problem in Cartesian coordinates can be written as

$$\nabla \times \frac{1}{\mu} \nabla \times \bar{\mathbf{A}}(\mathbf{x}) + j\omega\sigma\bar{\mathbf{A}}(\mathbf{x}) + \sigma\nabla V(\mathbf{x}) = \bar{\mathbf{J}}_s(\mathbf{x}) \quad (4.2a)$$

where $\bar{\mathbf{A}}(\mathbf{x})$ is magnetic vector potential and $V(\mathbf{x})$ is electrical scalar potential, $\mu(\mathbf{x})$ and $\sigma(\mathbf{x})$ are permeability and conductivity, respectively, and $\bar{\mathbf{J}}_s(\mathbf{x})$ is the imposed current source. Equation (4.2a) together with the Coulomb gauge

$$\nabla \cdot \bar{\mathbf{A}}(\mathbf{x}) = 0 \quad (4.2b)$$

and associated boundary conditions are necessary to obtain the solution for $\bar{A}(\mathbf{x})$. Alternatively, (4.2) may be rewritten as

$$\nabla \times \frac{1}{\mu} \nabla \times \bar{A}(\mathbf{x}) + \nabla \left(\frac{1}{\mu} \nabla \cdot \bar{A}(\mathbf{x}) \right) + j\omega\sigma\bar{A}(\mathbf{x}) + \sigma\nabla V(\mathbf{x}) = \bar{J}_s(\mathbf{x}) \quad (4.3a)$$

$$\nabla \cdot (j\omega\sigma\bar{A}(\mathbf{x}) + \sigma\nabla V(\mathbf{x})) = 0 \quad (4.3b)$$

and it has been shown that the solution to these equations is unique [22]. To recover (4.2), one can take the divergence of (4.3a), and combining the resultant equation with (4.3b), we get

$$\nabla^2 \left(\frac{1}{\mu} \nabla \cdot \bar{A}(\mathbf{x}) \right) = 0 \quad (4.4)$$

with boundary condition

$$\frac{1}{\mu} \nabla \cdot \bar{A}(\mathbf{x}) = 0 \quad (4.5)$$

Our formulation is based on (4.3) instead of (4.2) since (i) the associated stiffness matrix in a finite element model is symmetric, and (ii) in general, it results in a well-conditioned set of equations [22].

4.3 Element-Free Galerkin Method

In the EFG method a set of nodes is used to construct the discrete equations. However, to implement the Galerkin procedure, it is necessary to compute the integrals over the solution domain, so either a regular background mesh or a background cell is used, but they are much simpler than the conventional FEM mesh. In numerical implementation, we'll give a detailed explanation.

Consider a function $u(\mathbf{x})$ that is to be approximated. The EFG method utilizes a moving least squares approach to do so, and relies on three components: (i) a weight function, (ii) a polynomial basis and (iii) a set of position dependent coefficients. The weight function is nonzero only over a small subdomain around a particular node, which is termed the domain of influence of that node.

4.3.1 Moving Least Square Approximation

In MLS approximation, the interpolant $u^h(\mathbf{x})$ is given by [31]

$$u^h(\mathbf{x}) = \sum_{j=0}^m p_j(\mathbf{x})a_j(\mathbf{x}) = \mathbf{p}^T(\mathbf{x})\mathbf{a}(\mathbf{x}) \quad (4.6)$$

where m is the number of terms in the basis, $p_j(\mathbf{x})$ are monomial basis functions, and $a_j(\mathbf{x})$ are coefficients that depend on the position \mathbf{x} . In two dimensions, $u^h(\mathbf{x})$ can be expressed in terms of either a linear or a quadratic basis as

$$\begin{aligned} u^h(x, y) &= a_0(x, y) + a_1(x, y)x + a_2(x, y)y && \text{(linear basis)} \\ u^h(x, y) &= a_0(x, y) + a_1(x, y)x + a_2(x, y)y + \\ &\quad a_3(x, y)x^2 + a_4(x, y)xy + a_5(x, y)y^2 && \text{(quadratic basis)} \end{aligned} \quad (4.7)$$

Lancaster and Salkauskas (1981) defined a local approximation by

$$u^h(\mathbf{x}, \bar{\mathbf{x}}) = \sum_{j=0}^m p_j(\bar{\mathbf{x}})a_j(\mathbf{x}) = \mathbf{p}^T(\bar{\mathbf{x}})\mathbf{a}(\mathbf{x}) \quad (4.8)$$

where \mathbf{x} is the approximation point, $\bar{\mathbf{x}}$ is a particular node. The coefficients $a_j(\mathbf{x})$ are determined by minimizing the difference between the local approximation and the nodal parameters u_j , i.e., minimize the following quadratic form,

$$\begin{aligned}
J &= \sum_{j=1}^n w(\mathbf{x} - \mathbf{x}_j) (u^h(\mathbf{x}, \mathbf{x}_j) - u_j)^2 \\
&= \sum_{j=1}^n w(\mathbf{x} - \mathbf{x}_j) \left[\sum_{i=0}^m p_i(\mathbf{x}_j) a_i(\mathbf{x}) - u_j \right]^2
\end{aligned} \tag{4.9}$$

Here $w(\mathbf{x} - \mathbf{x}_j)$ is a weight function with compact support, n is the number of nodes in the neighborhood of \mathbf{x} where the weight function doesn't vanish. In matrix notation, (4.9) can be written as

$$J = (\mathbf{P}\mathbf{a} - \mathbf{u})^T \mathbf{W}(\mathbf{x})(\mathbf{P}\mathbf{a} - \mathbf{u}) \tag{4.10}$$

where $\mathbf{u}^T = (u_1, u_2, \dots, u_n)$ are the unknowns,

$$\mathbf{P} = \begin{bmatrix} p_1(\mathbf{x}_1) & p_2(\mathbf{x}_1) & \cdots & p_m(\mathbf{x}_1) \\ p_1(\mathbf{x}_2) & p_2(\mathbf{x}_2) & \cdots & p_m(\mathbf{x}_2) \\ \vdots & \vdots & \ddots & \vdots \\ p_1(\mathbf{x}_n) & p_2(\mathbf{x}_n) & \cdots & p_m(\mathbf{x}_n) \end{bmatrix} \tag{4.11a}$$

and

$$\mathbf{W}(\mathbf{x}) = \begin{bmatrix} w(\mathbf{x} - \mathbf{x}_1) & & & 0 \\ & w(\mathbf{x} - \mathbf{x}_2) & & \\ & & \ddots & \\ 0 & & & w(\mathbf{x} - \mathbf{x}_n) \end{bmatrix} \tag{4.11b}$$

The minimization of J with respect to $\mathbf{a}(\mathbf{x})$ leads to

$$\mathbf{A}(\mathbf{x})\mathbf{a}(\mathbf{x}) - \mathbf{B}(\mathbf{x})\mathbf{u} = 0 \tag{4.12}$$

where

$$\mathbf{A} = \mathbf{P}^T \mathbf{W}(\mathbf{x}) \mathbf{P} \tag{4.13a}$$

$$\mathbf{B} = \mathbf{P}^T \mathbf{W}(\mathbf{x}) \tag{4.13b}$$

Therefore, we can write

$$\mathbf{a}(\mathbf{x}) = \mathbf{A}^{-1}(\mathbf{x})\mathbf{B}(\mathbf{x})\mathbf{u} \quad (4.14)$$

Substituting (4.14) into (4.8), and letting $\bar{\mathbf{x}} = \mathbf{x}$, the MLS approximation can be written as

$$u^h(\mathbf{x}) = \sum_{j=1}^n \Phi_j(\mathbf{x})u_j \quad (4.15)$$

where shape function Φ_j are given by

$$\Phi_j(\mathbf{x}) = \sum_{i=0}^m p_i(\mathbf{x})(\mathbf{A}^{-1}(\mathbf{x})\mathbf{B}(\mathbf{x}))_{ij} = \mathbf{p}^T \mathbf{A}^{-1} \mathbf{B}_j \quad (4.16)$$

The derivatives of shape function are

$$\begin{aligned} \Phi_{j,x} &= (\mathbf{p}^T \mathbf{A}^{-1} \mathbf{B}_j)_{,x} \\ &= \mathbf{p}_{,x}^T \mathbf{A}^{-1} \mathbf{B}_j + \mathbf{p}^T (\mathbf{A}^{-1})_{,x} \mathbf{B}_j + \mathbf{p}^T \mathbf{A}^{-1} \mathbf{B}_{j,x} \end{aligned} \quad (4.17a)$$

$$\begin{aligned} \Phi_{j,y} &= (\mathbf{p}^T \mathbf{A}^{-1} \mathbf{B}_j)_{,y} \\ &= \mathbf{p}_{,y}^T \mathbf{A}^{-1} \mathbf{B}_j + \mathbf{p}^T (\mathbf{A}^{-1})_{,y} \mathbf{B}_j + \mathbf{p}^T \mathbf{A}^{-1} \mathbf{B}_{j,y} \end{aligned} \quad (4.17b)$$

Here we shall note that the shape function does not satisfy the Kronecker delta criterion:

$\Phi_{j,y}(\mathbf{x}_k) \neq \delta_{jk}$, so $u^h(\mathbf{x}_j) \neq u_j$ which makes it difficult to impose essential boundary conditions. Techniques that can be applied to address this issue include using either a Lagrange multiplier or coupling with standard finite elements at the boundary. Also note that the shape function is constructed in same manner in both two- and three- dimensions.

4.3.2 Weight Function

In two dimensions, the solution domain is covered by domain of influence of each node; while the choice of shape of this domain is arbitrary, a circular or rectangular domain is typically used. In our implementation, a rectangular domain is used and its corresponding

weight function is referred to as a tensor product weight, which at any given point can be expressed as [31]

$$w(\mathbf{x} - \mathbf{x}_j) = w_x \cdot w_y = w(r_x) \cdot w(r_y) \quad (4.18)$$

where $w(r_i)$, for $i = x, y$, is either Gaussians, exponentials or cubic splines, and can be expressed as

$$w(r) = \begin{cases} 1 - e^{-(r-1)^2} & \text{for } r \leq 1 \\ 0 & \text{for } r > 1 \end{cases} \quad \text{(Gaussian)} \quad (4.19a)$$

$$w(r) = \begin{cases} e^{-(r/\alpha)^2} & \text{for } r \leq 1 \\ 0 & \text{for } r > 1 \end{cases} \quad \text{(Exponential)} \quad (4.19b)$$

$$w(r) = \begin{cases} \frac{2}{3} - 4r^2 + 4r^3 & \text{for } r \leq \frac{1}{2} \\ \frac{4}{3} - 4r + 4r^2 - \frac{4}{3}r^3 & \text{for } \frac{1}{2} < r \leq 1 \\ 0 & \text{for } r > 1 \end{cases} \quad \text{(Cubic spline)} \quad (4.19c)$$

where $\alpha = 0.5$ results best convergence for the exponential weight. and

$$r_x = \frac{|x - x_j|}{d_{mx}}, \quad r_y = \frac{|y - y_j|}{d_{my}} \quad (4.20)$$

$$d_{mx} = d_{\max} \cdot c_x, \quad d_{my} = d_{\max} \cdot c_y \quad (4.21)$$

d_{\max} is a scaling factor, (c_x, c_y) is the difference between node \mathbf{x}_j and its nearest neighbor.

Note, d_{mx} , d_{my} are chosen such that matrix \mathbf{A} is non-singular. In three- dimensions, the weight is a natural extension of those presented earlier for two-dimensions.

4.3.3 Discontinuities Approximation

NDE problems generally involve multiply connected regions where interfaces lie between different materials. This results in discontinuities of the normal component of

current density when passing from one material to another, which in turn implies that the derivatives of the shape function or the shape function itself should be discontinuous at the interface. Since continuity of shape function is inherited from continuity of weight function, it is necessary to introduce discontinuity into the weight function. This could be realized by using the visibility criterion [30].

As shown in Figure 4.1, if there is no material discontinuity, the domain of influence is the total area of the square. However, in the presence of a discontinuity, the domain of influence of node x_j shrinks to the area covered by dashed horizontal line, and the weight function will vanish outside of that area. This procedure directly results in the discontinuity of weight function, which in turn introduces the discontinuity of shape function and derivatives of shape function.

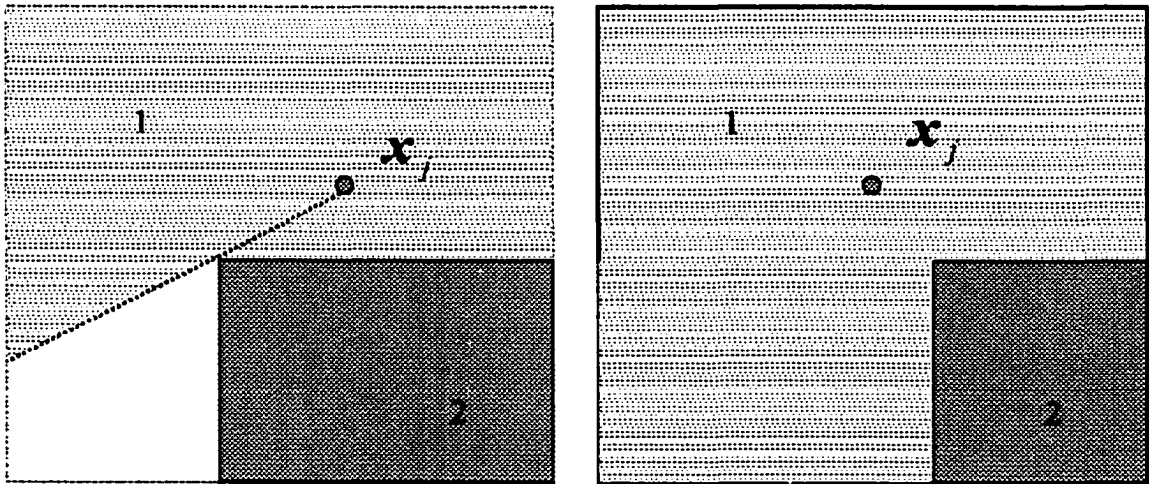


Figure 4.1 Domain of influence of node adjacent to material discontinuity.

4.4 Numerical Implementation

4.4.1 Static Problem

The weak form solution to the Poisson equation (4.1), V is computed by minimizing the functional $F(V)$, where

$$F(V) = \int_{\Omega} [(\nabla V)^2 - 2\frac{\rho}{\varepsilon}V]d\Omega + 2\int_{S_2} gVdS + \int_{S_1} \lambda(V - V_0)d\Omega \quad (4.22)$$

$V \in$ vector space W that satisfies the Dirichlet boundary conditions. Lagrange multipliers technique is applied to impose the boundary conditions, where λ is the Lagrange multiplier. In the numerical implementation, the vector space W usually is chosen to be a finite. Let the EFG shape functions $\{\Phi_i\}$ be the basis in W , then $V = \sum_{i=1}^N \Phi_i V_i$, where N is the total number of nodes in domain Ω . The functional $F(V)$ is minimized with respect to values of function V at all nodes in the domain Ω , that is, with respect to vector $V^T = (V_1, V_2, \dots, V_N)$.

The minimization of functional $F(V)$ results in the following equations,

$$\frac{\partial F}{\partial V} = \left[\frac{\partial F}{\partial V_1}, \frac{\partial F}{\partial V_2}, \dots, \frac{\partial F}{\partial V_N} \right]^T = 0 \quad (4.23)$$

which can be expressed as

$$\sum_{i=1}^N \left[\int_{\Omega} \nabla \Phi_i \cdot \nabla \Phi_j d\Omega \right] V_i + \sum_{k=1}^{N_{UK}} \left[\int_{S_1} N_k \Phi_j d\Omega \right] \lambda_k = - \int_{\Omega} \frac{\rho}{\varepsilon} \Phi_j d\Omega + \int_{S_2} g \Phi_j dS \quad (4.24a)$$

for $j = 1, 2, \dots, N$

Combining the above set of equations with Dirichlet boundary conditions

$$\sum_{i=1}^N \left[\int_{S_1} N_k \Phi_i dS \right] V_i - \int_{S_1} N_k V_0 dS = 0 \quad \text{for } k = 1, 2, \dots, N_{UK} \quad (4.24b)$$

we obtain a complete linear algebraic system. In the above equations, λ_k is Lagrange multiplier, N_k is the shape function associated with the Lagrange multiplier, and NUK is the number of nodes on S_1 where a Dirichlet boundary condition is imposed. As mentioned before, a background mesh is required for integration calculation appears in Eqns. (4.24) since evaluation of $d\Omega$ or dS corresponds to computation of the Jacobin of a background integration cell.

4.4.2 Quasi-Static Problem

Galerkin formulation and Lagrange multiplier technique will be applied to obtain the numerical solution to the eddy current equations (4.3). The first task is to express potentials as a linear combination of shape functions, such as $\bar{A} = \sum_{j=1}^{3N} \bar{\Phi}_j A_j$, and $V = \sum_{j=1}^N V_j \Phi_j$, where $\bar{\Phi}_j = \Phi_j \hat{x}$, $\Phi_j \hat{y}$ or $\Phi_j \hat{z}$. Next, substituting the above expressions into (4.3), performing the inner product on each of the resulting equations with a test function (shape function will be used), and apply Lagrange multiplier method, we obtain

$$\begin{aligned} \sum_{j=1}^{3N} [\int_{\Omega} (\frac{1}{\mu} \nabla \times \bar{\Phi}_i) \cdot (\nabla \times \bar{\Phi}_j) + \frac{1}{\mu} \nabla \cdot \bar{\Phi}_i \nabla \cdot \bar{\Phi}_j + j\omega \sigma \bar{\Phi}_i \cdot \bar{\Phi}_j d\Omega] A_j + \\ \sum_{j=1}^N [\int_{\Omega} \sigma \bar{\Phi}_i \cdot \nabla \Phi_j d\Omega] V_j + \sum_{k=1}^{3NUK} [\int_{\partial\Omega} \bar{\Phi}_i \cdot \bar{N}_k dS] \alpha_k = 0 \end{aligned} \quad (4.25a)$$

$$\begin{aligned} \sum_{j=1}^{3N} [\int_{\Omega} j\omega \sigma \nabla \Phi_i \cdot \bar{\Phi}_j d\Omega] A_j + \sum_{j=1}^N [\int_{\Omega} \sigma \nabla \Phi_i \cdot \nabla \Phi_j d\Omega] V_j + \\ \sum_{k=1}^{NUK} [\int_{\partial\Omega} \Phi_i N_k dS] \beta_k = 0 \end{aligned} \quad (4.25b)$$

$$\sum_{j=1}^{3N} [\int_{\partial\Omega} \bar{N}_k \cdot \bar{\Phi}_j dS] A_j - \int_S \bar{N}_k \cdot \bar{A}_0 dS = 0 \quad (4.25c)$$

$$\sum_{j=1}^N [\int_{\partial\Omega} N_k \Phi_j dS] V_j - \int_S N_k V_0 dS = 0 \quad (4.25d)$$

where A_j is one of three components of magnetic vector potential and V_j is electric scalar potential, α_k, β_k are Lagrange multipliers, N_k is the shape function associated with the Lagrange multipliers, NUK is the number of nodes where Dirichlet boundary is imposed. In matrix notation, (4.25) may be succinctly written as

$$GA = Q \quad (4.26)$$

As in the standard FEM methods, the matrix G is sparse, and (4.26) is solved using a standard non-stationary iterative solver such as (TF)QMR [28].

4.5 Applications and Results

In this section we present the validation of EFG method and compare their solutions to those obtained using traditional FEM. Finally the technique will be applied to two-dimensional quasi-static (eddy current NDE) problems.

4.5.1 Convergence Study and Comparison with Traditional FE

Consider the Poisson equation

$$\nabla^2 u(x, y) = 8\pi^2 \sin(2\pi x) \sin(2\pi y) \quad (x, y) \in [-0.5 \ 0.5] \times [-0.5 \ 0.5] \quad (4.27a)$$

with boundary condition

$$u(x, y) = 0 \quad (4.27b)$$

The analytical solution to this problem is

$$u(x, y) = \sin(2\pi x) \sin(2\pi y) \quad (4.27c)$$

(a) Effect of mesh density: Uniform meshes of $9 \times 9, 17 \times 17, 33 \times 33, 65 \times 65$ nodes are used with 4×4 Gaussian quadrature in each cell. EFG with linear and quadratic bases are used in the study, results are compared with those obtained by linear FEM. A typical surface plot of a numerical solution is shown in Figure 4.2. The error estimations in L^2 and H^1 norm are shown in Figure 4.3 and Figure 4.4. The error functions and convergence rate r are computed as

$$L^2 err(h) = \left(\int_{\Omega} (u^{num} - u^{exact})^2 d\Omega \right)^{\frac{1}{2}} \quad (4.28a)$$

$$H^1 err(h) = \left(\int_{\Omega} (u^{num} - u^{exact})^2 + \sum_{\alpha=x,y} (u_{\alpha}^{num} - u_{\alpha}^{exact})^2 d\Omega \right)^{\frac{1}{2}} \quad (4.28b)$$

$$r = \log_2(err(h) / err(2h)) \quad (4.28c)$$

It can be observed that the convergence rate of EFG depends on the scaling factor. The convergence rate of EFG method is higher than that of linear FEM in both L^2 and H^1 norm, which varies from 2.1 to 3.1 in L^2 norm, and varies from 1.0 to 2.0 in H^1 norm. We should mention that the EFG method is inherently a high order scheme that requires more computation overhead than linear FEM that is used for comparison.

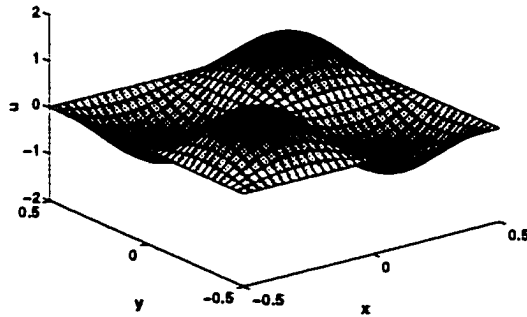
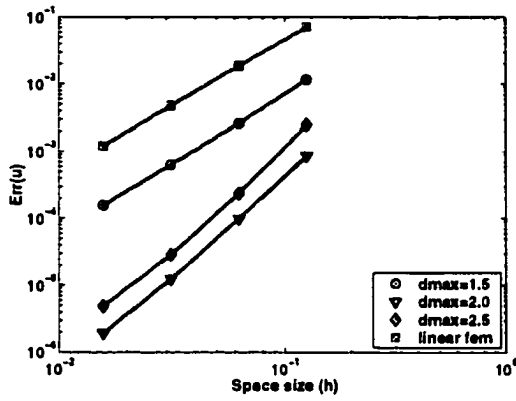
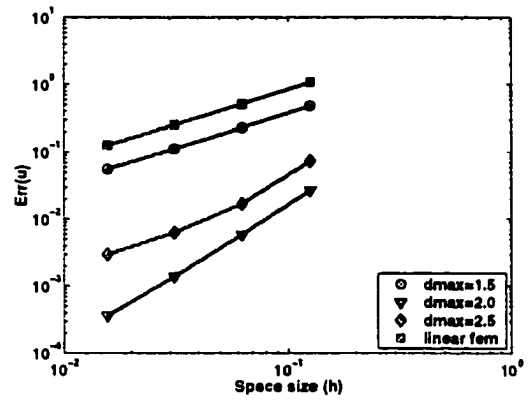


Figure 4.2 Surface plot of numerical solution.

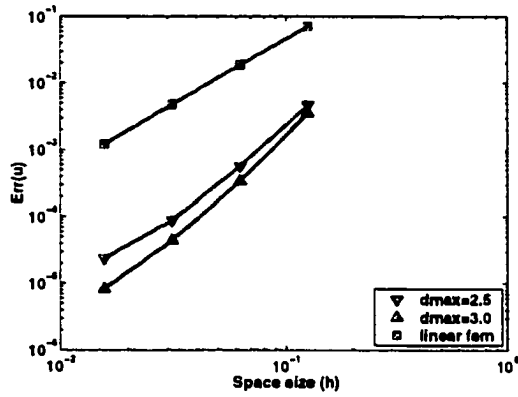


(a)

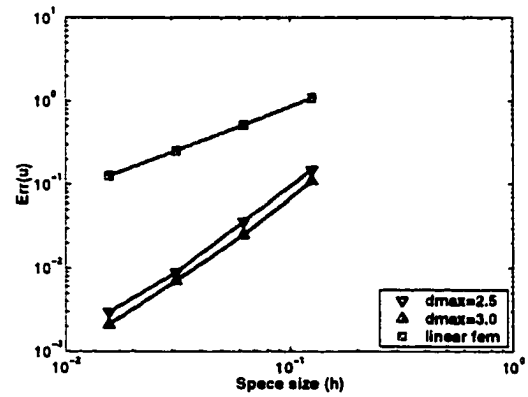


(b)

Figure 4.3 (a) Error estimation in L^2 norm for the linear EFG. (b) Error estimation in H^1 norm for the linear EFG.



(a)



(b)

Figure 4.4 (a) Error estimation in L^2 norm for the quadratic EFG. (b) Error estimation in H^1 norm for the quadratic EFG.

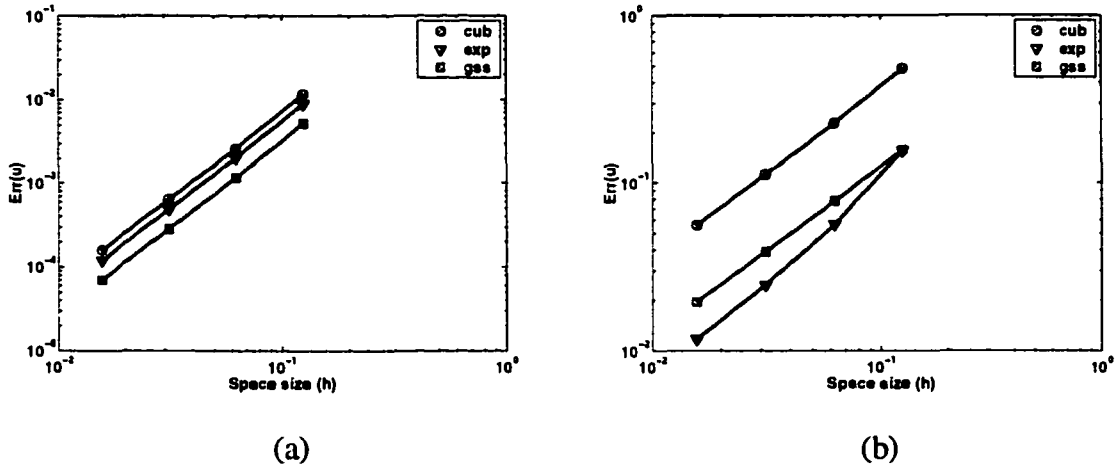


Figure 4.5 (a) Error estimation in L^2 norm for different weight functions. (b) Error estimation in H^1 norm for different weight functions.

(b) Effect of weight function: As mentioned before, weight function is crucial to the convergence of numerical solution. Cubic splines, exponentials, and Gaussians are some of the commonly used weight functions. It is found that cubic spline has the best convergence property, while the exponential and Gaussian are better when the scaling factor is small. This is largely due to the fact that the latter two functions reduce the domain of influence, which in turn reduces the number of non-zero entries in the stiffness matrix. This reduction saves both computational time and memory.

4.5.2 Application to Eddy Current NDT

(a) Validation geometry – a disk: Now we consider a two-dimensional eddy current problem. The governing equation in $A-V$ formulation is derived from Maxwell equations [22],

$$\nabla \times \frac{1}{\mu} \nabla \times \bar{A}(x,y) + j\omega\sigma\bar{A}(x,y) + \sigma\nabla V(x,y) = \bar{J}_s(x,y) \quad (4.29a)$$

in a unit disk $r \leq 1$, with Dirichlet boundary conditions

$$\bar{A}(x,y) = \begin{pmatrix} -y \\ x \end{pmatrix}, V(x,y) = 0 \quad (4.29b)$$

on a unit circle $r = 1$, where $r = (x^2 + y^2)^{\frac{1}{2}}$. The analytical solution for this problem is

$$\bar{A}(x,y) = \frac{I_1(j^{\frac{1}{2}}(\omega\sigma\mu)^{\frac{1}{2}}r)}{rI_1(j^{\frac{1}{2}}(\omega\sigma\mu)^{\frac{1}{2}})} \begin{pmatrix} -y \\ x \end{pmatrix}, V(x,y) = 0 \quad (4.32)$$

where $I_1(x)$ is the first kind of modified Bessel function. The numerical solution is shown in Figure 4.5c where $\omega = 1, \sigma = 1, \mu = 1$. The domain was uniformly discretized using a 6×6 grid of nodes (Figure 4.6a), 4×4 cells for integration, and 4×4 Gaussian quadrature in each quadrature cell as shown in Figure 4.6b. The circular flow of eddy currents demonstrates that the model predictions are validated. To study the convergence behavior of this method, several discretizations namely, 9×9 , 17×17 , 33×33 , 65×65 nodal points were tried. EFG with linear bases was used in this study, and the results obtained were compared against those using linear FEM for the same discretizations. The error estimations in both L^2 and H^1 norm are shown in Figure 4.7a and Figure 4.7b.

The convergence rate (defined in (4.28)) of EFG method is 2.39 in L^2 norm, higher than linear FEM, whose convergence rate is 2.0. The convergence rate of EFG method is 1.35 in H^1 norm, also higher than that of linear FEM.

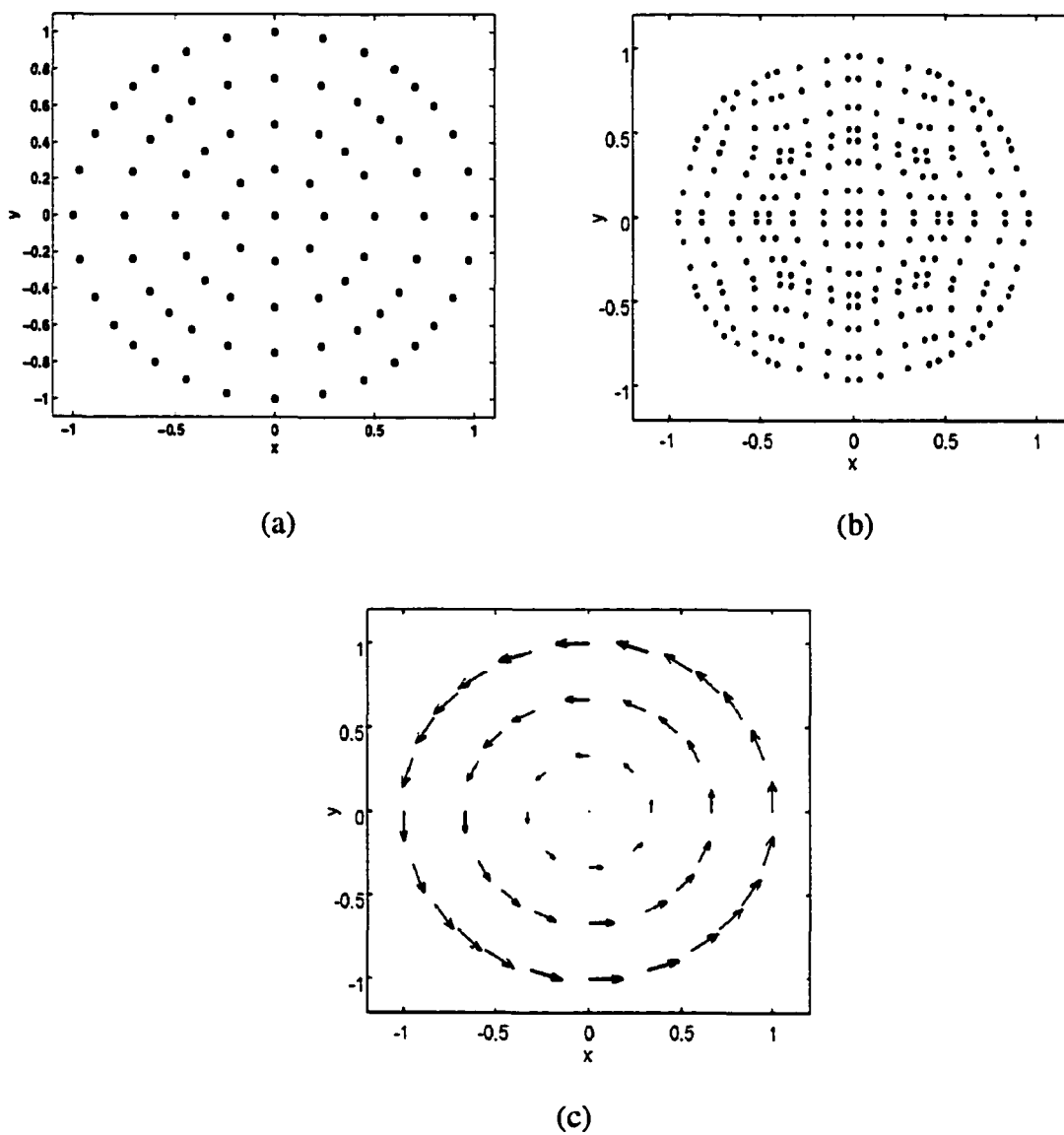


Figure 4.6 Eddy current in unit disk.

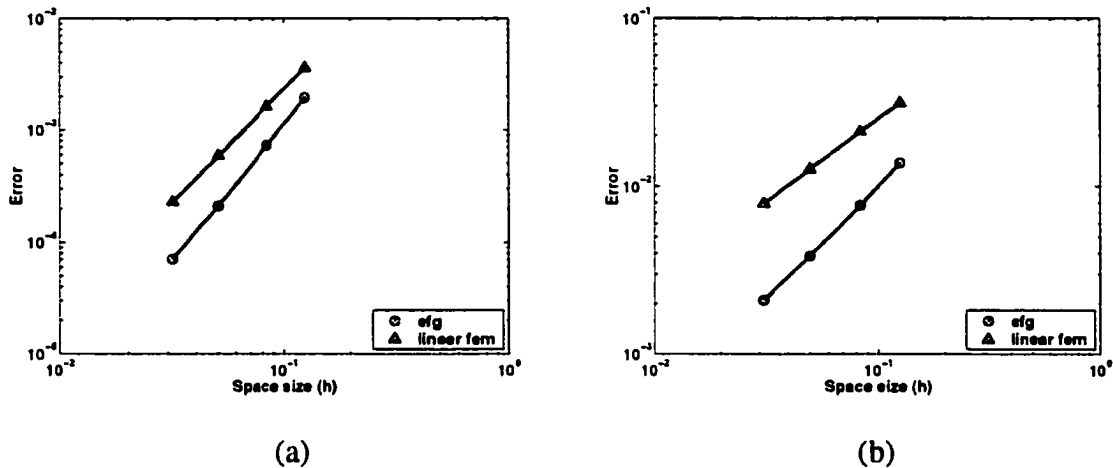


Figure 4.7 (a) Error estimation in L^2 norm. (b) Error estimation in H^1 norm.

(b) Experimental geometry – plate with tight crack: Assume an infinite-size conducting plate with a tiny crack along y direction ($width = 0$, $length = 1$) is placed under a time-varying harmonic current source in the x direction. The induced current will be along $-x$ direction in the absence of crack, and will be perturbed by its presence. This geometry was modeled using the EFG method and results of induced current distribution are shown in Figure 4.9a. As shown in Figure 4.8, A tight crack is modeled without introducing any additional nodes (total 144 nodes) in the region in contrast to conventional FEM, which requires a larger number of nodes (total 180 nodes) and elements since at least two layers of elements is needed to model the crack. Figure 4.9b shows the difference of eddy current distribution, it shows that the two solutions are very close to each other. The induced current flows around the crack due to the electrical discontinuity. This again confirms the reliability of EFG methods to model cracks.

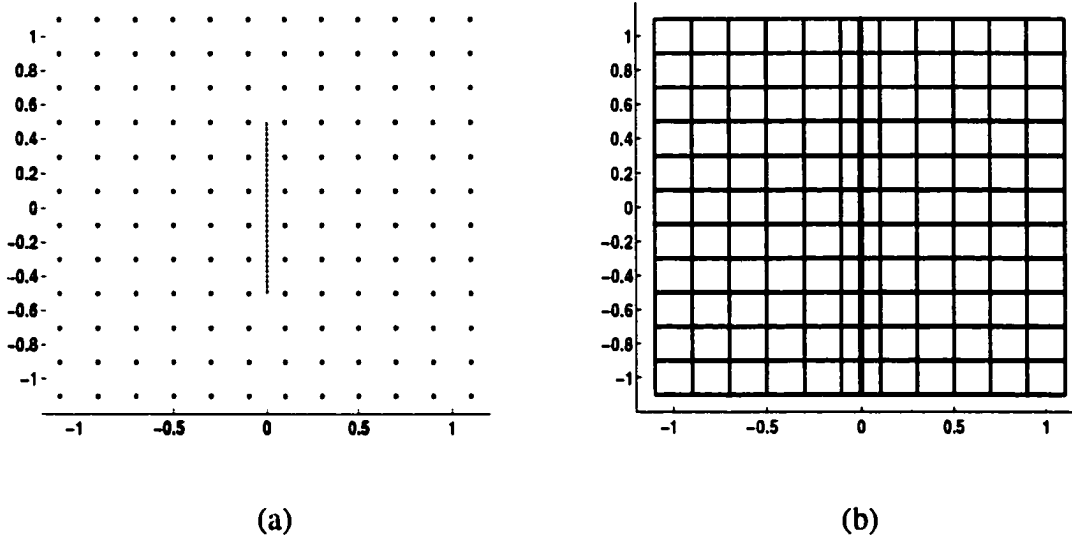


Figure 4.8 Discretization of solution region with a tight crack. (a) EFG (b) FEM

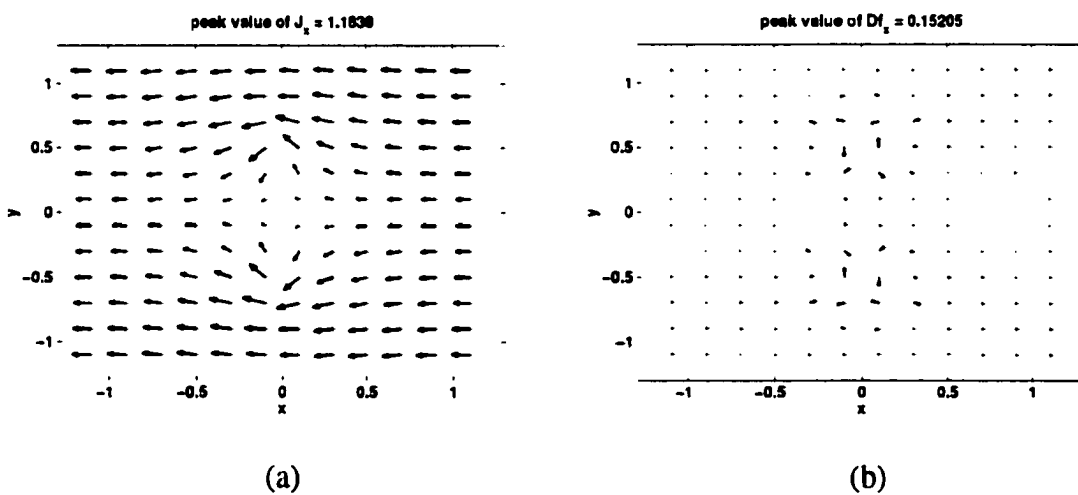
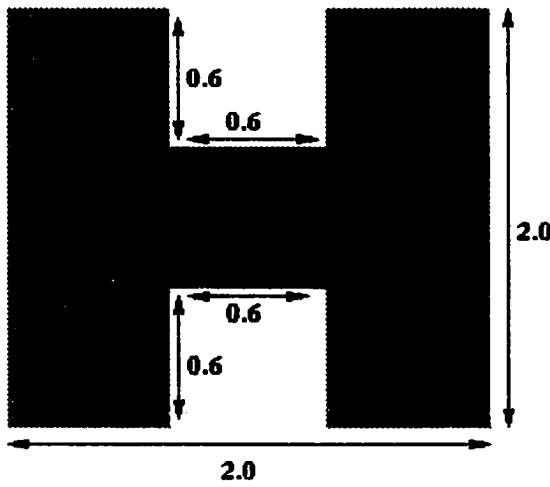


Figure 4.9 (a) Eddy current in presence of crack predicted by EFG. (b) Difference between EFG and FEM.

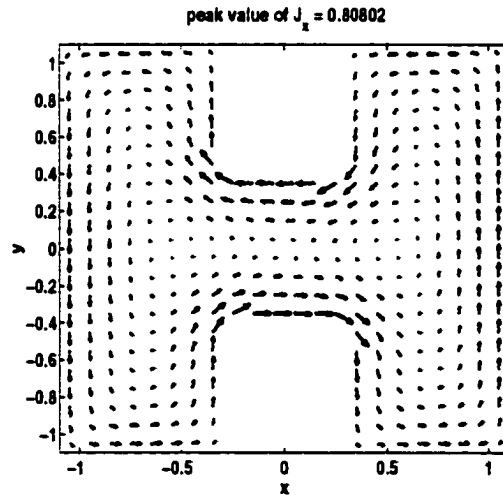
(c) **Conducting plate in time-varying field:** The third geometry considered for the purpose of model validation is a conducting plate, which is immersed in a time-varying harmonic magnetic field as shown in Figure 4.10a. Using $B = 1, \omega = 1, \sigma = 1, \mu = 1$, the induced eddy currents is calculated with both EFG and FE methods as shown in Figure 4.10b and Figure 4.10c. Both methods correctly predict the current continuity conditions and the eddy current flow around the sharp corners in the geometry.

Both models use a discretization of 23×23 nodes uniformly distributed in region $[-1.15 \ 1.15] \times [-1.15 \ 1.15]$. The relative total energy difference (R) between them is 6.82% which is mainly occurs at the corners.

$$R = \frac{\left(\int_{\Omega} (J_x^{EFG} - J_x^{FEM})^2 + (J_y^{EFG} - J_y^{FEM})^2 d\Omega \right)^{\frac{1}{2}}}{\left(\int_{\Omega} (J_x^{FEM})^2 + (J_y^{FEM})^2 d\Omega \right)^{\frac{1}{2}}} \quad (4.35)$$



(a)



(b)

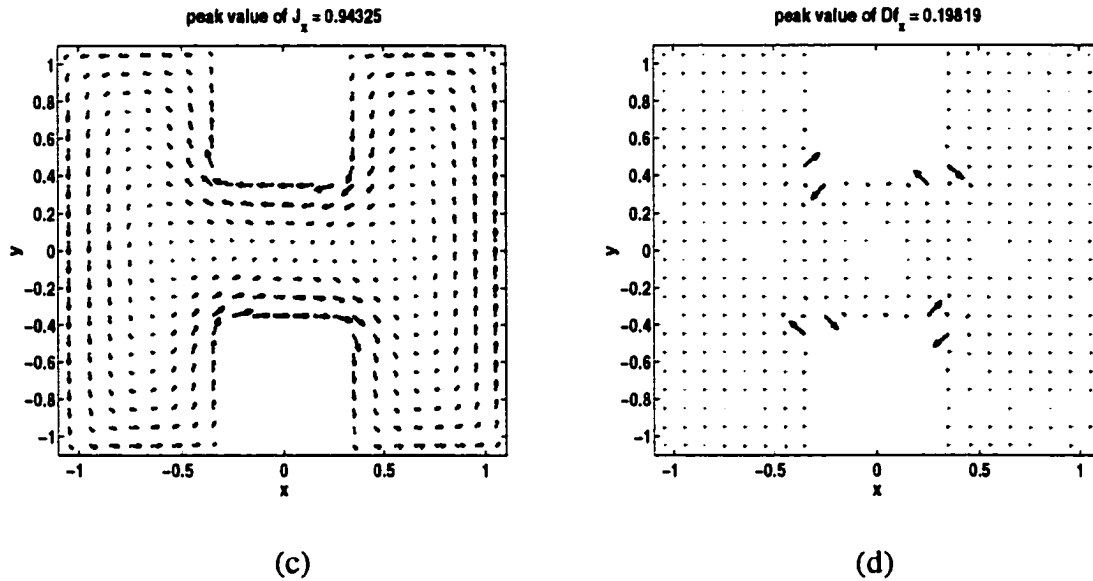


Figure 4.10 (a) Geometry of an 'H' plate. (b) Numerical induced currents inside the plate calculated by EFG. (c) Numerical induced currents inside the plate calculated by FEM. (d) Difference between FEM and EFG.

So far, through these examples, we see that EFG method can be successfully applied to the NDE problems in either static or quasi-static fields. Compared with usual FE Methods, EFG methods can obtain the same accuracy with less computation time and fewer data storage. Furthermore, EFG methods avoid the difficulties of large mesh changes in problems involving tight cracks. In the next, we will continue to exploit the EFG methods in multi-frequency and time-dependent problems.

CHAPTER 5. MULTIFREQUENCY AND PULSED EDDY CURRENT TECHNIQUES

5.1 Introduction

Non-destructive testing (NDT) technology that is based either on sinusoidal or on pulsed eddy current techniques is widely used in both aviation and nuclear industries for the detection of surface and subsurface defects and corrosion. The depth of penetration of the field depends on the conductivity of the sample and the operating frequency. At very low frequencies, the depth is large, while at high frequencies the depth is localized to the surface. For a given conductivity, one can detect cracks at a range of depths, for instance, detecting cracks in a multi-layered structure, by using a suitable mix of frequencies. In practice this is done using multifrequency or pulsed eddy current technique. The multifrequency technique is extensively used in nuclear utilities for extracting defect signals that are masked by unwanted signals from artifacts such as support plates. In the pulsed eddy current method, the signal's amplitude and time-to-zero-crossing (TZC) are two most essential features for defect characterization. The peak value is related to the size of defect and the depth location of defect, while TZC is mainly related to the defect depth [2]. The principle advantage of pulsed eddy current methods is that these time domain methods can yield information at a variety of frequency points that lie within the bandwidth of the pulse used [35]. This technology is extremely useful in analyzing multi-layered structures that are often encountered in the aerospace industry.

The analytic approach to eddy currents problems can be traced back to more than 40 years ago; the theory for the response of a coil over a layered conducting structure for a single frequency was developed by Cheng, Dodd and Deeds [36]. By applying Laplace-transform technique, Ludwig, Bowler and others have developed theoretical solutions for modeling of pulsed eddy currents in conducting half-space [35]-[37]. In the mean time, eddy currents techniques were widely applied to the detection of corrosion and cracks in multi-layered aircraft structures in the Center for Nondestructive Evaluation at Iowa State University [38] [39]. In the next section, we will present several two-dimensional EFG models for multifrequency eddy current and pulsed eddy current testing.

5.2 Multifrequency Eddy Currents

Here we consider a two dimensional eddy current problem. The governing equation in $A - V$ formulation, in frequency domain is given by

$$\nabla \times \frac{1}{\mu} \nabla \times \bar{A}(x, y) + j\omega\sigma[\bar{A}(x, y) + \nabla V(x, y)] = 0 \quad (5.1a)$$

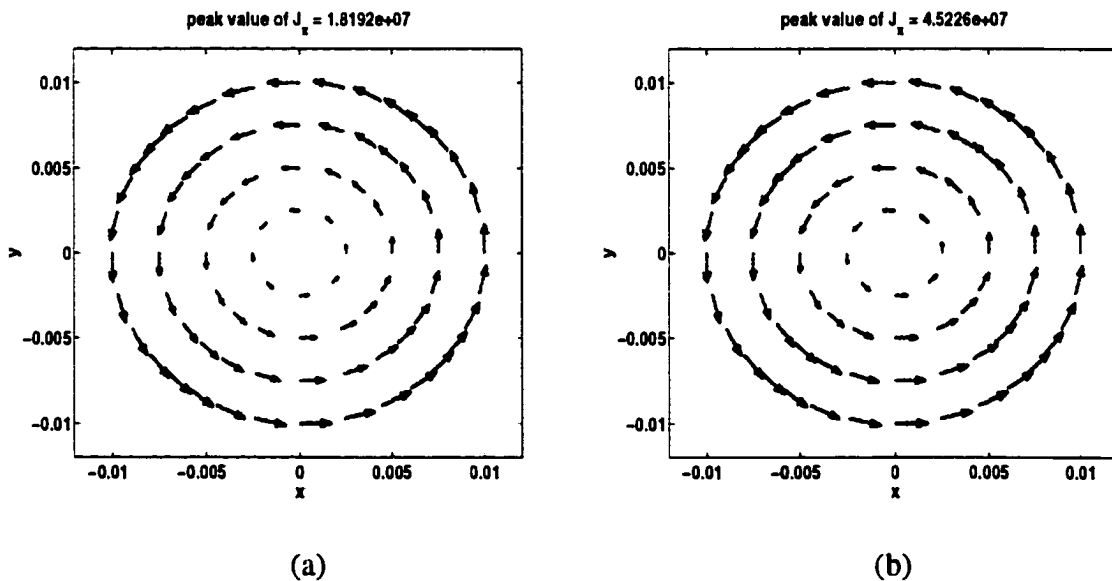
in a disk $r \leq 0.01$, with Dirichlet boundary conditions

$$\bar{A}(x, y) = \begin{pmatrix} y \\ -x \end{pmatrix}, V(x, y) = 0 \quad (5.1b)$$

on $r = r_0 (= 0.01)$, where $r = (x^2 + y^2)^{\frac{1}{2}}$. The analytical solution for this problem is given by

$$\bar{A}(x, y) = \frac{r I_1(j^{\frac{1}{2}}(\omega\sigma\mu)^{\frac{1}{2}}r)}{r_0 I_1(j^{\frac{1}{2}}(\omega\sigma\mu)^{\frac{1}{2}}r_0)} \begin{pmatrix} y \\ -x \end{pmatrix}, V(x, y) = 0 \quad (5.2)$$

where $I_1(x)$ is the modified Bessel function of the first kind. We choose the conductivity $\sigma = 1.8867 \times 10^7 \text{ S/m}$, permeability $\mu = 4\pi \times 10^{-7} \text{ H/m}$, and the frequency varies from 10 Hz to 10 KHz . In EFG formulation, as the frequency increases, the matrix system becomes more ill conditioned, since the entries correspond to Lagrange multipliers do not change while all other entries increase with the frequency. By amplifying these unchanged entries with the frequency, the matrix system becomes well conditioned. Figure 5.1 shows the eddy currents inside the disk for various frequencies. Figure 5.2 demonstrates that the accuracy of EFG is affected by the excitation frequency, that is, both relative errors in L^2 norm and H^1 norm increase with the frequency. But the numerical error is proportional to the spacing size, so it is controllable. Here spacing size is defined as the largest distance between two neighbor nodes.



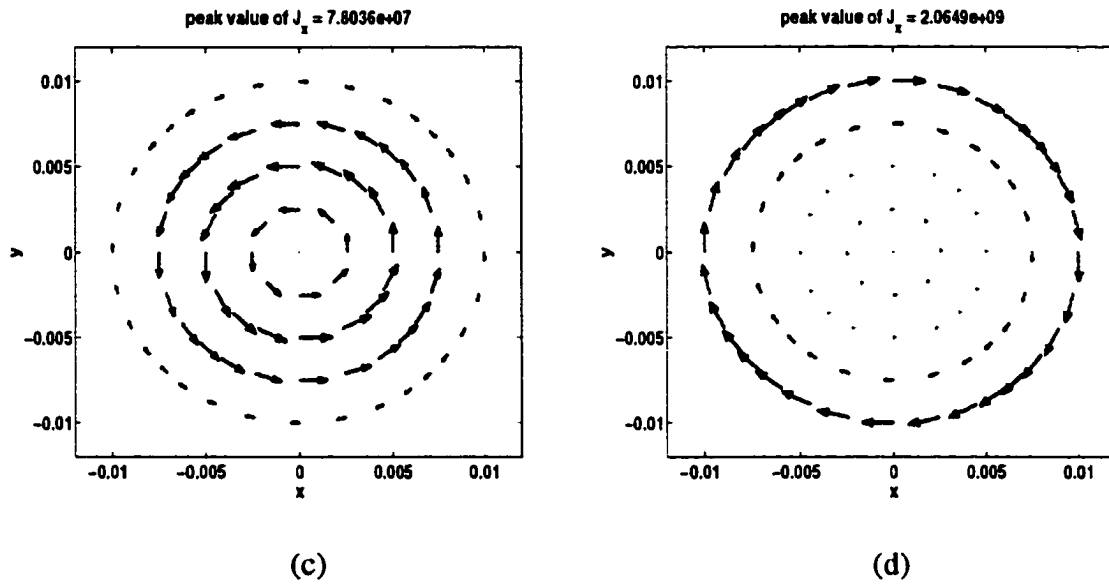


Figure 5.1 Eddy currents in a disk with the excitation frequency of (a) 300 Hz (b) 1 KHz (c) 3 KHz (d) 10 KHz. The length of arrow is proportional to amplitude of current density.

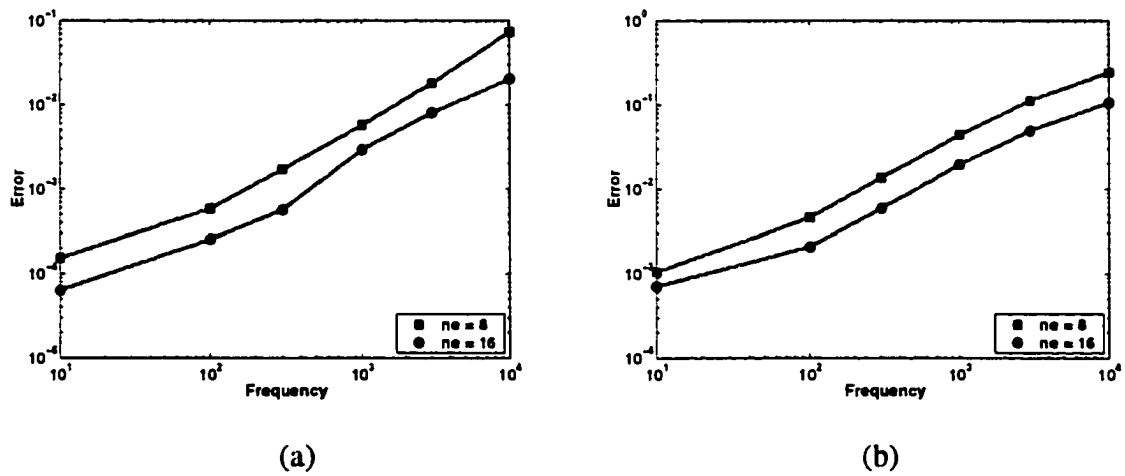


Figure 5.2 Relative error versus excitation frequency. (a) in L^2 norm (b) in H^1 norm

5.3 Pulsed Eddy Currents

The governing equations for the transient eddy current problem can be written in terms of the magnetic vector potential \bar{a} and the electric scalar potential v as

$$\nabla \times \frac{1}{\mu} \nabla \times \bar{a}(x, y) + \nabla \left[\frac{1}{\mu} \nabla \cdot \bar{a}(x, y) \right] + \frac{\partial}{\partial t} [\sigma \bar{a}(x, y) + \sigma \nabla v(x, y)] = \bar{j}_s(x, y) \quad (5.5.a)$$

$$\nabla \cdot \left[\frac{\partial}{\partial t} (\sigma \bar{a}(x, y) + \sigma \nabla v(x, y)) \right] = 0 \quad (5.5b)$$

Here an implicit Coulomb gauge is applied, which results in a high degree of numerical stability.

5.3.1 Time Domain Solution

Using Galerkin formulation and Lagrange multiplier technique to (5.5) with EFG shape functions, we obtain

$$\begin{aligned} \sum_{j=1}^{2N} \left[\int_{\Omega} \left(\frac{1}{\mu} \nabla \times \bar{\Phi}_i \right) \cdot (\nabla \times \bar{\Phi}_j) + \frac{1}{\mu} \nabla \cdot \bar{\Phi}_i \nabla \cdot \bar{\Phi}_j d\Omega \right] a_j + \sum_{j=1}^{2N} \left[\int_{\Omega} \sigma \bar{\Phi}_i \cdot \bar{\Phi}_j d\Omega \right] \frac{da_j}{dt} + \\ \sum_{j=1}^N \left[\int_{\Omega} \sigma \bar{\Phi}_i \cdot \nabla \Phi_j d\Omega \right] \frac{dv_j}{dt} + \sum_{k=1}^{2NUK} \left[\int_{\partial\Omega} \bar{\Phi}_i \cdot \bar{N}_k dS \right] \frac{d\alpha_k}{dt} = \sum_{j=1}^N \int_{\Omega} \bar{\Phi}_i \cdot \bar{j}_s d\Omega \end{aligned} \quad (5.6.a)$$

$$\begin{aligned} \sum_{j=1}^{2N} \left[\int_{\Omega} \sigma \nabla \Phi_i \cdot \bar{\Phi}_j d\Omega \right] \frac{da_j}{dt} + \sum_{j=1}^N \left[\int_{\Omega} \sigma \nabla \Phi_i \cdot \nabla \Phi_j d\Omega \right] \frac{dv_j}{dt} + \\ \sum_{k=1}^{2NUK} \left[\int_{\partial\Omega} \Phi_i N_k dS \right] \frac{d\beta_k}{dt} = 0 \end{aligned} \quad (5.6.b)$$

$$\sum_{j=1}^{2N} \left[\int_{\partial\Omega} \bar{N}_k \cdot \bar{\Phi}_j dS \right] \frac{da_j}{dt} - \int_s \bar{N}_k \cdot \frac{d\bar{a}_0}{dt} dS = 0 \quad (5.6.c)$$

$$\sum_{j=1}^N \left[\int_{\partial\Omega} N_k \Phi_j dS \right] \frac{dv_j}{dt} - \int_s N_k \frac{dv_0}{dt} dS = 0 \quad (5.6.d)$$

In matrix notation, this can be written as

$$G_1 A + G_2 \frac{dA}{dt} = Q \quad (5.7)$$

which is a system of ordinary differential equations.

The vector $A = [a_1, a_2, v_1, \dots, a_{2k-1}, a_{2k}, v_k, \dots]^T$ represents the unknown nodal values of the potential \bar{a} and v . G_1 , G_2 and Q are obtained by integration of the EFG shape functions. Equation (5.7) is solved by time stepping: the unknowns are solved at the time instances $t = n\Delta t$, ($n = 1, 2, \dots$), Δt is the time step. Using implicit Euler's time stepping procedure, we get an algebraic equation

$$(G_1 + \frac{1}{\Delta t} G_2) A^{n+1} = \frac{1}{\Delta t} G_2 A^n + Q^n \quad (5.8)$$

where A^n denotes the value of A at $t = n\Delta t$. The required initial condition A^0 is obtained by neglecting G_2 in Equation (5.8) and solving the remaining static equation. Note that implicit Euler scheme is always stable, so we can choose $\Delta t = 1.0 \mu s$ which ensures the accuracy.

Consider the geometry shown in Figure 5.3 that consists of a current source (an infinite wire) located 1.5 mm above the conducting plate with current density of 25 A/m^2 , and a rectangular plate of length 1.44 mm and width 1 mm . The objective is to compute the eddy currents that are induced on the plate. In this case, both the magnetic potential and current degrade to be scalars. Figures 5.4 and 5.5 show values of potential and induced current at different times. The induction field spreads out and the peak value decreases with time as expected. The solution region is chosen as $[-20 \ 20] \times [-10 \ 20] \text{ mm}^2$, which is large enough such that the field has decayed substantially.

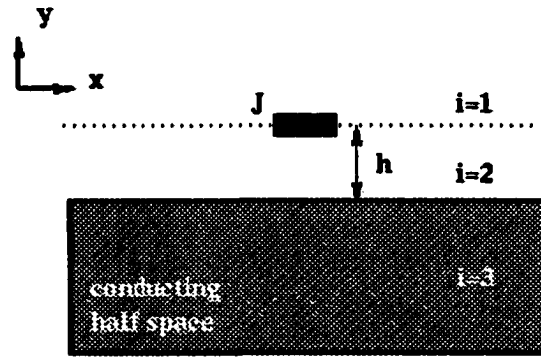


Figure 5.3 Geometry of current source and conducting half-space.

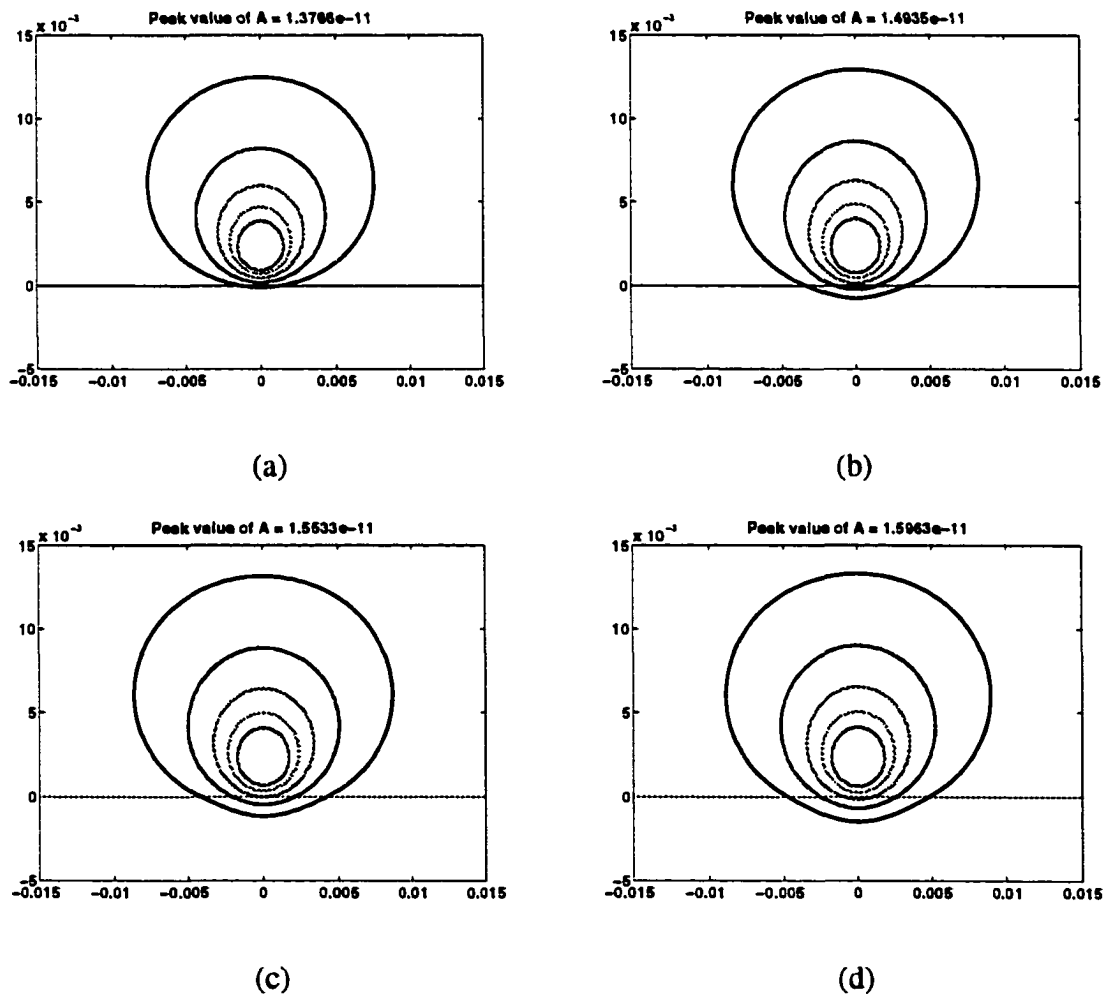
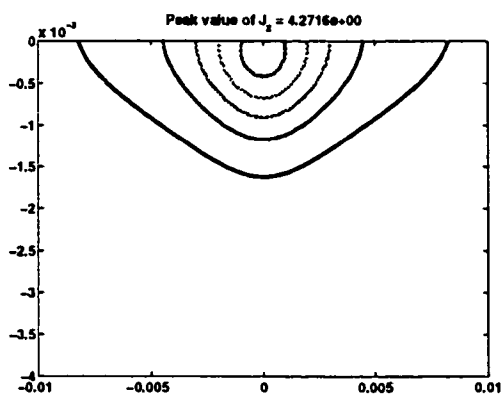
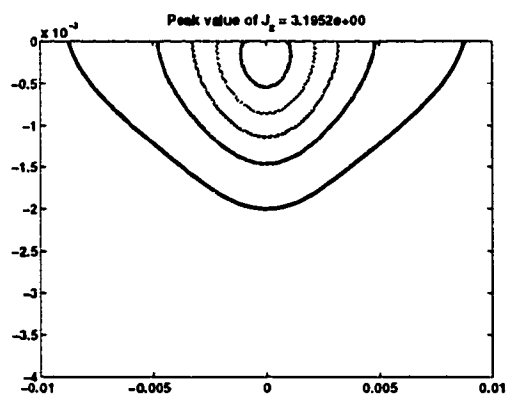


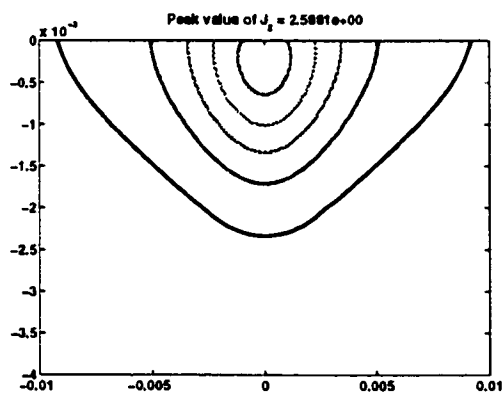
Figure 5.4 Magnetic potential at various time instances. (a) $t = 5 \mu s$ (b) $t = 30 \mu s$ (c) $t = 55 \mu s$ (d) $t = 80 \mu s$



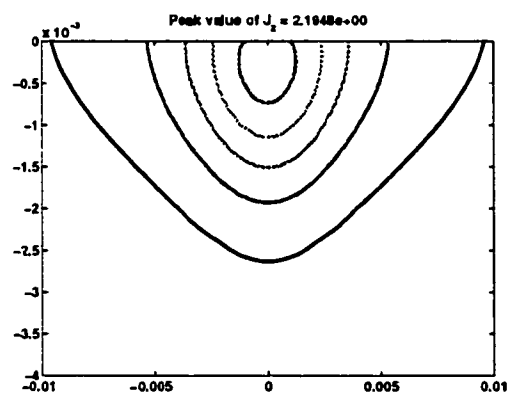
(a)



(b)



(c)



(d)

Figure 5.5 Induced current at various time instances. (a) $t = 12 \mu s$ (b) $t = 18 \mu s$ (c) $t = 24 \mu s$ (d) $t = 30 \mu s$

5.3.2 Analytic Solution in Frequency Domain

Alternatively, this problem can be solved analytically. Noting that the magnetic potential is a scalar, and the electrical potential is unnecessary, the governing equation is simplified as

$$-\frac{1}{\mu} \nabla^2 a(x, y) + \sigma \frac{\partial}{\partial t} a(x, y) = j_s(x, y) \quad (5.9)$$

where $a(x, y)$, $j_s(x, y)$ denote the magnetic potential and source current in time domain.

For a time harmonic varying field, the governing equation in frequency domain can be written as

$$-\frac{1}{\mu} \nabla^2 A(x, y) + j\omega\sigma A(x, y) = J_s(x, y) \quad (5.10)$$

where $A(x, y)$, $J_s(x, y)$ are the corresponding quantities in frequency domain.

Now supposing $J_s = \delta(x)\delta(y-h)$, the solution can be derived by separation of variables technique. Assume $A(x, y) = f(x)g(y)$, then

$$-\frac{1}{\mu} (gf_{xx} + fg_{yy}) + j\omega\sigma fg = \delta(x)\delta(y-h) = 0 \quad \text{at } (x, y) \neq (0, h) \quad (5.11)$$

So $\frac{f_{xx}}{f} + \frac{g_{yy}}{g} = j\omega\sigma\mu$, which is equivalent to

$$f_{xx} + k^2 f = 0 \quad (5.12 a)$$

$$g_{yy} - (k^2 + j\omega\sigma\mu)g = 0 \quad (5.12b)$$

Due to geometric symmetry in x direction, (5.12a) has only solution in terms of $\cos(kx)$.

(5.12b) has solution in terms of $e^{-\gamma y}$ or $e^{\gamma y}$, where $\gamma^2 = k^2 + j\omega\sigma\mu$.

Based on superposition of these basic solutions, and applying zero boundary condition in the far field, the vector potential can be written as

$$A_1(x, y) = \int_0^{\infty} C_1(k) \cos(kx) e^{-k(y-h)} dk \quad (5.13a)$$

$$A_2(x, y) = \int_0^{\infty} [C_2(k) e^{k(y-h)} + D_2(k) e^{-ky}] \cos(kx) dk \quad (5.13b)$$

$$A_3(x, y) = \int_0^{\infty} C_3(k) \cos(kx) e^{ky} dk \quad (5.13c)$$

A_i denotes the vector potential in the i th region as shown in Figure 5.3. This solution is called Green function of (5.10). The interface conditions in terms of the normal and tangential components of the electrical field and magnetic field can be expressed in terms of potentials as follows

$$A_i = A_{i+1} \quad (5.14a)$$

$$\int_{0^-}^{0^+} \int_{h^-}^{h^+} -\frac{1}{\mu} (A_{xx}^- + A_{yy}^-) - j\omega\sigma A dx dy = 1 \quad (5.14b)$$

$$\int_{0^-}^{0^+} \int_{0^-}^{0^+} -\frac{1}{\mu} (A_{xx}^- + A_{yy}^-) - j\omega\sigma A dx dy = 0 \quad (5.14c)$$

Since A is finite and x symmetric, (5.14b) is same as

$$1 = \int_{0^-}^{0^+} \int_{h^-}^{h^+} -\frac{1}{\mu} A_{yy}^- dx dy = \int_{0^-}^{0^+} -\frac{1}{\mu} \left(\frac{\partial A(x, h^+)}{\partial y} - \frac{\partial A(x, h^-)}{\partial y} \right) dx$$

So

$$-\frac{1}{\mu} \left(\frac{\partial A(0, h^+)}{\partial y} - \frac{\partial A(0, h^-)}{\partial y} \right) = \delta(x) \quad (5.14b')$$

Similarly we have

$$-\frac{1}{\mu} \left(\frac{\partial A(0, 0^+)}{\partial y} - \frac{\partial A(0, 0^-)}{\partial y} \right) = 0 \quad (5.14c')$$

Applying the interface conditions, we get

$$C_1 = C_2 + D_2 e^{-kh} \quad (5.15a)$$

$$C_2 e^{-kh} + D_2 = C_3 \quad (5.15b)$$

$$\int_0^{\infty} \frac{k}{\mu} (C_1 + C_2 - D_2 e^{-kh}) \cos(kx) dx = \delta(x) \quad (5.15c)$$

$$C_2 e^{-kh} k - D_2 k = C_3 \gamma \quad (5.15d)$$

Note that

$$\int_0^{\infty} \cos(kx) dk = \frac{1}{2} \int_{-\infty}^{\infty} \cos(kx) dk = \frac{1}{4} \int_{-\infty}^{\infty} (e^{jkx} + e^{-jkx}) dk = \frac{\pi}{2} (\delta(x) + \delta(-x)) = \pi \delta(x)$$

So (5.15c) can be replaced by

$$\frac{k}{\mu} (C_1 + C_2 - D_2 e^{-kh}) = \frac{1}{\pi} \quad (5.15c')$$

Finally, the coefficients is given by

$$C_1(k) = \frac{\mu}{2\pi k} \left(1 + \frac{k-\gamma}{k+\gamma} e^{-2kh}\right) \quad (5.16a)$$

$$C_2(k) = \frac{\mu}{2\pi k} \quad (5.16b)$$

$$D_2(k) = \frac{\mu}{2\pi k} \frac{k-\gamma}{k+\gamma} e^{-kh} \quad (5.16c)$$

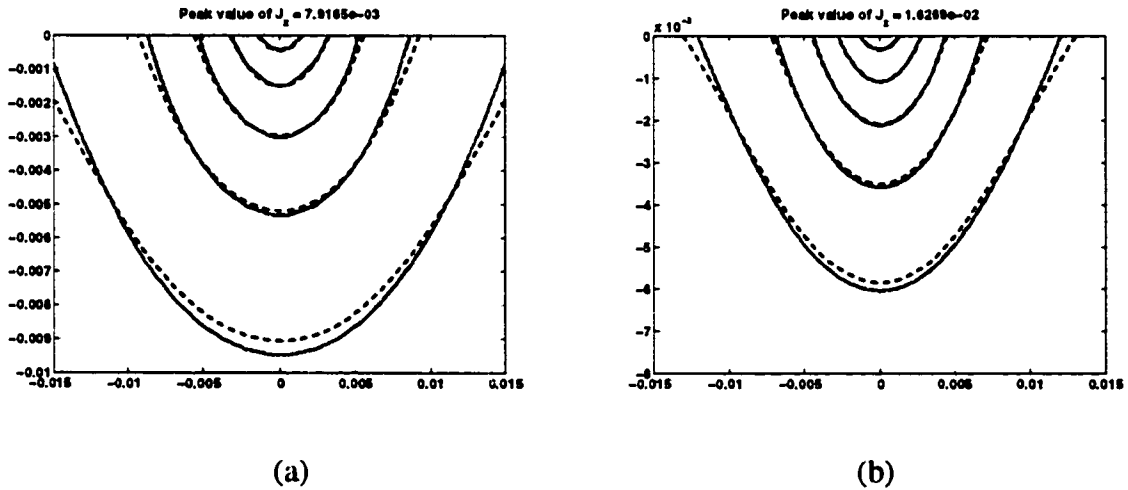
$$C_3(k) = \frac{1}{\pi} \frac{\mu}{k+\gamma} e^{-kh} \quad (5.16d)$$

The solution of (5.10) should be the convolution of its Green function and source current excitation. Assume the source is uniformly distributed in a region $[-\tau \tau] \times [h - \Delta \ h + \Delta]$ with current density of J_0 . Then we can derive the induce current in conducting half space as

$$\begin{aligned}
 J(x, y) &= -j\omega\sigma A_3(x, y) \otimes J_s(x, y - h) \\
 &= -j\omega\sigma\mu J_0 \int_0^\infty \frac{2\sin(k\tau)}{\pi k} \frac{e^{\gamma\Delta} - e^{-\gamma\Delta}}{\gamma} \frac{e^{-kh}}{k + \gamma} \cos(kx) e^{\gamma y} dk
 \end{aligned} \tag{5.17}$$

Finally, the induction field in time domain can be obtained by an inverse Fourier transform to (5.17).

Figure 5.6 shows the induction field for various excitation frequencies. The solid lines denote the EFG solutions and the dash lines denote the analytic solutions. The numerical results lose some accuracy at low frequency region, and the cut-off error on boundaries will be significant as frequency becomes low, which is caused by skin depth effect. As expected, the EFG solutions agree with the analytical solutions quite well at higher frequency region.



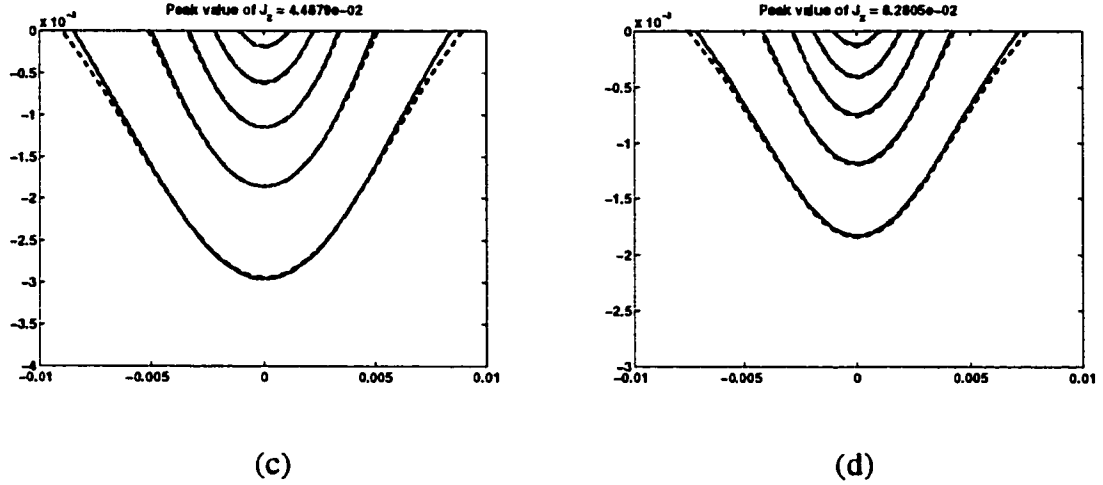


Figure 5.6 Induced current in the conducting plate with a sinusoidal excitation and parameters $\tau = 0.72 \text{ mm}$, $\Delta = 0.5 \text{ mm}$ and $h = 2 \text{ mm}$ at (a) $\omega = 400 \text{ Hz}$, (b) $\omega = 1 \text{ KHz}$, (c) $\omega = 4 \text{ KHz}$, (d) $\omega = 10 \text{ KHz}$. The contour lines are drawn at value of 0.1, 0.3, 0.5, 0.7, 0.9 times peak value.

As Δ becomes very small, the current source can be modeled as a sheet source with constant density of $K_0 = 2\Delta J_0$, and in turn, Equation (5.17) turns to be

$$J(x, y) = -j\omega\sigma\mu \frac{2\tau K_0}{\pi} \int_0^{\infty} \frac{\sin(k\tau)}{k\tau} \frac{e^{-kh}}{k+\gamma} \cos(kx) e^{jy} dk \quad (5.18)$$

In time domain, if the current source is a step function, that is,

$$i(t) = \begin{cases} I_0 & t \geq 0 \\ 0 & t < 0 \end{cases} \quad (5.19a)$$

The corresponding frequency response is

$$I(\omega) = \frac{I_0}{j\omega} \quad (5.19b)$$

From (5.18), the induced current in frequency domain can be expressed as

$$J(x, y) = -\sigma\mu \frac{I_0}{\pi} \int_0^{\infty} \frac{\sin(k\tau)}{k\tau} \frac{e^{-kh}}{k+\gamma} \cos(kx) e^{jy} dk \quad (5.20)$$

By inverse Fourier transform, we obtain the induced current in time domain as

$$j(x, y, t) = \frac{-I_0}{\pi} \int_0^{\infty} \frac{\sin(k\tau)}{k\tau} e^{-kh} \exp\left(\frac{-k^2 t}{\sigma\mu}\right) \cos(kx) \cdot \left[\sqrt{\frac{\sigma\mu}{\pi t}} \exp\left(\frac{-y^2 \sigma\mu}{4t}\right) - k \exp\left(-yk + \frac{k^2 t}{\sigma\mu}\right) \operatorname{erfc}\left(-\frac{y}{2} \sqrt{\frac{\sigma\mu}{t}} + k \sqrt{\frac{t}{\sigma\mu}}\right) \right] dk \quad (5.21)$$

where erfc is complementary error function defined as

$$\operatorname{erfc}(x) = 1 - \frac{2}{\sqrt{\pi}} \int_0^x e^{-t^2} dt \quad (5.22)$$

Comparing the EFG solution and analytical expression, we see they agree closely with each other as the width of current source approaches zero, which is shown in Figure 5.7. As time marches, the numerical error does not grow, so the method is very stable.

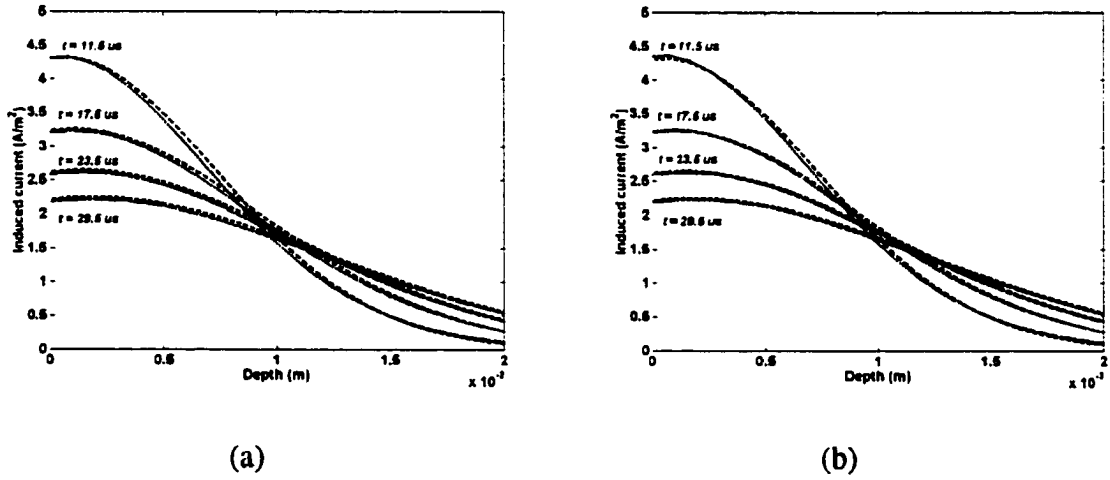


Figure 5.7 Induced current distribution along y axis at various time instances. (a) $\Delta = 0.5 \text{ mm}$ (b) $\Delta = 0.1 \text{ mm}$. Dashed lines denote the analytical solution, solid line denote the numerical solution.

5.4 Conducting plate under Current Foil

So far we have studied the analytical solutions of the conducting half space. Using a similar approach, we obtain analytic expression for the current induced in a conducting plate by a current foil.

Consider the problem shown in Figure 5.8. The current source is a semi-infinite sheet $h(m)$ above the conducting plate with current density of $J_s (A/m^2)$, the length of the current sheet is $l(m)$ and the thickness is $s(m)$. The thickness of the conducting plate is $d(m)$. Assume $J_s = \delta(x)\delta(y-h)$, then the vector potential can be written as

$$A_1(x, y) = \int_0^{\infty} C_1(k) \cos(kx) e^{-ky} dk \quad (5.23a)$$

$$A_2(x, y) = \int_0^{\infty} [C_2(k) e^{ky} + D_2(k) e^{-ky}] \cos(kx) dk \quad (5.23b)$$

$$A_3(x, y) = \int_0^{\infty} [C_3(k) e^{y'} + D_3(k) e^{-y'}] \cos(kx) dk \quad (5.23c)$$

$$A_4(x, y) = \int_0^{\infty} C_4(k) \cos(kx) e^{ky} dk \quad (5.23d)$$

A_i denotes the vector potential in the i th region as shown in Figure 5.8.

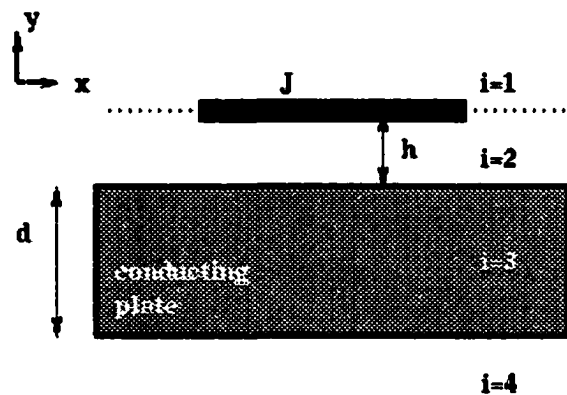


Figure 5.8 Conducting plate under current sheet.

The interface conditions are written as

$$C_1(k)e^{-kh} = C_2(k)e^{kh} + D_2(k)e^{-kh} \quad (5.24a)$$

$$C_1(k)e^{-kh} + C_2(k)e^{kh} - D_2(k)e^{-kh} = \frac{\mu}{\pi k} \quad (5.24b)$$

$$C_2(k) + D_2(k) = C_3(k) + D_3(k) \quad (5.24c)$$

$$C_2(k)k - D_2(k)k = C_3(k)\gamma - D_3(k)\gamma \quad (5.24d)$$

$$C_3(k)e^{-\gamma d} + D_3(k)e^{\gamma d} = C_4(k)e^{-kd} \quad (5.24e)$$

$$C_3(k)\gamma e^{-\gamma d} - D_3(k)\gamma e^{\gamma d} = C_4(k)ke^{-kd} \quad (5.24f)$$

Equations (5.24c-f) can be expressed in matrix form as

$$\begin{pmatrix} 1 & 1 \\ k & -k \end{pmatrix} \begin{pmatrix} C_2 \\ D_2 \end{pmatrix} = \begin{pmatrix} 1 & 1 \\ \gamma & -\gamma \end{pmatrix} \begin{pmatrix} C_3 \\ D_3 \end{pmatrix} \quad (5.25a)$$

$$\begin{pmatrix} e^{-\gamma d} & e^{\gamma d} \\ \gamma e^{-\gamma d} & -\gamma e^{\gamma d} \end{pmatrix} \begin{pmatrix} C_3 \\ D_3 \end{pmatrix} = \begin{pmatrix} C_4 e^{-kd} \\ C_4 k e^{-kd} \end{pmatrix} \quad (5.25b)$$

So

$$\begin{pmatrix} C_3 \\ D_3 \end{pmatrix} = C_4 \begin{pmatrix} \frac{k+\gamma}{2\gamma} e^{-(k-\gamma)d} \\ -\frac{k-\gamma}{2\gamma} e^{-(k+\gamma)d} \end{pmatrix} \quad (5.26a)$$

$$\begin{pmatrix} C_2 \\ D_2 \end{pmatrix} = C_4 \begin{pmatrix} \frac{(k+\gamma)^2}{4k\gamma} e^{-(k-\gamma)d} - \frac{(k-\gamma)^2}{4k\gamma} e^{-(k+\gamma)d} \\ \frac{k^2 - \gamma^2}{4k\gamma} e^{-(k-\gamma)d} - \frac{k^2 - \gamma^2}{4k\gamma} e^{-(k+\gamma)d} \end{pmatrix} \quad (5.26b)$$

By substituting (5.24a) into (5.24b), we obtain

$$C_2(k) = \frac{\mu}{2\pi k} e^{-kh} \quad (5.27a)$$

Thus

$$D_2(k) = \frac{(k^2 - \gamma^2)e^{-(k-\gamma)d} - (k^2 - \gamma^2)e^{-(k+\gamma)d}}{(k+\gamma)^2 e^{-(k-\gamma)d} - (k-\gamma)^2 e^{-(k+\gamma)d}} \frac{\mu}{2\pi k} e^{-kh} \quad (5.27b)$$

$$C_1(k) = \frac{\mu}{2\pi k} e^{kh} + \frac{(k^2 - \gamma^2)e^{-(k-\gamma)d} - (k^2 - \gamma^2)e^{-(k+\gamma)d}}{(k+\gamma)^2 e^{-(k-\gamma)d} - (k-\gamma)^2 e^{-(k+\gamma)d}} \frac{\mu}{2\pi k} e^{-kh} \quad (5.27c)$$

$$C_4(k) = \frac{4k\gamma}{(k+\gamma)^2 e^{-(k-\gamma)d} - (k-\gamma)^2 e^{-(k+\gamma)d}} \frac{\mu}{2\pi k} e^{-kh} \quad (5.27d)$$

$$C_3(k) = \frac{4k\gamma}{(k+\gamma)^2 e^{-(k-\gamma)d} - (k-\gamma)^2 e^{-(k+\gamma)d}} \frac{k+\gamma}{2\gamma} \frac{\mu}{2\pi k} e^{-kh} e^{-(k-\gamma)d} \quad (5.27e)$$

$$D_3(k) = -\frac{4k\gamma}{(k+\gamma)^2 e^{-(k-\gamma)d} - (k-\gamma)^2 e^{-(k+\gamma)d}} \frac{k-\gamma}{2\gamma} \frac{\mu}{2\pi k} e^{-kh} e^{-(k+\gamma)d} \quad (5.27f)$$

Assume the source is uniformly distributed in a region $[-\tau \tau] \times [h - \Delta \ h + \Delta]$ with current density of J_0 . We can express the magnetic vector potential in the first region as

$$\begin{aligned} \tilde{A}_1(x, y) &= A_1(x, y) \otimes J_5(x, y - h) \\ &= J_0 \int_0^\infty C_1(k) \frac{-2 \sin(k\tau) e^{k\Delta} - e^{-k\Delta}}{k} \cos(kx) e^{-ky} dk \end{aligned} \quad (5.28a)$$

and in other regions as

$$\tilde{A}_2(x, y) = J_0 \int_0^\infty (C_2(k) e^{ky} + D_2(k) e^{-ky}) \frac{-2 \sin(k\tau) e^{k\Delta} - e^{-k\Delta}}{k} \cos(kx) dk \quad (5.28b)$$

$$\tilde{A}_3(x, y) = J_0 \int_0^\infty (C_3(k) e^{\gamma y} + D_3(k) e^{-\gamma y}) \frac{-2 \sin(k\tau) e^{k\Delta} - e^{-\gamma\Delta}}{\gamma} \cos(kx) dk \quad (5.28c)$$

$$\tilde{A}(x, y) = J_0 \int_0^\infty C_4(k) \frac{-2 \sin(k\tau) e^{k\Delta} - e^{-k\Delta}}{k} \cos(kx) e^{ky} dk \quad (5.28d)$$

In the MOI modeling that was discussed in Chapter 3, the parameters chosen, are $h = 0.37 \text{ mm}$, $\tau = 30 \text{ mm}$, $\Delta = 0.02 \text{ mm}$, $d = 1.5 \text{ mm}$, $\sigma = 1.8867 \times 10^7 \text{ S}$ and

$J_s = 10^8 \text{ A/m}^2$. Figure 5.9-10 show the comparison between exact solutions and numerical solutions, Dirichlet boundary condition were applied on upper Y boundary and lower Y boundary, both of them were set to be the values of exact solution. The numerical potential matches the exact solution very well in the solution domain, which indicates that the proposed method is accurate and reliable. For realistic complicated problems, the exact solutions are usually unknown, homogeneous Dirichlet boundary conditions can be applied, but requires a relative larger solution domain.

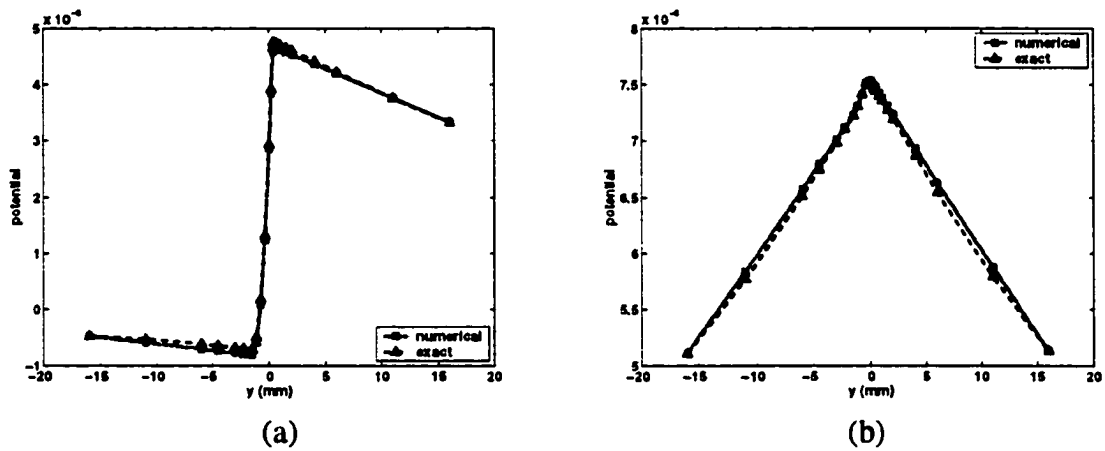


Figure 5.9 Magnetic vector potential with frequency of 3 KHz (a) real part (b) imaginary part

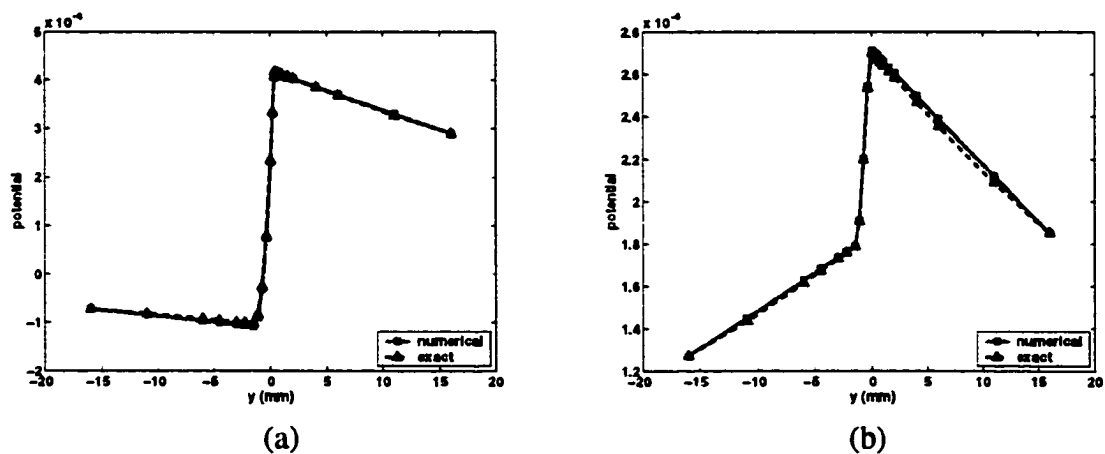


Figure 5.10 Magnetic vector potential with frequency of 10 KHz (a) real part (b) imaginary part

CHAPTER 6. 3D ELEMENT FREE GALERKIN METHOD

6.1 Introduction

Modeling a realistic problem in electromagnetics inevitably involves into solving a three-dimensional fields equations. This chapter presents the extension of the work to modeling a 3D problem. In the formulation of 2D or 3D EFG, one can use a circular weight function or tensor product weight. Contrast to circular weight, tensor product weight results in a relatively simple quadrature procedure. Similar to the expression in (4.13), a tensor product weight at any given point can be expressed as

$$w(\mathbf{x} - \mathbf{x}_j) = w_x \cdot w_y \cdot w_z = w(r_x) \cdot w(r_y) \cdot w(r_z) \quad (6.1)$$

6.2 Numerical Implementation

The static field problem and quasi-static field problem are two important issues in NDE. For electric static problem the field equations reduce directly to the Poisson equation. While for quasi-static problem the field equations can be simplified to the diffusive equation and involves both magnetic vector and electric scalar potential. The numerical procedure for the solution of these problems using 3D EFG formulation is very similar to that using FEM scheme.

6.2.1 Static Fields

Consider the Poisson equation

$$\begin{aligned} \nabla^2 u(x, y, z) &= 12\pi^2 \sin(2\pi x) \sin(2\pi y) \sin(2\pi z) \\ \text{for } (x, y, z) &\in [-0.5, 0.5] \times [-0.5, 0.5] \times [-0.5, 0.5] \end{aligned} \quad (6.2a)$$

with homogeneous boundary condition

$$u(x, y, z) = 0 \quad (6.2b)$$

The analytical solution for this problem is

$$u^{exact}(x, y, z) = \sin(2\pi x) \sin(2\pi y) \sin(2\pi z) \quad (6.3)$$

The 3D numerical model consists of $n \times n \times n$ integration cells for $n = 7, 11, 17, 25$ with 4×4 Gaussian quadrature in each cell. Linear basis is applied to construct the shape function. The error estimations in L^2 and H^1 norm are shown in Figure 6.1. Those errors can be written as

$$L^2 err(h) = \left\{ \frac{\int_{\Omega} (u^{num} - u^{exact})^2 d\Omega}{\int_{\Omega} (u^{exact})^2 d\Omega} \right\}^{\frac{1}{2}} \quad (6.4a)$$

$$H^1 err(h) = \left\{ \frac{\int_{\Omega} (u^{num} - u^{exact})^2 + \sum_{\alpha=x,r,\text{or } z} (u_{\alpha}^{num} - u_{\alpha}^{exact})^2 d\Omega}{\int_{\Omega} u^{exact^2} + \sum_{\alpha=x,r,\text{or } z} (u_{\alpha}^{exact})^2 d\Omega} \right\}^{\frac{1}{2}} \quad (6.4b)$$

Again, the convergence rate of EFG depends on the scaling factor. The convergence rate varies from 2.16 to 3.10 in L^2 norm for EFG, in contrast to 1.89 for linear FEM. The convergence rate in H^1 norm varies from 1.10 to 2.16 for EFG, also higher than that of linear FEM. The results for computation cost are summarized in Fig. 18. For a fixed size of mesh, FEM is much less expensive than EFG; however, for a given precision EFG uses less computation time than FEM. The EFG has a high set up cost to assemble the matrix, which is

a bottleneck for meshless methods. A variety of matrix assembly techniques have been applied as reported in [40] by Han, Oliveira and Stewart.

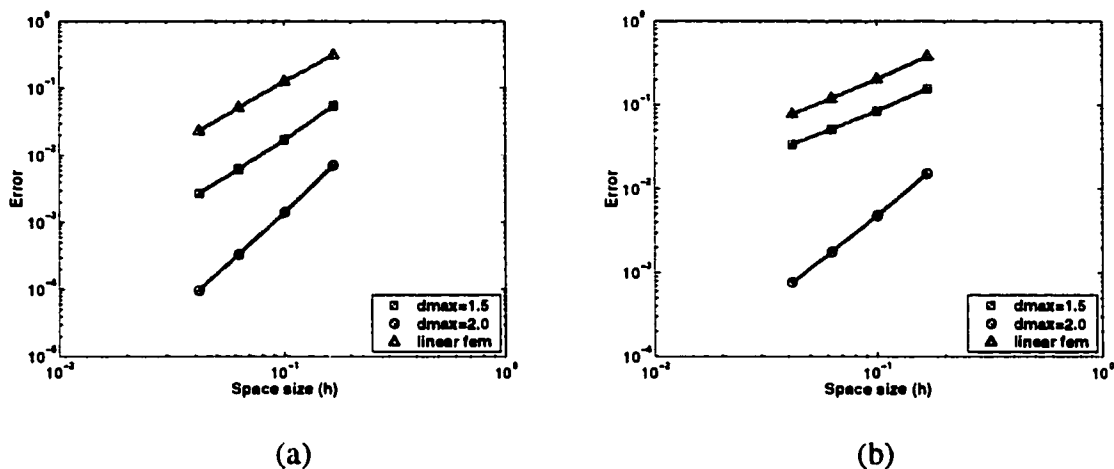


Figure 6.1 (a) Error estimation in L^2 norm for the linear EFG. (b) Error estimation in H^1 norm for the linear EFG.

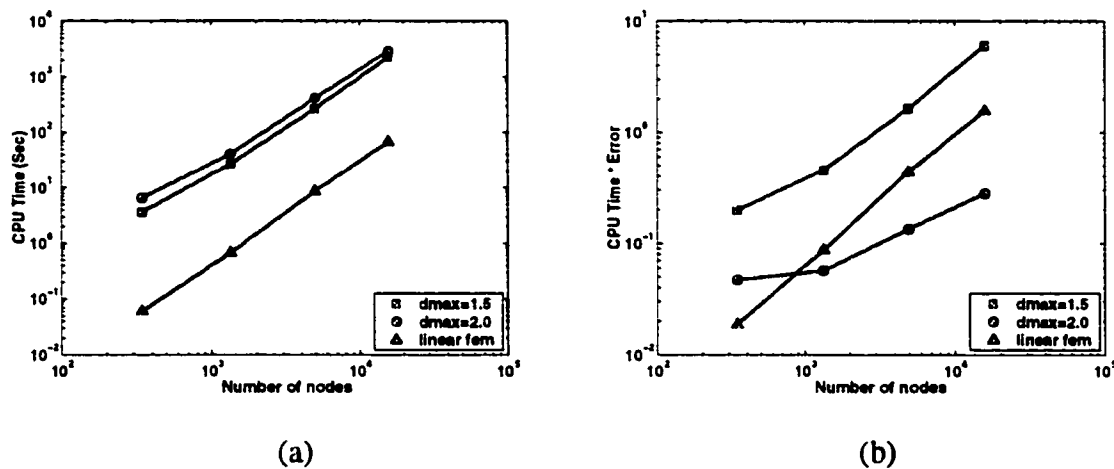


Figure 6.2 Computation time for 3D Poisson Problems. (a) CPU time versus number of nodes. (b) The product of CPU time and numerical error versus number of nodes.

6.2.2 *Quasi-static Fields*

In this section, we validate the 3D EFG method by comparing results against canonical problem and finally, demonstrate its application for analyzing a practical problem.

The governing equations for eddy currents are given by Maxwell equations based on $A-V$ formulation similar to those in the previous chapters. EFG method is applied for the solution of the differential equations. Some key differences between the two methods are (i) 3D EFG shape function is of higher order than the linear FEM shape function. (ii) The stiffness matrix is assembled point by point (quadrature point), other than element by element. (iii) Boundary conditions are imposed using Lagrange multiplies technique in EFG, thus it results in a larger algebraic system than the normal FEM. The model is first validated using a simple geometry.

(a) Conducting plate under current foil: An infinite sinusoidal AC current foil of 1 mm thick and 12 mm wide is placed above a conducting plate of 3 mm thick and infinite wide (both are infinite along current direction) as shown in Figure 6.3. Current density is 1 A/m^2 . The solution region is set as $[-12\ 12] \times [-12\ 12] \times [-5\ 5]\text{ mm}^3$, and $7 \times 7 \times 21$ uniform distributed nodes were used for discretization. Boundary conditions are summarized in Table 6.1. Figure 6.5-6 shows the X component of magnetic vector potential at different locations. It is observed that the real part of the numerical results approximates the analytic solution better than the imaginary part, this is because the real part is a dominant term in the complex form.

Table 6.1 Boundary conditions.

Upper boundary ($z = 5 \text{ mm}$)	$A_y = A_z = 0, V = 0, A_x =$ the value of analytic solution
Lower boundary ($z = -5 \text{ mm}$)	$A_y = A_z = 0, V = 0, A_x =$ the value of analytic solution
Left boundary ($x = -12 \text{ mm}$)	$A_y = A_z = 0, V = 0, A_x$ is free
Right boundary ($x = 12 \text{ mm}$)	$A_y = A_z = 0, V = 0, A_x$ is free
Front boundary ($y = -12 \text{ mm}$)	$A_y = A_z = 0, V = 0, A_x$ is free
Rear boundary ($y = 12 \text{ mm}$)	$A_y = A_z = 0, V = 0, A_x$ is free

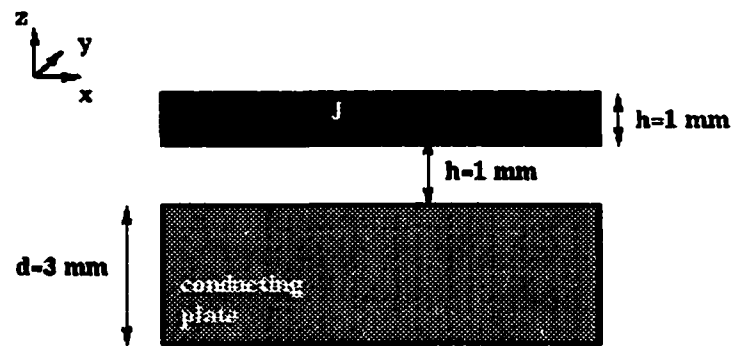
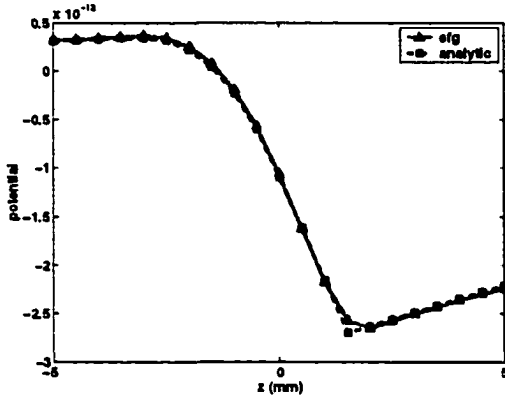
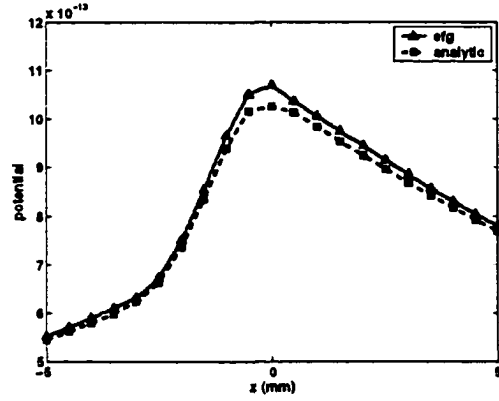


Figure 6.3 Geometry of conducting plate under current foil.

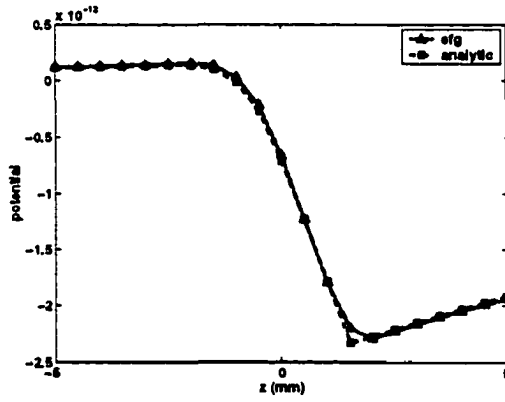


(a)

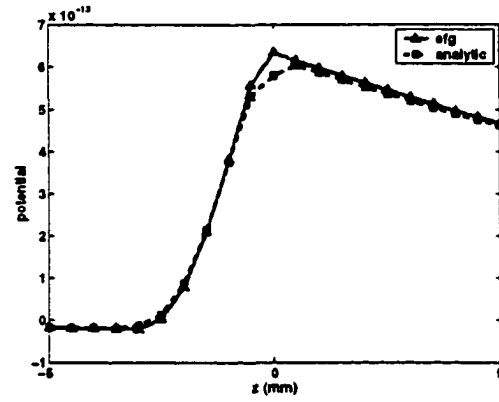


(b)

Figure 6.4 Magnetic vector potential at frequency of 3 *KHz* . (a) real part, (b) imaginary part.



(a)

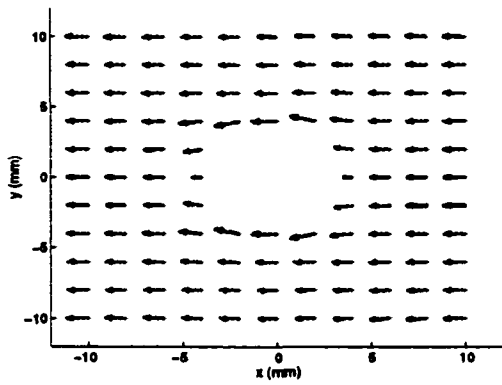


(b)

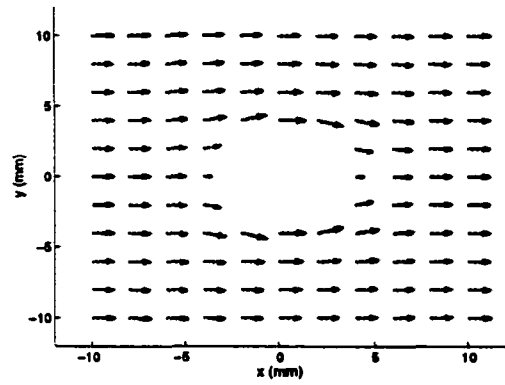
Figure 6.5 Magnetic vector potential at frequency of 10 *KHz* . (a) real part, (b) imaginary part.

(b) Defects in Conducting plate: Here we introduce a defect in the conducting plate, and set the excitation frequency at 1kHz . The solution region is chosen as $[-10\ 10] \times [-10\ 10] \times [-5\ 2]\text{mm}^3$. It has 11 nodes in X and Y directions, respectively, and 8 nodes in Z direction. This produces a discretization with a total of 700 integration cells and 968 nodes (3872 unknowns).

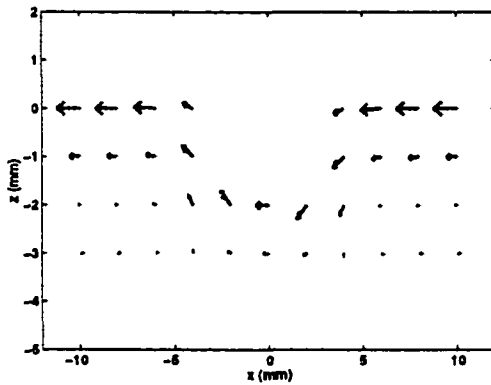
Figure 6.6 shows the induced eddy currents in the conducting plate with a square EDM notch of 5mm width and 1.5mm depth. Both real part and imaginary part of the eddy currents in complex form are plotted. It is observed that the induced currents flow around the defect without passing across, which agrees with underlying physics and experiments. Figure 6.7 shows the induced currents nearby a tight crack of 5mm length and 3mm depth (cutting through the sample plate). EFG does not require a fine mesh around the crack for accurately predicting the characteristics of the induction phenomenon.



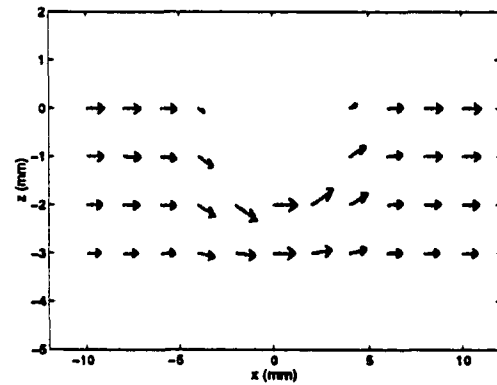
(a)



(b)



(c)



(d)

Figure 6.6 Induced currents in the conducting plate. (a) Top view of the real part of currents (plane $z = 0$) (b) Top view of the imaginary part of currents (plane $z = 0$) (c) Side view of the real part of currents (plane $y = 0$) (d) Side view of the imaginary part of currents (plane $y = 0$)

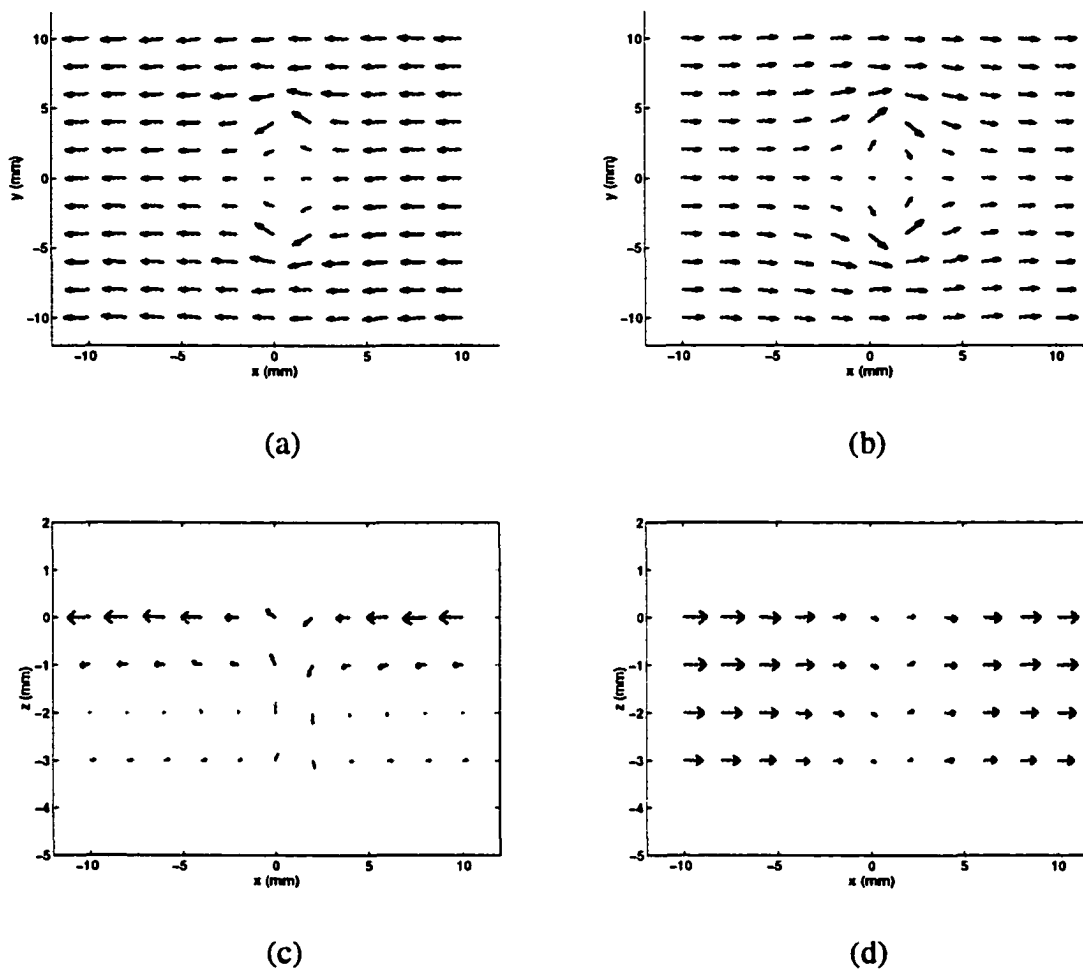


Figure 6.7 Induced currents in the conducting plate. (a) Top view of the real part of currents (plane $z = 0$) (b) Top view of the imaginary part of currents (plane $z = 0$) (c) Side view of the real part of currents (plane $y = 0$) (d) Side view of the imaginary part of currents (plane $y = 0$)

CHAPTER 7. SUMMARY AND FUTURE WORK

The Magneto-Optic/Eddy Current imaging (MOI) method is a recently developed NDT technique used in aging aircraft inspection. Compared with traditional eddy current methods, it is attractive to industry due to some of its distinct characteristics. The availability of real-time images of defect and large area coverage makes the detection and interpretation of inspected data fast and easy. At higher frequencies, MOI techniques can image and detect small, tight fatigue defect near rivet on the outer surface of aluminum aircraft skin; subsurface cracks and corrosion in the multiple layer structure can be detected at lower frequencies. The finite element method is a useful tool for optimizing the design of MOI sensor and developing processing algorithms for the analysis of MO image data.

7.1 Summary of Work

- Finite element model based on $A-V$ formulation has been developed to simulate MO inspection. The model has been validated and successfully applied to a number of inspection geometries such as hole, corrosion, and cracks both in the first and second layer. It has been also applied to complex geometries such as cracks under fastener (CUF).
- Modeling of complex geometry such as CUF where air gap and cracks are present near the rivet head results in a large linear system. A fast iterative solver called Transpose-Free Quasi Minimal Residual method has been applied with a proper

preconditioning technique such as incomplete LU method. The method shows a distinct advantage in terms of computational time and data storage.

- In order to model the complex CUF geometry, Element-Free Galerkin (EFG) method has been studied. Two-dimensional models for the Poisson equation and eddy current geometry have been developed and compared with conventional FEM.
- Multifrequency and pulsed eddy currents methods are two common techniques in NDT applications. Corresponding numerical models based on EFG method are constructed and verified.
- 3D EFG method is developed to solve static and eddy current problems. Several initial results demonstrate a promising role for the EFG method in modeling NDT problems.

7.2 Future Work

Theoretically, meshless methods can achieve any desired accuracy depending on the order of shape functions. However, like conventional FEM method, the accuracy of EFG methods rely on the correctness of formulation, the regularity of discretization (and background mesh), the precision of interface and boundary conditions. The success of EFG method depends on how well it handles to an inhomogeneous, multiply connected complex geometry. In order to model a complicated NDT problem, an efficient way for pre setup is required before solving the matrix system. Several techniques have been reported, and this issue should as rigorously in the future.

Finally, in eddy current inverse problems, reconstruction of defect profile can be achieved by combining the corresponding forward model with optimization theory. Remeshing is usually required in every iterative step in a traditional FE forward model. A forward model based on meshless method can handle changes in defect profile more efficiently since only the position of nodes around the defect area needs to change and no remeshing is involved.

REFERENCES

- [1] D. E. Bray and R. K. Stanley, *Nondestructive Evaluation*, McGraw Hill, 1989
- [2] S. Udpa, L. Udpa, "Eddy Current Nondestructive Evaluation," *Encyclopedia of Electrical and Electronics Engineering*, John G. Webster, Editor, John Wiley, 1999
- [3] S. Sharma, "Application of Finite Element Models to Eddy Current Probe Design for Aircraft Inspection," Ph.D. Dissertation, Iowa State University, 1997
- [4] C. Chen, "Finite Element Modeling of MOI for NDE Applications," Master Thesis, Iowa State University. 2000
- [5] J. D. Jackson, *Classical Electrodynamics*, John Wiley & Sons Inc, New York, 1998
- [6] C. A. Balanis, *Advanced Engineering Electromagnetics*, John Wiley & Sons Inc, New York, 1989
- [7] G. L. Fitzpatrick, "Imaging Near Surface Flaws in Ferromagnetic Materials Using Magneto-Optic Detectors," *Review of Progress in Quantitative Nondestructive Evaluation*, edited by D. O. Thompson and D. E. Chimenti, Plenum Publishing Corporation, Norwell, Massachusetts, 1985
- [8] G. L. Fitzpatrick, D. K. Thome, R. L. Skaugset etc, "Magneto-Optic/Eddy Current Imaging of Aging Aircraft: A new NDI Technique," *Material Evaluation*, pp. 1402-1407, Dec. 1993.
- [9] G. L. Fitzpatrick with D. K. Thome, "Aircraft Inspection with the Magneto-Optic/Eddy Current Imager – A New Technology," presented at the Air Transport Association, NDT Forum, Long Beach, California, Sep., 1991

- [10] Simms, Sandra, "MOI: Magneto-Optic/Eddy Current Imaging," *Material Evaluation*, pp. 529-534, May 1993
- [11] G. L. Fitzpatrick, D. K. Thome and R. Skaugset, "Advanced Magneto-Optic/Eddy Current Techniques for Detection of Hidden Corrosion Under Aircraft Skins," Reported submitted by Physical Research Inc. to Naval Surface Warfare Center (1995)
- [12] D. Yang, C. L. Wang and Y. Pu, *Magneto-optics, The Electrical Engineering Handbook*, R. C. Dorf, editor-in-chief, CRC Press
- [13] A. Elshafiey and L. Udpa, "Finite Element Modeling of Magneto-Optic Inspection of Hidden Flaws in Aging Aircraft," *The Fifth Internal Workshop on Electromagnetic Nondestructive Evaluation*, Aug. 1-3, 1999
- [14] G. B. Scott and D. E. Lacklison, "Magneto-Optic Properties and Applications of Bimuth Substituted Iron Garnets," *IEEE Transactions on Magnetics*, MAG-12, July 1976
- [15] A. P. Malozemoff, J. C. Slonczewski, *Magnetic Domain Walls in Bubble Materials*, Academic Press Inc, New York, 1979
- [16] A. H. Eschenfelder, *Magnetic Bubble Technology*, Springer series in solid-state sciences, 1981
- [17] J. Jin, *The Finite Element Method in Electromagnetics*, John Wiley & Sons Inc, New York, 1993
- [18] K. J. Binns, R. J. Lawrenson and C. W. Trowbridge, *The Analytical and Numerical Solution of Electric and Magnetic Fields*, John Wiley & Sons Inc, 1992

- [19] A. F. Peterson, S. L. Ray and R. Mittra, *Computational Methods for Electromagnetics*, IEEE Press, 1998
- [20] J. K. Sykulski, *Computational Magnetics*, Chapman & Hall, 1995
- [21] I. Nathan, *Three Dimensional Finite Element Modeling of Electromagnetic Nondestructive Testing Phenomena*, Ph.D. Dissertation, 1983
- [22] O. Biro and K. Preis, "On the Use of the Magnetic Vector Potential in the Finite Element Analysis of Three-Dimensional Eddy Currents," *IEEE Transactions on Magnetics*, vol. 25, no. 4, pp. 3145-3159, July (1989)
- [23] K. Preis, I. Bardi and O. Biro, "Different Finite Element Formulations of 3D Magnetostatic Fields," *IEEE Transactions on Magnetics*, vol. 28, no. 2, pp. 1056-1059, March, 1992
- [24] O. Biro and K. Preis, "Finite Element Analysis of 3-D Eddy Current," *IEEE Transactions on Magnetics*, vol. 26, no. 2, pp 418-423, March, 1990
- [25] O. Biro, K. Preis and W. Renhart, "Finite Element Analysis of 3D Multiply Connected Eddy Current Problems," *IEEE Transactions on Magnetics*, vol. 25, no. 5, pp. 4009-4011, Sept. 1989
- [26] L. N. Trefethen and D. Bau, *Numerical Linear Algebra*, SIAM, 1997
- [27] C.T. Kelley, *Iterative Methods for Linear and Nonlinear Equations*, SIAM, 1995
- [28] R. W. Freund, "Transpose-Free Quasi-Minimal Residual Methods for Non-Hermitian Linear Systems," *Advances in Computer Methods for Partial Differential Equations*, pp. 258-264, IMACS, 1992.
- [29] T. Belytschko, Y. Y. Lu, and L. Gu, "Element-Free Galerkin methods," *International Journal for Numerical Methods in Engineering*, vol. 37, pp. 229-256, 1994

- [30] T. Belytschko, Y. Krongauz, D. Organ, M. Fleming, and P. Krysl, "Meshless methods: An overview and recent developments," *Computer Methods in Applied Mechanics and Engineering* 139, 1-4, pp.3-47, 1996
- [31] J. Dolbow and T. Belytschko, "An Introduction to Programming the Meshless Element Free Galerkin Method," *Archives in Computational Mechanics*, Vol. 5, No. 3, pp. 207-241, 1998
- [32] V. Cingoski, N. Miyamoto, and H. Yamashita, "Element-free Galerkin method for electromagnetic field computations," *IEEE Transactions on Magnetics*, vol. 34, no. 5, pp. 3236–3239, 1998
- [33] S. A. Viana and R. C. Mesquita, "Moving least square reproducing Kernel method for electromagnetic field computation," *IEEE Transactions on Magnetics*, vol. 35, no. 3, pp. 1372–1375, 1999
- [34] S. L. Ho, S. Yang, J. M. Machado and H. C. Wong, "Applications of a Meshless Method in Electromagnetics," *IEEE Transactions on Magnetics*, vol. 37, no. 5, pp. 3198–3202, 2001
- [35] J. Bowler and M. Johnson, "Pulsed Eddy-Current Response to a Conducting Half-Space," *IEEE Transactions on Magnetics*, vol. 33, no. 3, pp. 2258-2264, May, 1997
- [36] C. C. Cheng, C. V. Dodd and W. E. Deeds, "Analytical solutions to eddy-current probe-coil problems over layered metals," *Internal Journal for Nondestructive testing*, vol. 109, pp. 90-109, 1969

- [37] R. Ludwig and X. Dai, "Numerical and Analytic Modeling of Pulsed Eddy Currents in a Conducting Half-Space," *IEEE Transactions on Magnetics*, vol. 26, no. 1, pp. 299-307, January, 1990
- [38] J. C. Moulder, M. W. Kubovich, E. Uzal and J. H. Rose, "Pulsed eddy-current measurement of corrosion-induced metal loss: Theory and experiment," *Review of Progress in DNDE*, vol. 14, edited by D. O. Thompson and D. E. Chimenti, Plenum Press, New York, pp. 2065-2072, 1995
- [39] R. Satveli, J. C. Moulder, J. H. Rose, "Impedance of a coil near an imperfectly layered metal structure: The layer approximation," *Journal for Applied Physics*, vol. 79, pp.2811, 1995
- [40] X. Han, S. Oliveira and D. Stewart, "New Matrix Assembly Techniques for Meshless Methods," *Computational Mathematics TR 128*, University of Iowa, 1999